ISAE-SUPAERO
&
POLITECNICO DI TORINO

Master's Thesis

A.a. 2024-2025

Failure and damage modelling of alumina in ceramic-composite ballistic protection

Supervisors:
Frédéric Lachaud
Marco Gherlone

Student:
Pietro Lapini
317907

Contents

Introduction

Context and objective of the study

One of the main problems encountered in the field of defense today is the development of high-performance and lightweight ballistic protections for the protection of personnel and armored vehicles.
The main objective of research is to increase the stopping power of protection systems without excessively sacrificing the lightness of the equipment and, consequently, the agility of the fighter. The need for such a compromise has led to the development of advanced materials capable of withstanding high-velocity projectile impacts. Among these, technical ceramics represent one of the most effective solutions for the design of lightweight and high-performance armor thanks to their high hardness, low density, and good wear resistance.
The main personal protection system is undoubtedly the bulletproof vest, whose purpose is to protect the vital organs of the fighter's chest cavity, opposing the penetration of the projectile and absorbing its energy. The optimization of the materials composing bulletproof vests has led to the design of multilayered structures, combining materials with different mechanical properties and behaviors rather than using single layers of homogeneous material.
The concept is to pair a front layer, capable of blunting the projectile, with a backing layer whose role is to dissipate the kinetic energy of the impact (Figure 1). The two protection layers thus have completely different roles and mechanical characteristics: for the front layer, it is necessary to use a highly hard and rigid material, whereas for the backing, a soft and elastic material is employed, capable of absorbing the impact energy.

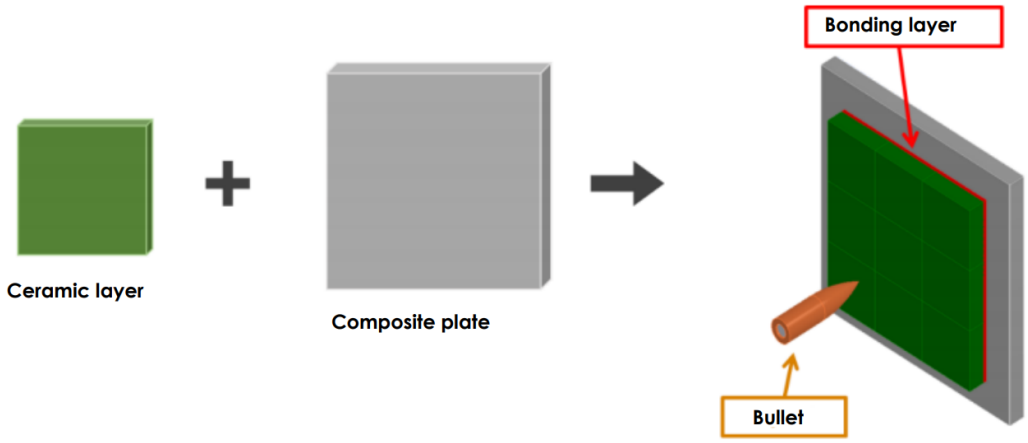

Figure 1: Scheme of a Dual Harness Armor [1].

The materials and their respective thicknesses must be chosen considering both the desired stopping power and the associated weight and dimensions, while also trying to minimize as much as possible the deflection of the backing towards the vital organs of personnel.
A protection system of this type is called "Dual Hardness Armor" (DHA).
The optimization of such protection must necessarily involve an understanding of the different degradation mechanisms of each layer and how the various materials interact in dissipating the impact energy.
This thesis fits within the study of alumina ceramic (Al_2O_3) as the primary material for the first layer of a Dual Hardness Armor: the objective is to compare and calibrate different sets of parameters available in the literature for the finite element simulation of the degradation and damage accumulation process using the JH2 numerical model ("Johnson Holmquist 2" [12]).
In order to evaluate the performance of the Johnson Holmquist 2 model in simulating ceramic under impact, experimental tests have been conducted under both static conditions (three-point bending) and dynamic conditions at high and low velocities (Hopkinson Bar, Drop Test), which have enabled a comparison of the performance of various parameter sets selected from the literature.

Thesis organization

The present work is structured into six main chapters:

- Chapter 1: description of the state of the art and introduction of the fundamental concepts for the design of an effective and lightweight ballistic protection. Based on the literature, the essential characteristics of the different materials that can compose bi-layer protections are analyzed, starting from the damage mechanisms that come into play during impact. Particular attention is dedicated to the behavior of ceramics, the subject of the present study;
- Chapter 2: description of the functioning and the fundamental equations of the Johnson Holmquist 2 numerical model and introduction to some parameter sets from the literature. Finite element simulation tests are presented on a single mesh element to understand and illustrate how the variation of certain parameters plays a fundamental role in the model behavior. A comparison between the proposed parameter sets is then discussed;
- Chapter 3: description and results of the three-point bending experimental test conducted in ISAE Supaero laboratories. The test provided stiffness properties of the material, which allowed to update the parameters set from literature. The fractured specimens were observed under an optical microscope for illustrative purposes to identify the static fracture modes. The test was then replicated numerically with the updated parameter sets and their performance was then compared with the experimental results, identifying the most efficient one for the static case;
- Chapter 4: two dynamic test campaigns carried out using the Hopkinson Bar machine are presented, respectively at low and high velocity. The test aims to be a pre-test campaign to identify critical issues and problems in view of a more extensive experimental cycle, but it also provided useful data to evaluate the performance of the numerical model under dynamic loading conditions. A comparison was then made between the experimental behavior of the material and that predicted by the numerical models, also evaluating the fracture mechanisms, which were experimentally observed thanks to the use of high-speed cameras;
- Chapter 5: this chapter illustrates the experimental and numerical results of a series of drop tests conducted at low velocity on a ceramic plate. The test campaign qualitatively introduces the study of the influence of an elastomer interlayer between the front plate and the backing, acting as an hypothetical adhesive layer between the two layers. The experimental results were used to validate the fracture mechanisms of the numerical model in a real impact case, with all the limitations deriving from the low velocity of the test;
- Chapter 6: conclusions and future developments.

1 Ballistic protection systems

1.1 Ballistic protection standards

Ballistic protections must be able to prevent injuries caused by ballistic stresses by cushioning the impact of the projectile and dissipating its kinetic energy. The interaction between the projectile and organic tissues and the understanding of injury mechanisms is the subject of wound ballistics.

Figure 2: Bulletproof vest "interceptor multi-threat body armor", standard in the american army [1].

Among the various characteristics of the impact phenomenon, two are the most significant for estimating damage to a human target: the thoracic compression rate and the compression velocity. These are consequently the quantities that must be reduced for effective protection.
Depending on the armors ability to reduce these quantities and withstand ballistic threats, the National Institute of Justice (NIJ) of the United States has established a standard for the protection provided by bulletproof vests, categorizing protection levels into six classes:

- Level I: represents the lowest level of protection, now obsolete. It was designed to stop small-caliber projectiles such as the .22 Long Rifle Round Nose (LRRN) and the .380 ACP Full Metal Jacket Round Nose (FMJ RN). These projectiles travel at a speed of approximately 300-350 m/s, with a kinetic energy of less than 350 J;
- Level II-A: offers improved protection compared to the previous level, being able to stop more powerful ammunition, such as the 9×19 mm Parabellum FMJ RN and the .40 S&W FMJ. These projectiles reach speeds between 300 and 380 m/s and a kinetic energy up to 600 J;
- Level II: designed to stop 9 mm FMJ RN and .357 Magnum JSP projectiles, with speeds exceeding 400 m/s and kinetic energies ranging from 600 to 1000 J. This level represents a good compromise between protection and armor weight;
- Level III-A: advanced protection against more powerful handgun ammunition, such as the .357 SIG Flat Nose and the .44 Magnum SJHP. The maximum speed of these projectiles reaches 450 m/s, with a kinetic energy between 900 J and 1700 J. These protections are typically composed of a single "soft armor layer" made of high-strength fibers;
- Level III: is the first level designed to protect against rifle projectiles. It is capable of stopping 7.62×51 mm NATO (M80, 148 grains) rounds, which travel at approximately 850 m/s with a maximum kinetic energy of 3600 J. To achieve this level of protection, ballistic plates of level IIIA must be paired with rigid plates ("hard armor"), often made of ceramic material;

- Level IV: represents the highest level of protection offered by the NIJ standard. This level is capable of stopping high-velocity armor-piercing ammunition, such as the .30-06 Springfield M2 Armor Piercing (AP, 166 grains). The impact velocity of these projectiles is about 900 m/s, with a kinetic energy exceeding 4000 J. This type of protection is manufactured similarly to level III but with the addition of thicker and more resistant front plates.

This standard specifies for the different types of ammunition a maximum velocity for which protection is guaranteed and the number of impacts that each protection level can withstand. The ballistic tests for the certification of protection standards are carried out by simulating the human body with plastiline or, more often, ballistic gelatin, and are intended to verify that the velocity and extent of the deflection of the rear face are limited within a certain safety level.

1.2 Ballistic protections materials

The state of the art distinguishes the materials that compose a bulletproof vest into two macro categories: disruptive materials and absorptive materials.
Disruptive components are typically manufactured from high-strength materials such as high strength steels or ceramics. Their main purpose is to blunt and rapidly erode the tip of the impacting projectile so that it loses its penetrative capability. For this reason, hardness is a fundamental property in the selection of this type of materials.
Some very hard materials, such as ceramics, are also brittle and therefore tend to fragment and disperse radially. This phenomenon contributes to dissipating kinetic energy while increasing the contact area with the backing, thanks to the conical fracture zone that typically forms just beneath the impact point.
The absorptive materials, on the other hand, are materials capable of absorbing and dissipating the kinetic energy of the projectile through plastic or viscoplastic deformation, resulting in conversion into thermal energy. Some examples include steel, aluminum, or high-strength fiber composites.
In the history of the development of bulletproof vests, particular attention is given to the use of composite materials. The use of these materials in bulletproof vests is the result of a technological evolution that took place over the course of the 20th and 21st centuries, when the materials used for ballistic protection transitioned from simple layers of fabric and metal to sophisticated combinations of aramid fibers, ultra-high molecular weight polyethylene (UHMWPE), and advanced ceramics. One of the key events in the development of ballistic protections was undoubtedly the invention of the aramid fiber Kevlar by DuPont in 1965, which quickly established itself as the reference standard thanks to its properties of lightness, flexibility and high resistance.
Today, modern bulletproof vests are mainly composed of two primary classes of materials: para-aramid fibers such as Kevlar, Twaron, Goldflex and high-strength polyethylene fibers such as Spectra, Dyneema and Zylon.
All these fibers exhibit excellent mechanical properties, such as high toughness and stiffness, maintaining a very low density. Their use has significantly reduced the overall weight of ballistic protections, greatly increasing their stopping power.
To provide an idea of the mechanical properties of these materials, Figure 3 presents a comparison of most of the fibers used in ballistics in terms of tensile strength and Young modulus.

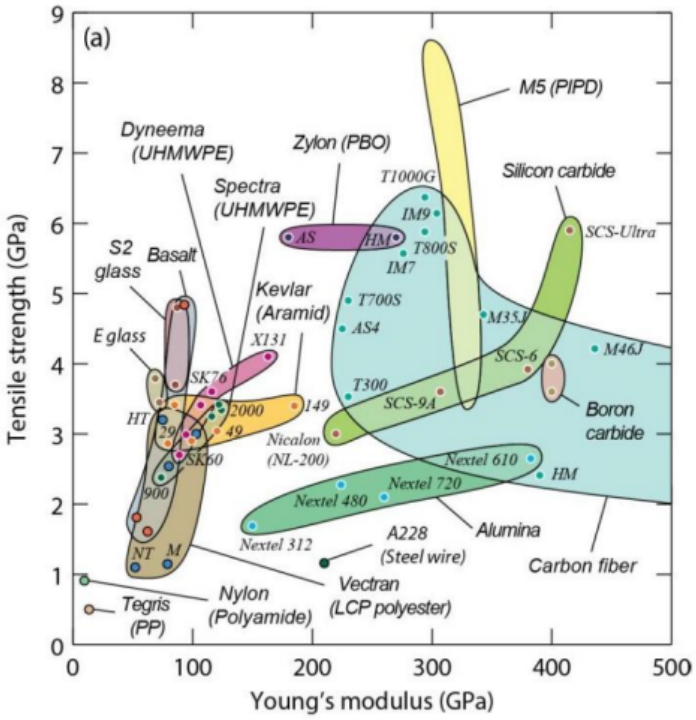

Figure 3: Tensile strength-Young modulus plot for main absortive materials [16].

Regarding disruptive materials, the state of the art identifies ceramics as the ideal candidate for the first layer of a DHA ballistic protection due to their characteristics of high hardness, strength and low density.
The most commonly used ceramics today are boron carbide (B_4C), silicon carbide (SiC), titanium diboride (TiB_2), aluminum nitride (AlN), and aluminum oxide (Al_2O_3), also known as "alumina," which is the focus of the present study.
Many studies have shown that numerous ceramic parameters influence the performance of a DHA armor. The main ones are certainly:

- Hardness;
- Tensile strength;
- Young modulus;
- Compressive strength;
- Density.

Properties	**Al_2O_3**	**B_4C**	**SiC**	**TiB_2**	**AlN**
Hardness (GPa)	15-20	30-38	22-28	25-30	10-12
Tensile strength (MPa)	300-500	200-400	400-600	350-550	300-400
Young modulus (GPa)	350-400	450-500	400-450	500-600	310-320
Compressive strength (GPa)	2-4	3-4.5	2.5-4	3.5-5	2-3
Density ($g \cdot cm^{-3}$)	3.9	2.5	3.2	4.5	3.3

Table 1: Mechanical properties of some of the most commonly used technical ceramics in the ballistic field.

Considering a cost/performance balance, alumina represents a good compromise among all technical ceramics.

1.3 Impact: fracture mechanisms

Before diving into the numerical study of alumina, it is useful to recall the mechanisms underlying the damage process of ceramics within dual-layer ballistic protections.
The response of a DHA to an impact is divided into two main parts: the shock response and the structural response ([17]). During the shock response, which lasts a few microseconds, waves propagate through the structure, causing the fragmentation of the ceramic and its possible detachment from the backing layer. At the moment when the projectile touches the surface of the ceramic, a wave propagates with a velocity on the order of 8000-10000 m/s. When this wave reaches the interface with the rear layer of the armor, it is partially reflected as a tensile wave, causing the fracture of the ceramic farthest from the impact point.

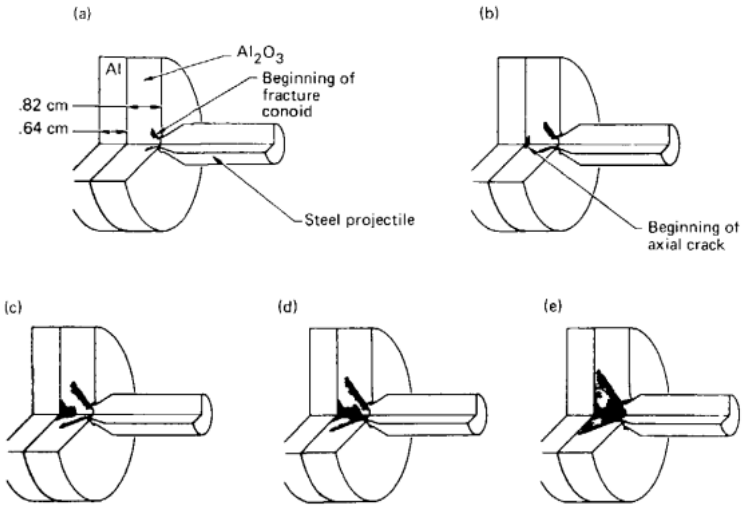

Figure 4: Development of axial and conic cracks in a double harness armour impacted by a bullet [17].

The structural response follows the shock response and involves the erosion of the projectile tip, which is deformed by contact with the ceramic. The fractured ceramic is then pushed against the backing, which bends, absorbing the kinetic energy and sustaining damage.
The projectile advances inside the ceramic, undergoing a process of deformation and erosion, while conical shear fractures progressively form, propagating from the interface towards the projectile. It should be noted that the fracturing of the ceramic itself is a process that absorbs only a very small amount of energy: the majority of the kinetic energy, in this initial phase, is dissipated by the displacement of the ceramic debris.
It has been demonstrated ([19]) that the initial resistance of the ceramic to the penetration of a projectile is primarily provided by its compressive strength, which determines the level of damage and plastic deformation of the impacting object. If the compressive strength of the projectile is significantly lower than that of the ceramic, a complete fragmentation of the projectile occurs; however, this also depends on its total length and other geometric characteristics.
The erosion and plastic deformation of the projectile during the first phase of impact is crucial in reducing its penetrative power and mainly depends on the hardness of the ceramic: for this reason, the goal is always to have a hardness of the first layer as high as possible compared to that of the impacting body.
The elastic and shear moduli are crucial during the initial shock phase, as the velocity of impact wave propagation depends on these properties; therefore, using very stiff materials is preferable. A property that plays a significant role in the fragmentation of the ceramic is undoubtedly shear strength, which is closely interconnected with the thickness of the layer. This thickness must be sufficiently high relative to the dimensions of the projectile, as shear strength is dependent on the stressed volume, and there are significant gradients between the area immediately beneath the impact point (compression) and the peripheral regions subjected to tension.
Finally, a crucial role is played by the Hugoniot Elastic Limit (HEL), which represents the elastic limit

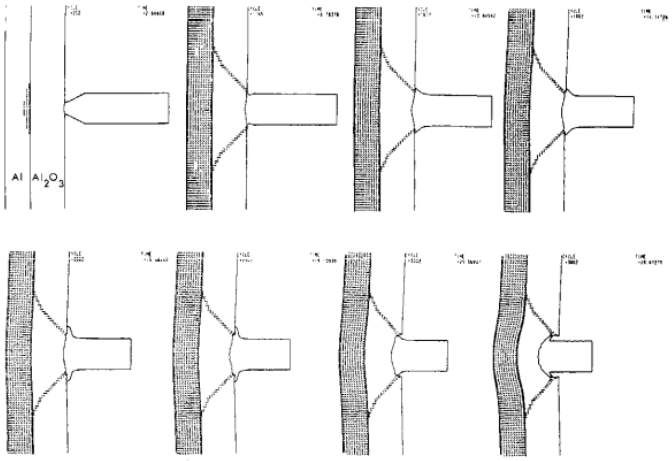

Figure 5: Penetration scheme of the projectile in the double harness armour during the structural response of the structure: the kinetic energy is absorbed by the backing while the projectile tip is eroded by the impact with ceramic front layer [17].

of a material subjected to uniaxial dynamic loading ([15]). In the early stages of impact, the generated shock waves transmit high pressure to the impacted material. If this transient pressure exceeds the HEL value, the material enters a phase of plastic deformation or fracture, losing its ability to respond elastically.
We can further divide the shock response of the material into a sequence of different stress states ([4], [14], [5]): in the first phase, a spherical wave originates from the impact point, propagating through the ceramic plate and subjecting the material to stresses on the order of GPa. This initial wave interacts with the ceramic before any other physical interaction between the alumina and the projectile and subjects the material to a hydrostatic compression characterized by very high pressures and strain rates. During this phase, it is possible for the stress to exceed the Hugoniot Elastic Limit, leading to the activation of fracture mechanisms due to compression, such as microplasticity and microcracking ([14]). Meanwhile, the projectile, which has just come into contact with the material and generated the wave, begins to sustain damage.

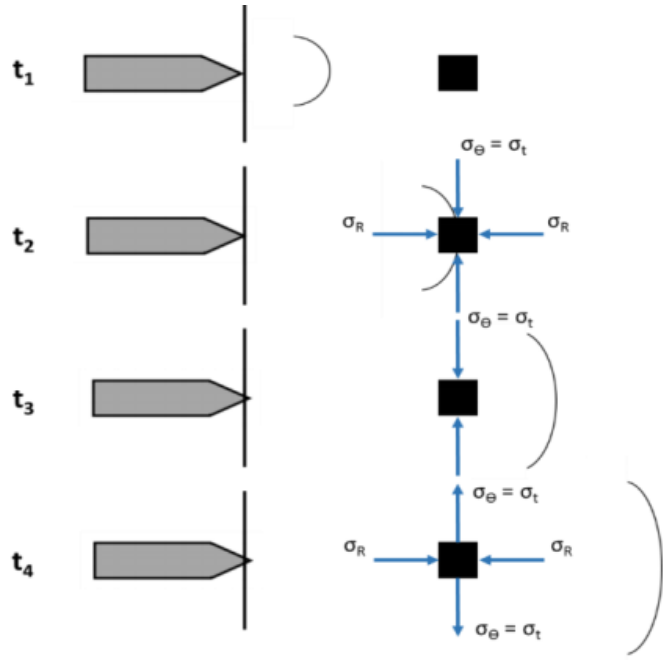

Figure 6: Stress on the volume elements caused by the compression wave passage following an impact [4].

The second phase follows the passage of the compression wave and is characterized by a biaxial compression/tension stress: a radial deformation of the material occurs due to the previous compression of the wave. The tensile stresses lead to material failure with multiple fracturing that follows the preferential directions of the stresses.
The final phase is the one in which the projectile penetrates into the already fragmented ceramic. These phenomena of fracture, fragmentation, and dissipation of impact energy by the ceramic constitute a very complex mechanical response to model numerically. Among the most commonly used numerical models for simulating the dynamic response of ceramics, we find the Johnson-Holmquist 2 ("JH2") model, widely used in the ballistic field, which allows us to describe the nonlinear plasticity behavior of alumina ceramic by taking into account its compressive strength, fracture propagation, and the progressive reduction of mechanical properties due to damage accumulation.
The operation of this numerical model is analyzed in the next chapter. As a practical example, three parameter sets from the literature are introduced, for which an initial comparison is provided on a single mesh element.

2 JH2 model

Ceramic materials can be considered to exhibit elastic-brittle behavior under static or quasi static loads. However, when subjected to ballistic impacts, their plastic response (post-yield response) can become significant.
One of the most commonly used models to represent the post-yield behavior of ceramic materials is the model developed by Johnson and Holmquist, which incorporates damage effects by modifying the strength of the ceramic during and after compression failure. This family of numerical models are commonly called "softening plasticity models".
Several constitutive equations have been developed based on the initial model (Johnson-Holmquist 1 [11]), which was later improved by adding a progressive damage model in the version known as "JH2" [12]. Finally, further developments were introduced with the JH2-V model [20].
The present work employs the JH2 model, whose robustness is well established due to its extensive use in the simulation of ceramic materials.
The JH2 model considers the effect of strain rate and damage accumulation within its equations and is capable of simulating the fracturing and weakening process of the material up to failure and, eventually, the complete removal of the excessively distorted mesh element.
The model consists of three components: an equation of state, a strength model, and a damage model.

2.1 JH2 model equations

2.1.1 Equation of state

The equation of state describes the relationship between the hydrostatic pressure "P" and the volumetric strain of the material "μ":

$$P = K_1\mu + K_2\mu^2 + K_3\mu^3 \quad \text{(Compression)} \tag{1}$$

$$P = K_1\mu \quad \text{(Tension)} \tag{2}$$

With K_1 as the bulk modulus of the material, K_2 and K_3 as material constants, and $\mu = \frac{\rho}{\rho_0} - 1$ as the volumetric strain (ρ_0 being the initial density).
A common definition for the initial bulk modulus K_1 in the Johnson-Holmquist II model is given by the relation:

$$K = \frac{E}{3\,(1-2\nu)}$$

where E is Young modulus and ν Poisson coefficient.
After the material begins to be damaged, the ceramic undergoes local deformation and radial expansion, making it necessary to add a term Δp to the initial polynomial equation of state:

$$P = K_1\mu + K_2\mu^2 + K_3\mu^3 + \Delta P_{t+\Delta t} \tag{3}$$

This correction allows the model to redistribute the pressure on the elements following damage, reducing it. The equation of state directly influences the stress on the elements and must therefore be updated according to the level of damage, just like all other quantities in the model. From an energetic point of view, there is a conversion of elastic energy into internal energy "absorbed" by the elements as a result of the damage, according to the equation:

$$\left(\Delta P_{t+\Delta t} - \Delta P_t\right)\mu_{t+\Delta t} + \frac{\Delta P_{t+\Delta t}^2 - \Delta P_t^2}{2K_1} = \beta \Delta U \tag{4}$$

With β as the conversion factor from elastic energy to potential energy and U as the potential energy. $\Delta P_{t+\Delta t}$ therefore corresponds to the bulking pressure of the material and is determined by the amount of accumulated damage according to the following equation (obtained directly by inverting the previous one):

$$\Delta P_{t+\Delta t} = -K_1\mu + \sqrt{\left(K_1\mu + \Delta P\right)^2 + 2\beta K_1 \Delta U} \tag{5}$$

The parameters of the equation of state can be determined through curve fitting of the P-μ graph obtained from plate impact tests. In the parameter set used in this work (as in all sets found in the

literature, see next), β is set to unity: it is therefore assumed that the loss of internal elastic energy is entirely converted into potential energy.
Physically, the equation represents the "release" of part of the elastic energy, which can no longer be stored in the material due to the microcracks produced by the damage.

2.1.2 Strength model

The strength model expresses the equivalent stress σ^* (normalized with respect to the Hugoniot elastic limit stress σ_{HEL}) as a function of the hydrostatic pressure given by the equation of state and relates it to the strain rate and the damage factor "D".
The dimensionless strength model is defined by:

$$\sigma^* = \sigma_i^* - D\left(\sigma_i^* - \sigma_f^*\right) \tag{6}$$

With σ_1^* and σ_f^* representing, respectively, the intact material equivalent stress (D=0) and the fractured material equivalent stress (D=1):

$$\sigma_i^* = A\left(p^* + \sigma_{t,m}^*\right)^N \left[1 + C\ln\left(\dot{\varepsilon} + \dot{\varepsilon}_0\right)\right] \tag{7}$$

$$\sigma_f^* = B\left(p^*\right)^M \left[1 + C\ln\left(\dot{\varepsilon} + \dot{\varepsilon}_0\right)\right] \tag{8}$$

The strength model thus updates the material resistance proportionally to the damage level D, based on the initial resistances of the intact and fully fractured material, which in turn depend on the hydrostatic pressure (by EOS), deviatoric stress, and strain rate according to material-specific constants (A, B, C, M, N).
The fractured strength σ_f^* is increased by the user-defined parameter σ_{fmax}^* (maximum fractured strength).
The normalized values appearing in the formulas are given by:

$$p^* = \frac{p}{p_{\text{HEL}}}, \quad \sigma_{t,m}^* = \frac{\sigma_{t,m}}{p_{\text{HEL}}}, \quad \sigma^* = \frac{\sigma}{\sigma_{\text{HEL}}}$$

With p_{HEL} as the hydrostatic pressure at the Hugoniot Elastic Limit (σ_{HEL}) and $\sigma_{t,m}$ as the maximum hydrostatic tensile stress that the material can withstand.
We can calculate $\sigma_{t,m}$ using [10]:

$$\sigma_{t,m} = \frac{T}{3}\frac{1+\nu}{1-\nu}$$

The constant C associated with the strain rate effect can be obtained by a uniaxial dynamic compression tests (for example Split Hopkinson Kolsky Bar).

2.1.3 Damage model

The JH2 model represents damage as a state variable "D" defined as the average damage over each volumetric mesh element. This variable evolves as the material undergoes deformation and is then used to degrade the strength properties and the elastic modulus of the ceramic. In particular, damage begins to accumulate when the deviatoric stress exceeds a critical value.
It should be noted that the damage variable does not control the erosion of the mesh element during the simulation; instead, this is managed by the parameter "FS" ("Failure Strain"), details of which will be provided later.
The damage variable D can be expressed as:

$$D = \sum\left(\frac{\Delta\varepsilon_p}{\varepsilon_p^f}\right) \tag{9}$$

with $\Delta\varepsilon_p$ as the integral of the plastic strain in a single cycle and ε_p^f as the crushing plastic strain of the material (plastic strain at failure): the onset of plastic deformation coincides with the initiation of damage in the element.

$$\varepsilon_p^f = \frac{D_1\left(p^* + \sigma_{t,m}^*\right)}{D_2} \tag{10}$$

For this reason, it is possible to monitor the damage state of the material by analyzing the output PEEQ - Plastic Equivalent Strain - available in Abaqus.
ε_p^f introducts the two damage coefficients D_1 and D_2. Due to the extremely brittle nature of ceramics, it is difficult to obtain experimental values for D_1 and D_2, which must therefore be determined by comparing numerical simulations with experimental results.
Summarizing, the main steps of the model are:

- Initial calculation of the volumetric strain (μ) from the contact pressure (P):

$$P = K_1\mu + K_2\mu^2 + K_3\mu^3 + \Delta P_{n-1}$$

  From this relation, μ is obtained, assuming that initially $\Delta P_{n-1} = 0$ (no previous variation).
  In tension this equation is reducted to:

$$P = K_1\mu$$

- Damage update (D): The incremental damage is calculated based on the accumulated equivalent plastic strain:

$$D = \sum \left(\frac{\Delta\varepsilon_p}{\varepsilon_p^f} \right)$$

  Where:

$$\varepsilon_p^f = \frac{D_1 \left(p^* + \sigma_{t,m}^*\right)}{D_2}$$

- Update of the equivalent stress (σ^*) with the new damage level:

$$\sigma^* = \sigma_1^* - D\left(\sigma_i^* - \sigma_f^*\right)$$

  Where:

$$\sigma_i^* = A\left(p^* + \sigma_{t,m}^*\right)^N \left[1 + C\ln\left(\dot{\varepsilon} + \dot{\varepsilon}_0\right)\right]$$

$$\sigma_f^* = B\left(p^*\right)^M \left[1 + C\ln\left(\dot{\varepsilon} + \dot{\varepsilon}_0\right)\right]$$

- Update of the pressure variation (ΔP_{n+1}): The pressure is updated considering the accumulated internal energy:

$$\Delta P_{n+1} = -K_1\mu + \sqrt{\left(K_1\mu + \Delta P\right)^2 + 2\beta K_1 \Delta U}$$

- Calculation of the total stress (σ_{ij}), computed by combining the hydrostatic pressure and the deviatoric stress:

$$\sigma_{ij} = -P\delta_{ij} + s_{ij}$$

  Where s_{ij} is the deviatoric stress calculated based on the accumulated plastic strain.

- Update of state variables: All internal variables are updated for the next step, including:
  - Volumetric strain (μ).
  - Pressure (P).
  - Equivalent plastic strain (ε_p).
  - Damage (D).
  - Pressure variation (ΔP).

2.2 Material parameters

2.2.1 Parameters set by literature

It is extremely difficult to characterize a set of parameters for the behavior of ceramics due to the extremely brittle nature of the material, which makes it challenging to extrapolate and correlate experimental data with numerical models.
Because of this, many parameter sets have been proposed in the literature for the alumina examined in this study. Therefore, three studies on alumina have been considered, from which three simulation parameter sets for the JH2 model have been derived.
It's necessary to note that the various parameters used in the analyzed studies were obtained partly through direct measurements of experimental values (e.g. HEL) and partly through progressive calibration of numerical simulations (e.g. D_1, D_2).
This introduces uncertainty into the data, both due to the different nature of the tests in the various studies (a dynamic impact test is extremely different from a static test) and to the different strategies adopted by the various authors to calibrate the models (also adjusting parameters in a iterative way to bring simulations closer to reality).
The result is a significant uncertainty regarding the values to be used and the presence of multiple sets of data that differ from each other but have nonetheless proven to be reliable in the various tests conducted by different authors.
In the present study, it was decided to consider three data sets, which will be named after the author of the paper from which they were extracted:

- "Holmquist": parameter set taken from the original presentation of the JH2 method by Holmquist and Johnson [12];
- "Nadal": set inherited from the previous study by Jordi Nadal of ISAE Supaero, of which this thesis is a continuation. The original source of this data set is [9];
- "Khan": set taken from the paper [13].

The parameters from the three sources are presented in the following table.

Material parameters	**HOLMQUIST [12]**	**NADAL [9]**	**KHAN [13]**
Density ρ_0 (kg/m^3)	3890	3890	3700
EOS			
Bulk modulus K_1 (GPa)	130.95	231	130.95
Pressure constant K_2 (GPa)	0	-160	0
Pressure constant K_3 (GPa)	0	2774	0
Strength model			
Shear modulus G (GPa)	90.16	152	90.16
Hugoniot elastic limit HEL (GPa)	2.790	6.570	19
Intact strength constant A	0.930	0.880	0.930
Intact strength exponent N	0.600	0.640	0.600
Strain rate constant C	0.000	0.000	0.000
Fracture strength constant B	0.310	0.280	0.310
Fracture strength exponent M	0.600	0.600	0.600
Normalized maximum fractured strength $\sigma_f^{\max}$	1.000	1.000	0.200
Pressure at HEL P_{HEL} (GPa)	1.460	1.460	1.460
Failure model			
Damage constant D_1	0.005	0.005	0.010
Damage exponent D_2	1.000	1.000	0.700
Bulking factor β	1.000	1.000	1.000

Table 2: JH-2 constitutive model parameters for alumina 99.5%

One of the main differences lies in the value of the Hugoniot Elastic Limit HEL, which greatly influences the behavior of the material under impact. The Hugoniot Elastic Limit describes the maximum pressure or stress that a material can withstand while maintaining an elastic behavior under

a shock wave or high-velocity load: when this threshold is exceeded, the material begins to deform plastically.
Consequently, a high HEL will result in a much more resistant material compared to an equivalent one with a lower one when subjected to impact loadings.
The objective is therefore to compare the collected data sets with the experimental results to determine which set is closest to our case.
First, all models were tested in Abaqus by simulating a single cubic mesh element. This allowed for a better understanding of both the characteristics of the different data sets and the numerical model.

2.2.2 Numerical model: cube

To analyze the material sets and the JH2 model behaviour, a similar but not identical simulation cube setting of the original Johnson and Holmquist paper is adopted [12]. Following the strain control with sawtooth load suggested by Gazonas [7], a strain control load is imposed instead of the original stress control setting on a single cubic mesh element with a side length of 1 m.
The cube is costrained on five sides (simple supported, Fig 7) and loaded on the sixth side with a sawtooth displacement function (Fig 8) defined as following:

$$\mu(t) = \frac{5tH(t)}{100} - \frac{(t-1)H(t-1)}{10}$$

With $H(t)$ as the Heaviside function defined as:

$$H(x) = \begin{cases} 0, & x < 0, \\ 1, & x \geq 0. \end{cases}$$

The result is a gradual compression on the only free side, followed by a subsequent release in tension.
A Matlab script has been used to generate the data for "Tabular amplitude" in Abaqus (2-second time and a maximum displacement of 50 mm at $t = 1$ sec). It is then possible to increase the maximum displacement if the material fracture is not achieved (which is necessary to visualize the complete behaviour of the damage model).

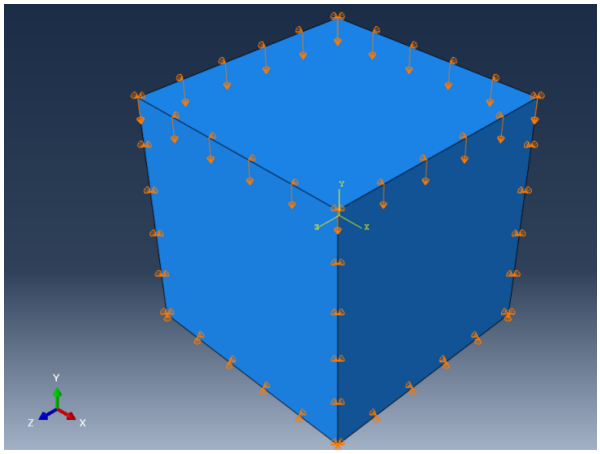

Figure 7: Cube constraints

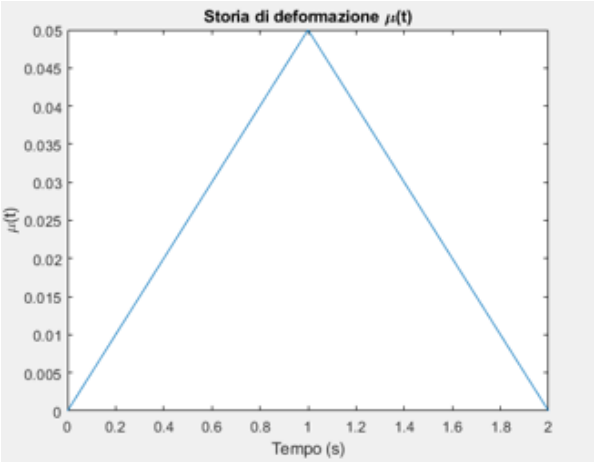

Figure 8: Sawtooth function [3]

The simulation is explicit dynamic with 3D explicit mesh element type. The options "convert to particles" and "element deletion" were not activated, and an initial FS of 0.2 was set as numerical parameters in the JH2 card model.
These precautions were taken to prevent the erosion of the element and thus avoid interruptions in the graphs due to excessive distortion: while this is necessary in impact simulations, here we want to observe the behavior of the model even in the post-fracture phase to compare it with the curves reported by Holmquist in the original paper [12].
The criteria for "element deletion" and "convert to particles" are indeed options that can be activated in the Abaqus mesh card, but the JH2 model already includes an internal erosion option by the parameter

"FS" ("Failure Strain"): when the plastic strain reaches the set value, the element will be removed from the calculation (but not from the graphical area: this is managed by the two Abaqus options).
It is necessary to carefully evaluate the activation of erosion criteria, as softening plasticity models like JH2 have shown a strong dependence on mesh size and, consequently, on the elimination of elements during the calculation. Alternative solutions have been implemented to mitigate this issue involving viscosity constitutive models (e.g. the JHB-V model [20]).

2.2.3 Holmquist cube

To verify the correct implementation of the JH2 Alumina model, the original parameters set from Johnson and Holmquist paper [12] was first simulated.
Figure 9 presents the "Effective stress-Pressure" graph of the mesh element from the original paper, overlaid with the two strength curves of the intact and fractured material (equations respectively 7 e 8).

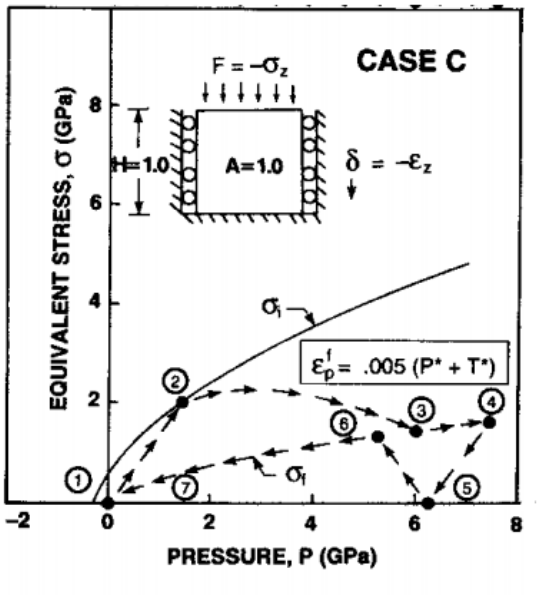

Figure 9: Original JH2 stress pressure plot [12].

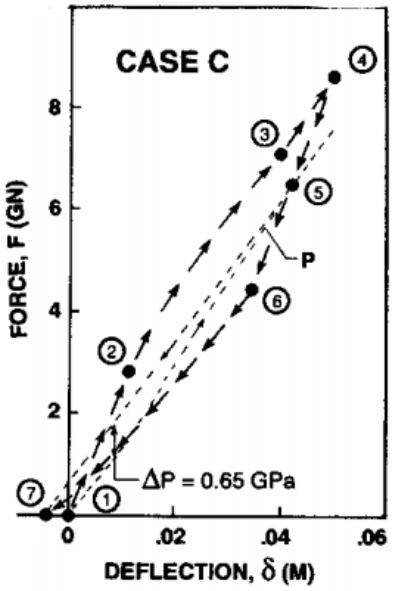

Figure 10: Original JH2 deflection-force plot (NE33-S33).

The quantities reported in the graph in 9 are the hydrostatic pressure on the x-axis ("Equivalent pressure" in Abaqus) and the equivalent stress on the y-axis ("Mises equivalent stress" in Abaqus).
By analyzing the different areas of the graph, it is possible to distinguish the material behaviour under stress and deduce the effects of the model parameters.
Starting from the stress-free state (point 1), the material begins to elastically load until it reaches point 2, which intersects the strength curve of the intact material (equation 7). Having reached the failure limit, the material starts to degrade, weakening progressively as damage accumulates from point 2 ($D = 0$) to point 3 ($D = 1$), where the fracture strength curve is intersected (equation 8).
The material continues to plastically flow from point 3 to point 4 along the fracture strength curve and reaches its maximum pressure at point 4, corresponding to the maximum compression set by the load of $\mu = 0.05$.
Here, the compression phase ends, and the tensile release begins: the material unloads elastically from point 4 to point 5, following the same slope as in compression (since the Young modulus remains unchanged and is not modified by damage) until it reaches a zero-stress condition. From point 5 to point 6, a tensile load is applied, and the axial deviatoric stress becomes tensile.
This occurs because, during the damage process, the material properties have changed, and the zero-stress condition is now intermediate in the compression release path: at the midpoint of the release, a tensile stress develops on the loaded side to return to the initial position.
The fracture stress is reached again (this time in tension) at point 6, and the material continues to plastically unload along the envelope of the fracture strength curve until point 7 (it cannot exceed its strength curve and thus plastically flows along it).

By simulating the "Holmquist" parameter set (column 1 of Table 2) and plotting the quantities, we observe the expected behavior:

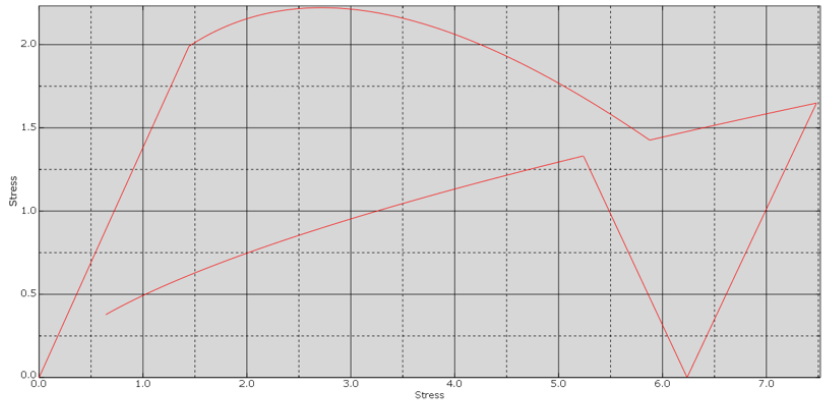

Figure 11: Equivalent pressure-equivalent stress Holmquist model in Abaqus cube simulation.

It should be noted that in our test, the stresses do not return to zero as in the example provided in Johnson and Holmquist [12] because the former is under strain control and there are residual stresses induced by yielding, whereas the latter is under stress control.
For a complete comparison with the original model, the stress-strain graph is shown in Figure 12.

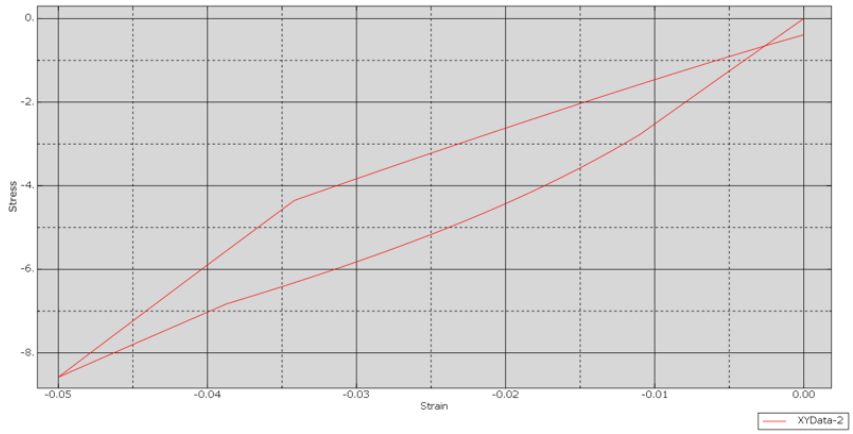

Figure 12: Deflection-stress Holmquist model in Abaqus cube simulation (NE33-S33)

The verification of this model in Abaqus has been extremely helpful in understanding how the parameters influence the material behavior and in the simulations of subsequent cases.

2.2.4 Khan cube

Observing the parameter set of Khan (2), we see that the main difference lies in a significantly higher Hugoniot Elastic Limit compared to the Holmquist case: 19 GPa instead of 2.79 GPa.
An immediate consequence of this is a considerable increase in the load level that the material can withstand in the elastic field: therefore, to analyze the entire model and observe all the curves identified in the Holmquist case, it is necessary to increase the imposed displacement.
In particular, this parameter set required a displacement load five times greater than that imposed in the previous case: the maximum displacement at $t = 1$ second is 0.250 m (25%) instead of 0.05 m (5%).
Clearly, since alumina is an extremely brittle ceramic material, it is unrealistic not to have failure up to such a load level. However, it must be considered that the model derives its parameters from a high-impact experimental calibration (in Khan's study, an impact on a plate at 275 m/s is simulated) and may not be suitable for a static load simulation like the present one.
Setting a unitary FS (which means that erosion within the JH2 routine occurs with an element deformation of 100% - in other words, it practically does not occur) allows visualizing the entire curve of elastic loading - damage accumulation - plastic flowing - and tensile load unloading (figure 11).

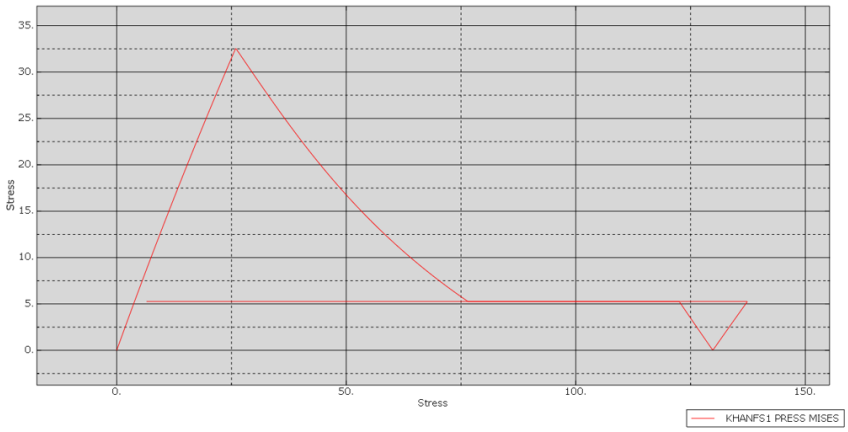

Figure 13: Equivalent pressure-equivalent stress Khan model in Abaqus cube simulation.

For completeness, figure 14 presents the strain-stress graph of the element to be compared with the Holmquist model curves in figures 10 and 11.

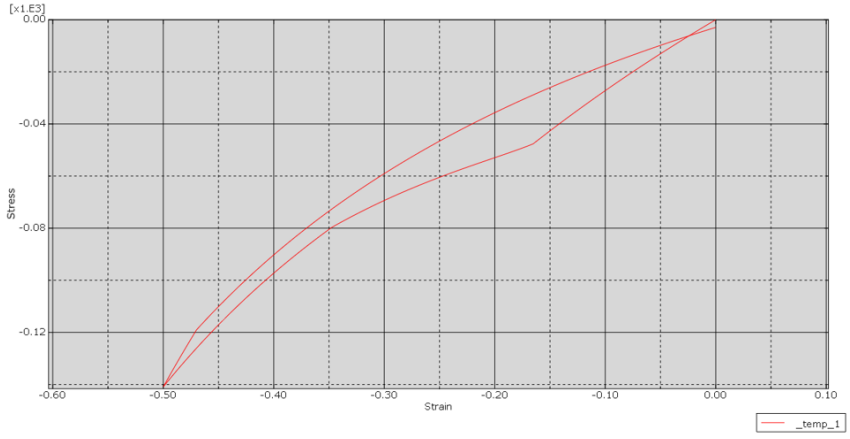

Figure 14: Deflection-stress Khan model in Abaqus cube simulation (NE33-S33).

From the graphs, we can see that the Khan model tolerates a very higher tensile stress compared to the Holmquist model before undergoing damage, which occurs only after an equivalent Mises stress of over 30 GPa (compared to approximately 2.5 GPa for Holmquist).
This is perfectly consistent with the really high HEL value of this parameter set, but obviously unrealistic for static loadings.

2.2.5 Nadal cube

Similarly to the case of Khan, this set also features a significantly higher HEL value compared to Holmquist one (see table 2), and it was therefore necessary to increase the imposed displacement from the original 0.05 m to 0.125 m (strain from 5% to 12.5%), obtaining a trend similar to that of Khan (but at a lower stress level), as can be seen in figure 16.

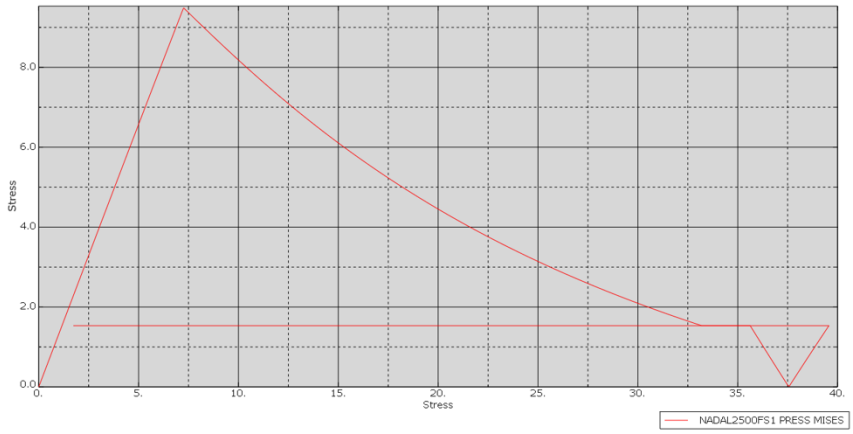

Figure 15: Equivalent pressure-equivalent stress Nadal model in Abaqus cube simulation.

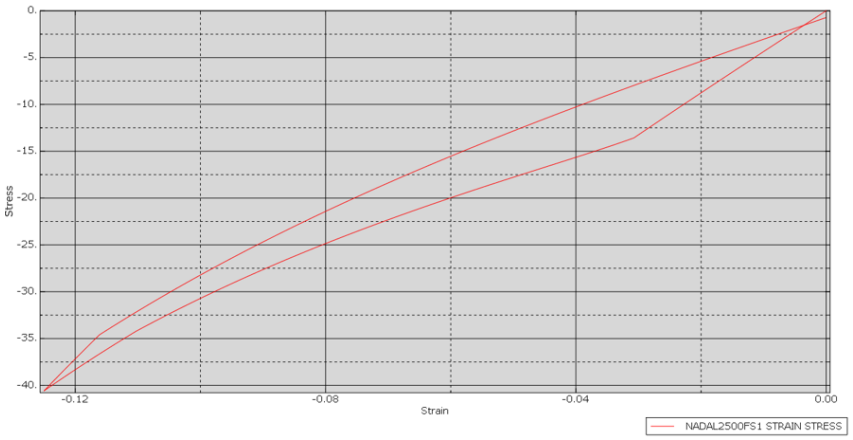

Figure 16: Nadal JH2 deflection-force plot (NE33-S33).

Figure 17 presents the qualitative comparison of the behavior obtained with the three parameter sets (note that that extremely different displacements were imposed: 0.05 m for the Holmquist case, 0.125 m for Nadal and 0.250 m for Khan).

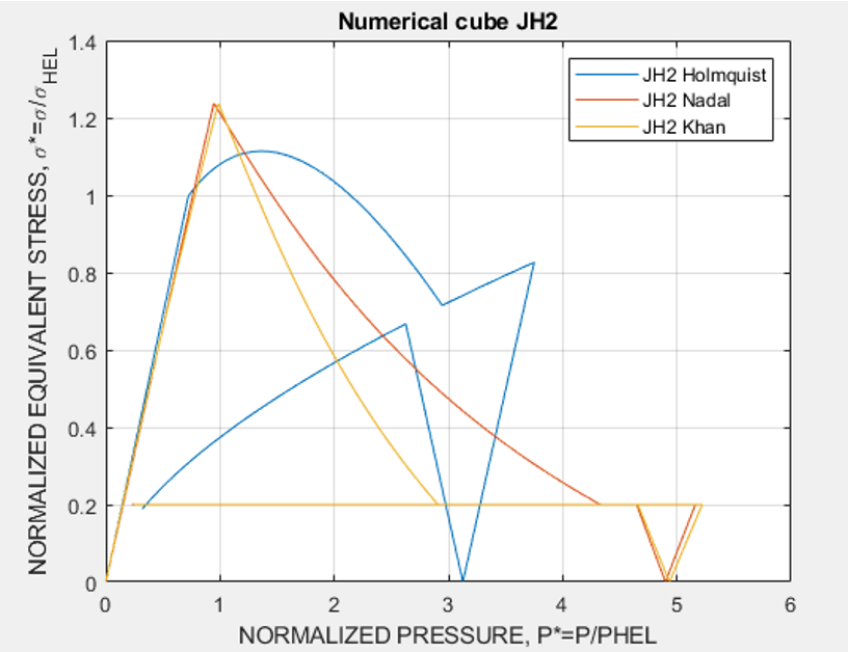

Figure 17: Pressure-stress JH2 cube comparison with different material set.

3 Three point bending test

In order to characterize the ceramic in static behaviour and obtain material data, an initial test campaign was conducted on a three-point bending test. This is necessary because even within the same material (aluminum oxide Al_2O_3), significantly different mechanical properties can be observed (as seen in the various parameter sets reported in Table 2), mainly due to different manufacturing processes. The three-point bending test is one of the most commonly used methods for material characterization and allows for the determination of some fundamental parameters such as Young modulus E (and consequently, through knowledge and/or assumption of the Poisson ratio, the shear modulus G), the modulus of rupture MOR, which is the flexural failure load, and the ultimate tensile strength UTS.

3.1 Experimental experience

3.1.1 Experimental settings

In the three-point bending test, the specimen is positioned on two lateral cylindrical supports and is loaded in the center by a third cylinder. This results in the typical "butterfly" stress distribution, with tensile stress in the lower part and compressive stress in the upper part. The neutral plane, coinciding with the mid-thickness plane is instead characterized by a null stress state.

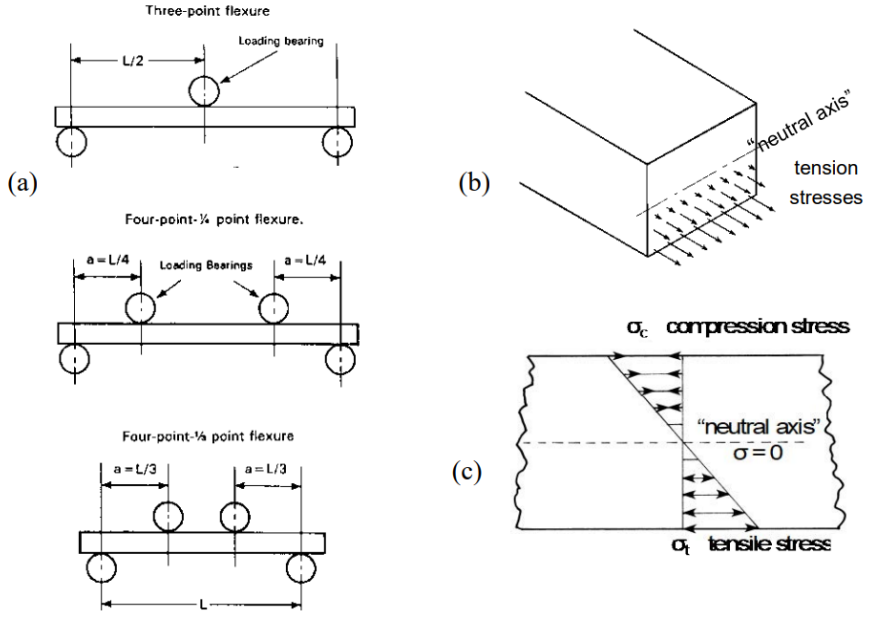

Figure 18: Stress distribution in the material in three and four point bending tests.

The test was carried out on a prismatic specimen with a rectangular base of 6x10 mm and a length of 90 mm. The supports of the testing machine (an Instron 6800 machine for tensile, torsion, and bending tests [10]) were placed at a distance of 80 mm so that the ends of the specimen extend by half a centimeter on each side, as shown in figure 19.

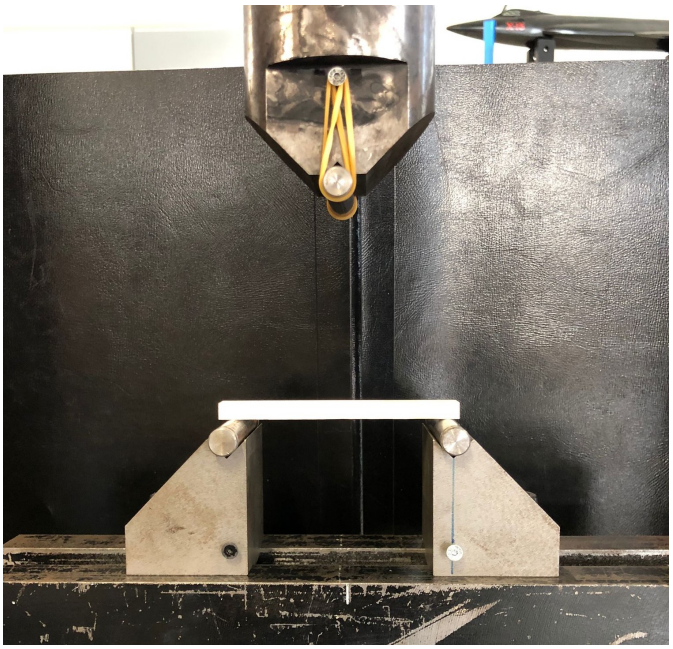

Figure 19: Three point bending test.

The test was carried out on 5 specimens: given the low variability of the obtained results, this number was considered sufficient for the characterization of the material. The fracture occurred in an extremely brittle manner in all specimens, and all tests were considered acceptable as the fracture developed in the central part (as required by the standard). It was initially assumed that the crack developed on the lower side (the tensile side), since the tensile strength of ceramic materials is typically much lower than their compressive strength. This hypothesis was later validated through microscopic observation of the specimens: refer to chapter 3.1.3 for the analysis of the fracture mechanism.
Figure 20 shows images of the specimens after fracture.

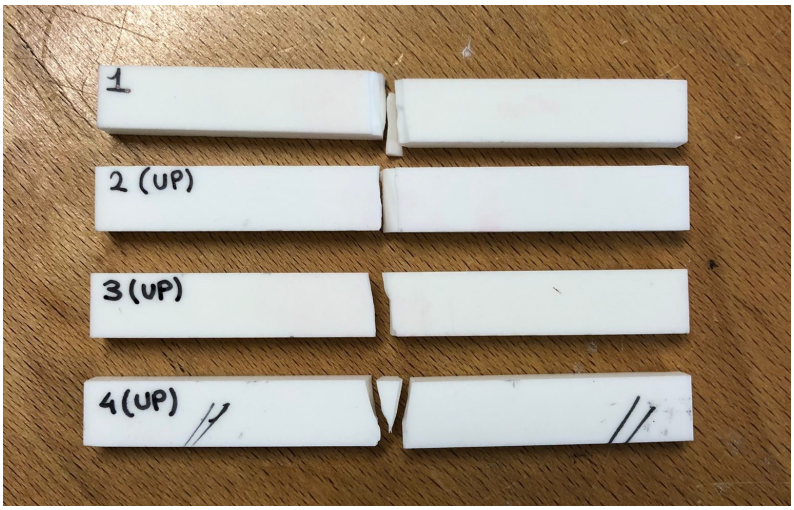

Figure 20: Specimen 1, 2, 3 and 4 after the test.

3.1.2 Test results and data analysis

The force-displacement data of the loading pin have been acquired and their plots post-processed using a Matlab algorithm are presented in figure 21.

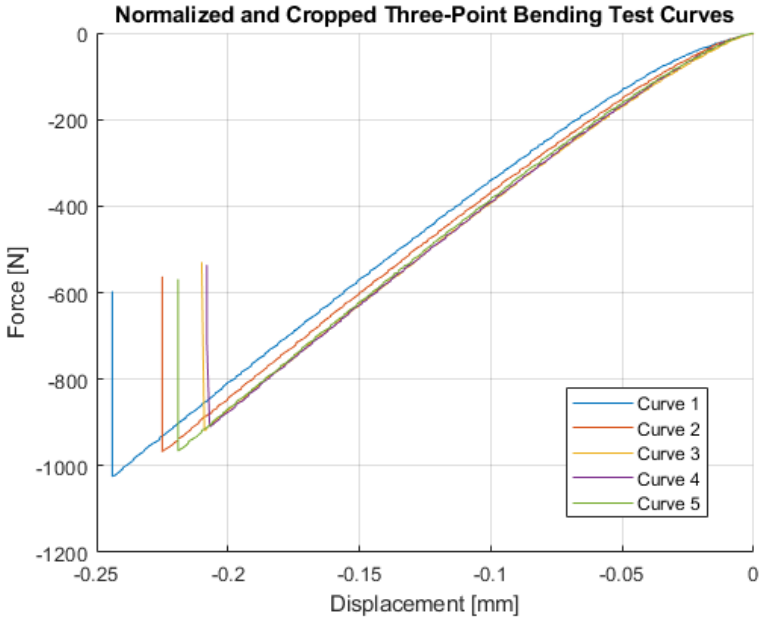

Figure 21: Three point bending test force displacement plot.

From the test various quantities of interest can be obtained. While the modulus of rupture MOR is given by the maximum load reached during the test, for the calculation of Young modulus E, modulus of rupture MOR and shear modulus G, it is sufficient to apply Hooke law and the formulas derived from De Saint Venant theory.
The formulas used in the Matlab script are briefly recalled below.
Defining:

- F_{max}: Maximum applied force;
- L: Distance between the supports;
- b: Width of the specimen;
- d: Thickness of the specimen.

We obtain that the maximum bending stress MOR is given by:

$$MOR = \frac{3F_{max} \cdot L}{2b \cdot d^2}$$

The elastic modulus E can be obtained from the relation:

$$E = \frac{L^3}{4b \cdot d^3} \cdot \frac{F}{\delta}$$

Where:

- F: Force in the elastic region;
- δ: Deflection (displacement at the center of the beam).

The shear modulus G is related to the elastic modulus E and the Poisson ratio ν by:

$$G = \frac{E}{2(1+\nu)}$$

By implementing these formulas in a Matlab script, we obtain the following average values:

- **Maximum flexural strength (MOR)**:

$$MOR = 319\,\text{MPa}$$

- **Elastic modulus (E)**:

$$E = 275\,\text{GPa}$$

- **Shear modulus (G)**:

$$G(\nu = 0.10) = 124.8\ \text{GPa}$$
$$G(\nu = 0.21) = 114.5\ \text{GPa}$$
$$G(\nu = 0.25) = 110.5\ \text{GPa}$$

It should be noted that the values of G were obtained by assuming three different Poisson ratios ν, specifically $\nu = 0.10$, $\nu = 0.21$ and $\nu = 0.25$.
By comparing the calculated values with those found in the literature, it is considered that a Poisson ratio of 0.21 is the most representative of the material. Therefore, we will use the data set obtained with this value as a reference for the subsequent models.
It should also be noted that the maximum flexural strength MOR can be used to estimate the ultimate tensile strength UTS. Specifically, for brittle materials, the following relationship holds:

$$UTS \approx k \cdot MOR$$

with k as an empirical factor ranging between 0.6 and 0.9 ([18]). Assuming an average between the maximum and minimum values, we can use $k = 0.75$ for an estimate of UTS:

$$UTS \approx 0.75 \cdot MOR = 0.75 \cdot 319 = 240\,\text{MPa}$$

The value is in line with those reported in the literature.
The derived quantities are presented in table 3.

Property	**Value**
Young modulus (E)	275 GPa
Maximum flexural strength (MOR)	319 MPa
Shear modulus (G)	114.5 GPa
Ultimate tensile strength (UTS)	240 MPa

Table 3: Mechanical properties calculated with $\nu = 0.21$.

3.1.3 Fracture analysis of the specimens

Optical microscope analysis

The specimens were analyzed under an optical microscope to identify the fracture zones and validate the initial hypothesis (i.e. fracture initiation on the lower tensile side).
This instrument is capable of magnifications up to 2000 times and can generate a three-dimensional model of the fracture surface.
As we know, ceramics are extremely brittle materials: fracture during the bending test is sudden and occurs at the location of the maximum bending moment, which is just below the loading pin. As observed in figure 20, all tested specimens confirmed this behavior but exhibit slight differences in the fracture mode, which are worth investigating.
In specimens subjected to bending tests (whether three-point or four-point), it is possible to identify some recurring characteristics: the fractured surface often exhibits a compression curling effect in the upper region and a different surface pattern depending on the location and mode of fracture [8].
Figure 22 presents examples of compression curling in specimens subjected to four-point and three-point bending (cases b and d): once the fracture initiated from the tensile side, it propagates to

the compressive one, slowing down and changing direction, possibly bifurcating and creating a third fragment (cases c and e).

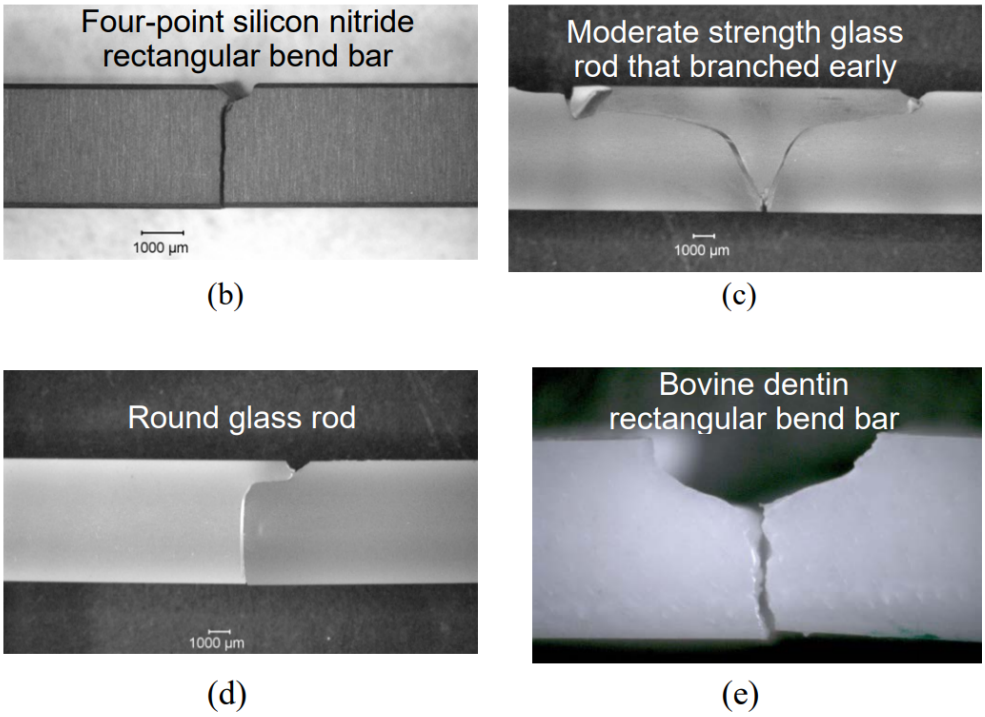

Figure 22: Typical compression curling in specimens fractured under bending [8].

The presence of this type of pattern in the fracture is therefore a confirmation of tensile failure in the lower part of the specimen. Qualitatively, the presence of a compression curling effect can be associated with a low-energy failure, while its rupture and the creation of a third fragment indicate a slightly higher fracture energy. However, the potential central fragment is not of significant interest, as it never hosts the crack initiation ([8]).

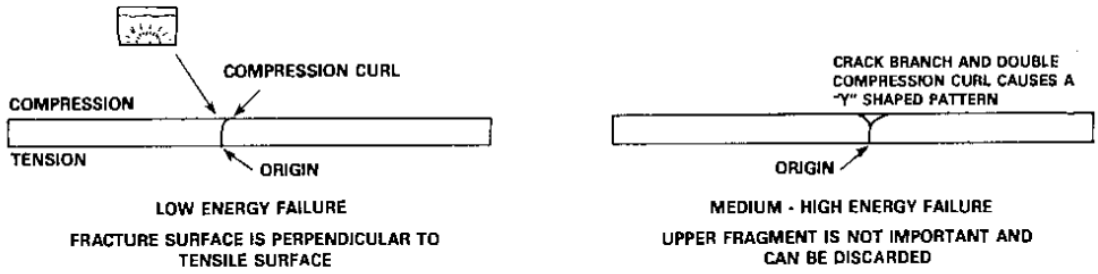

Figure 23: Main fracture modes in three-point and four-point bending tests [8].

Not all tested specimens exhibit the compression curling effect or the same fracture pattern. Specifically:

- Specimen 2 (figure 24) and specimen 3 (figure 25): the fracture presents the typical "compression curling" in the upper region subjected to compression, dividing the specimen into two parts;
- Specimen 1: the fracture is similar to that of specimens 2 and 3, but the compression curling collapses and detaches, forming a third fragment. The fracture phenomenology can therefore be traced back to the previous cases;
- Specimen 4: the fracture is anomalous compared to the previous ones, as it propagates from the left side, bifurcating and creating a third fragment not due to weakening from compression curling;

- Specimen 5 (Fig. 26): the fracture is very similar to that of specimen 1, but with only a partial detachment of the portion affected by compression curling (it does not completely detach, but chipping occurs on one side). In any case, the nature of the fracture remains the same.

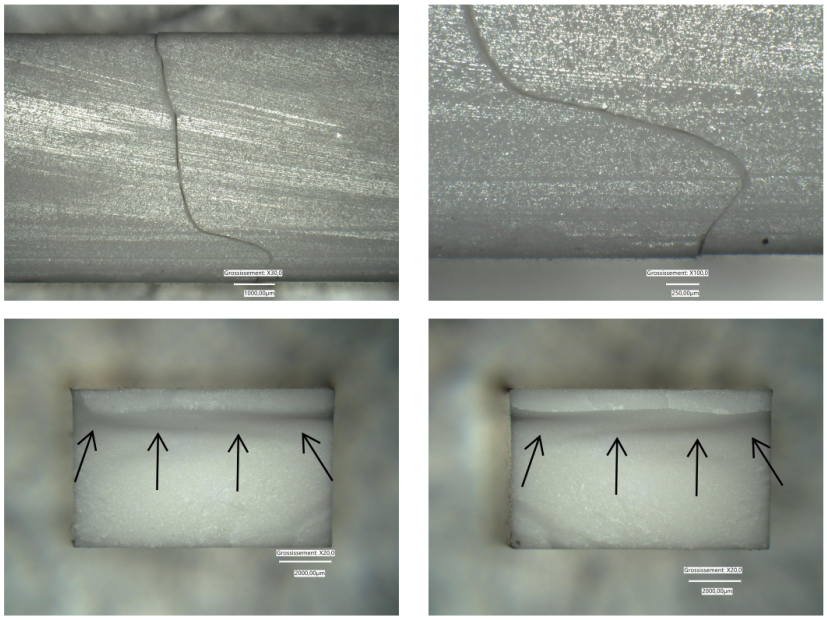

Figure 24: Compression curling specimen 2. The load is applied to the upper side of the specimen.

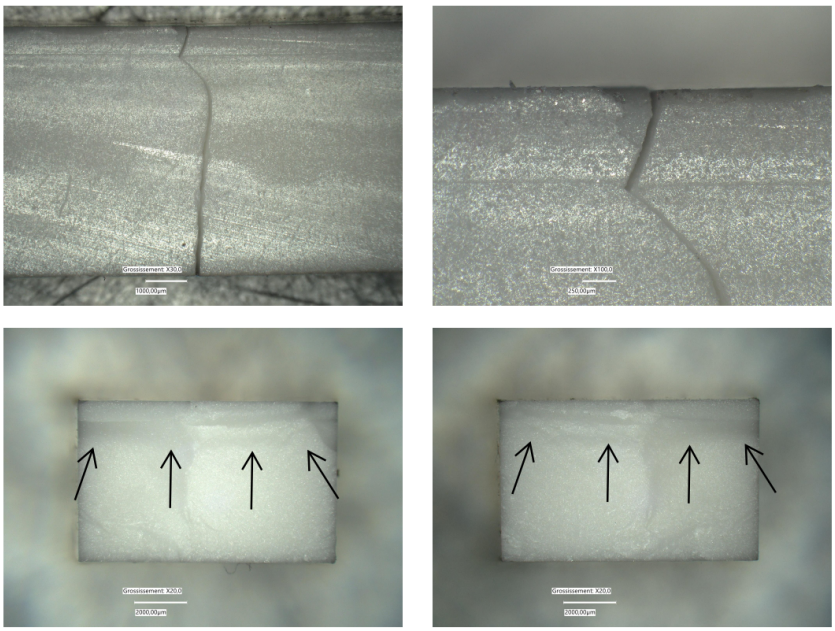

Figure 25: Compression curling specimen 3. The load is applied to the upper side of the specimen.

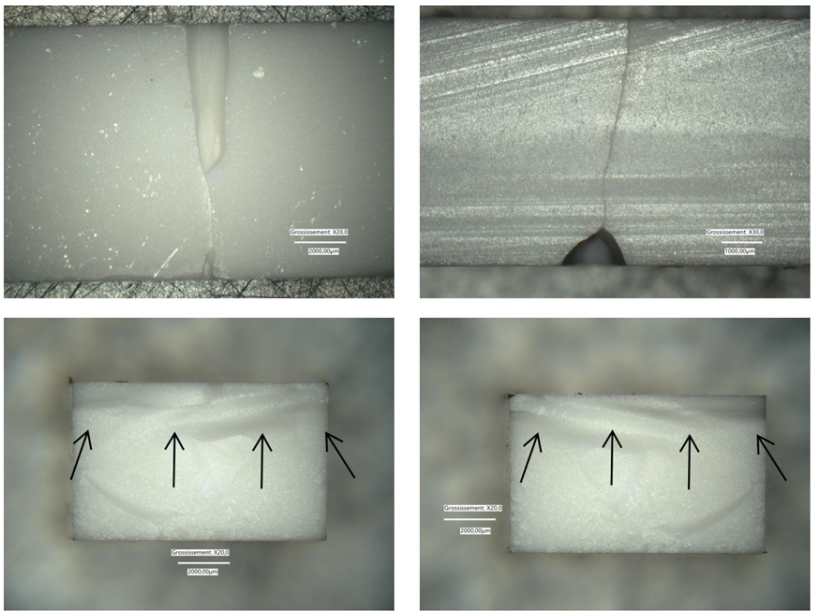

Figure 26: Compression curling specimen 5. The load is applied to the upper side of the specimen.

The presence of the compression curling in the upper region of the specimen already allows us to validate the initial hypothesis of tensile failure on the lower face (thus confirming the value of Ultimate Tensile Strength). From the literature [8], the fracture phenomenology of ceramics under bending is well established: fracture nucleation originates from a defect on the tensile side, then propagates through the thickness first in a transgranular manner and later in an intergranular fashion.
An example of fractographic analysis is shown in Fig. 27.

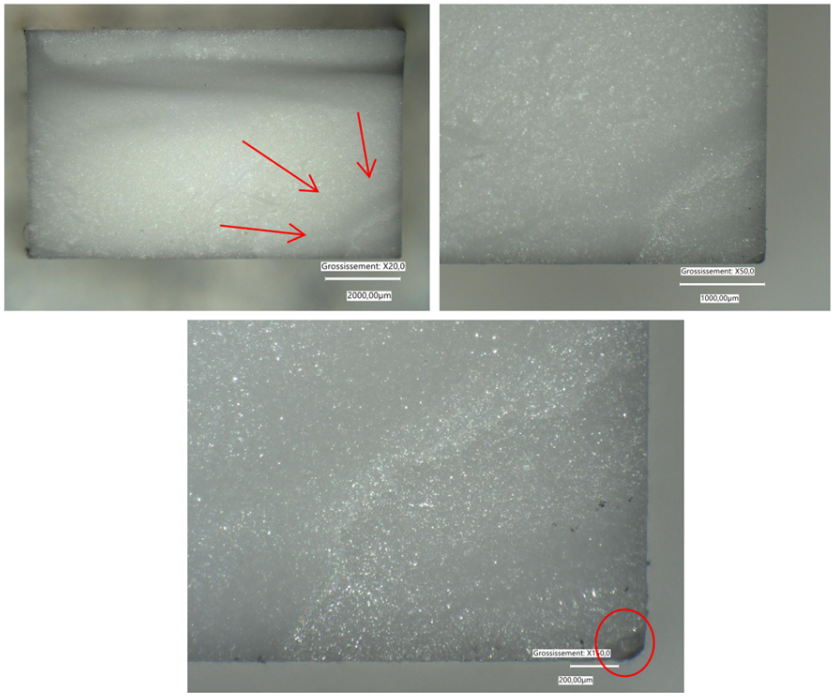

Figure 27: Probable nucleation point of specimen number 2. "Waves" are visible radiating from the lower right corner, where there is a defect due to the cutting of the specimen. The lower surface of the fracture appears homogeneous and relatively smooth (it is the "mirror"), while moving away from this, the surface becomes rougher and less regular.

The two modes influence the surface appearance in different ways: in the area closest to the crack initiation (transgranular fracture), the surface often appears smoother and shinier (and for this reason is called "mirror") because here the crack moves through the ceramic grains along cleavage planes with relatively regular and controlled propagation. In the farther area, however, the crack tends to advance in an intergranular manner along the grain boundaries creating a more irregular surface and thus a more opaque and rough texture.
Figure 28 shows an example of fractographic analysis. The specimen is number 4: here a large central fragment detached not due to compression curling but rather due to the bifurcation of the crack in its transverse development.
Although in this case the crack nucleation point was not immediately visible, by analyzing the appearance of the fracture surfaces it was possible to identify the probable position of the defect. In particular, the green area, smoother and more regular, corresponds to a transgranular fracture, while the blue area, rougher and coarser, was affected by intergranular crack development. Since the lower side is the tensile side, it is very likely to find nucleation in this area: the defect should be sought along the line indicated by the red arrows.

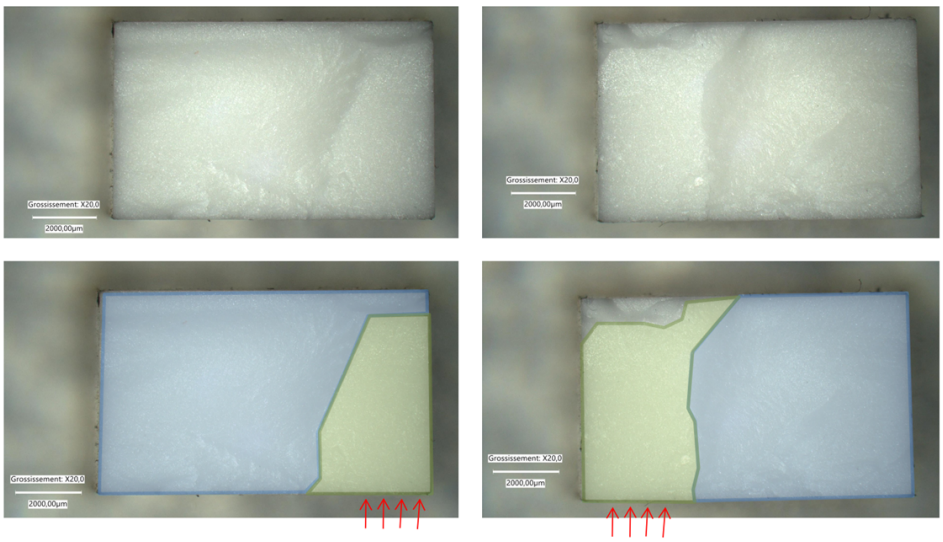

Figure 28: Fracture analysis example on specimen 4.

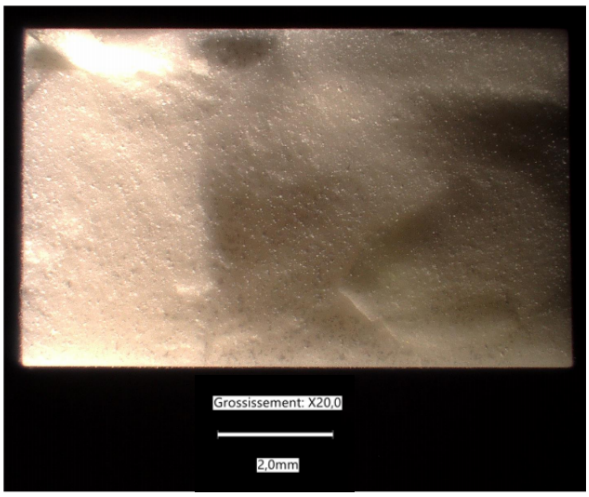

Figure 29: Side lighting helps identify the roughness of the different areas and thus trace back to the fracture mode (intralaminar or interlaminar, specimen 4).

The ceramic studied in this work, alumina, is a polycrystalline ceramic in which the fracture mode depends on the microstructure: if it has fine and uniform grains, a transgranular fracture mode will prevail, while if it has coarse grains or impurities, the fracture will tend to have a larger intergranular zone.
The grain size is largely determined by the material purity: alumina can be high purity (99.9%, fine grain, fewer impurities, tendency towards transgranular fracture), medium purity (99.5%-99.6%, coarser grain, presence of impurities and defects, greater tendency towards intergranular fracture), or low purity ($< 96\%$, coarse grain, many impurities and defects, tendency towards intergranular fracture).
For ballistic applications like the one under study, medium purity alumina ($> 99\%$) is typically used. Therefore, we expect both fracture modes to be present in different proportions depending on the specimens and nucleation points.

Penetrant liquids

In order to detect the presence of any secondary cracks next to the main fracture line, the specimens were treated with the penetrant liquid HM-430 from Sherwin (Fig. 30).

Figure 30: Penetrant liquid (left) and developer (right).

The penetrant liquid technique is part of the family of non-destructive testing methods and is particularly useful for identifying defects, porosity and cracks on the surfaces of specimens.
This method relies on the ability of the liquid to penetrate micro-cracks and surface defects in the material by capillary action: after the application of the main liquid (the penetrant itself, shown in figure 30 on the left), a developer (or "detector," shown in figure 30 on the right) is applied, which draws the fluid out of the defects, making them visible to the naked eye or under ultraviolet light.
In our case, it was necessary to use a UV lamp to visualize the defects.
The steps performed for the application were:

- Preparation and degreasing of the surface (alcohol);
- Application of the HM-430 penetrant liquid;
- The treated specimens were left to rest at room temperature (50° C) for about ten minutes;
- Cleaning off excess penetrant from the specimen surface;
- Application of the D-100 developer liquid;
- Waiting for about 10-15 minutes to allow the penetrant to rise to the surface;

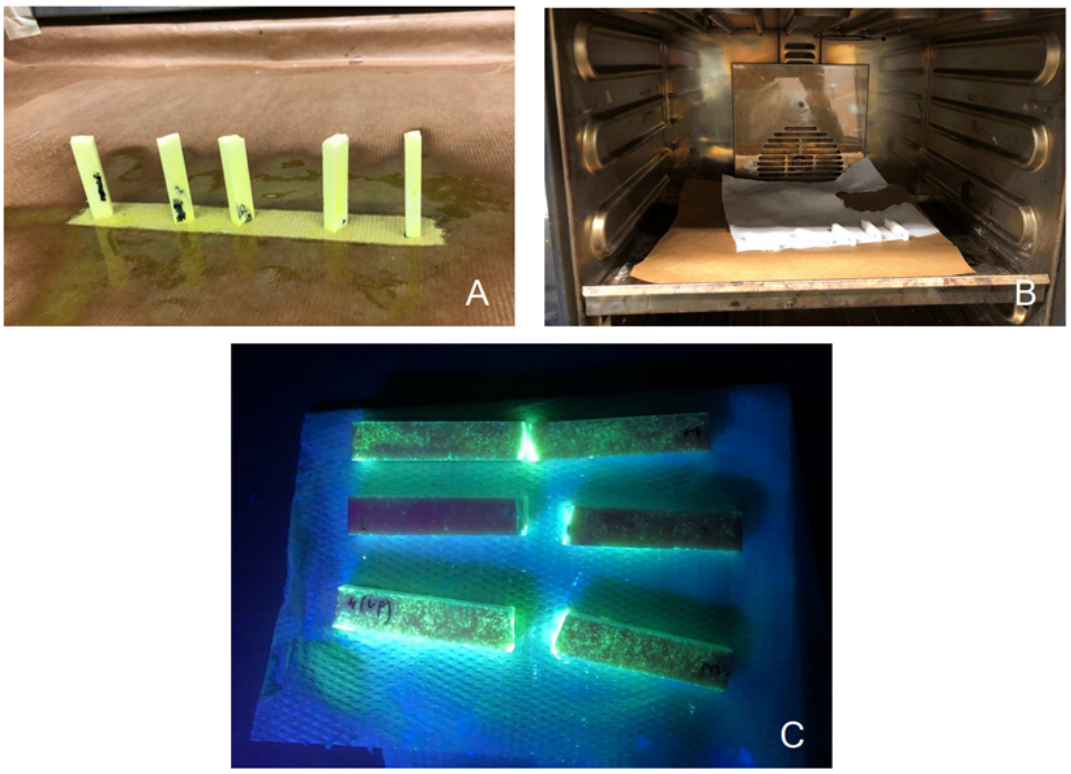

Figure 31: Penetrant liquid treatment: after applying the penetrant liquid (figure A), the samples were left to rest in an oven at a temperature of 50° for 10-15 minutes (figure B). Once the excess liquid was removed and the developer applied, the result can be visualized using a UV lamp (figure C).

After performing these steps, the specimens were examined under an optical microscope.
In some samples (tests 1, 3, and 4) secondary cracks were observed next to the main crack. No cracks were detected in the longitudinal direction entering the specimen in a direction perpendicular to the fracture surface.
A fracture was often observed in the area of the compression curling, which is consistent with the fact that in some specimens the entire upper portion in contact with the loading cylinder detached. The most interesting images are shown and commented in the following images.

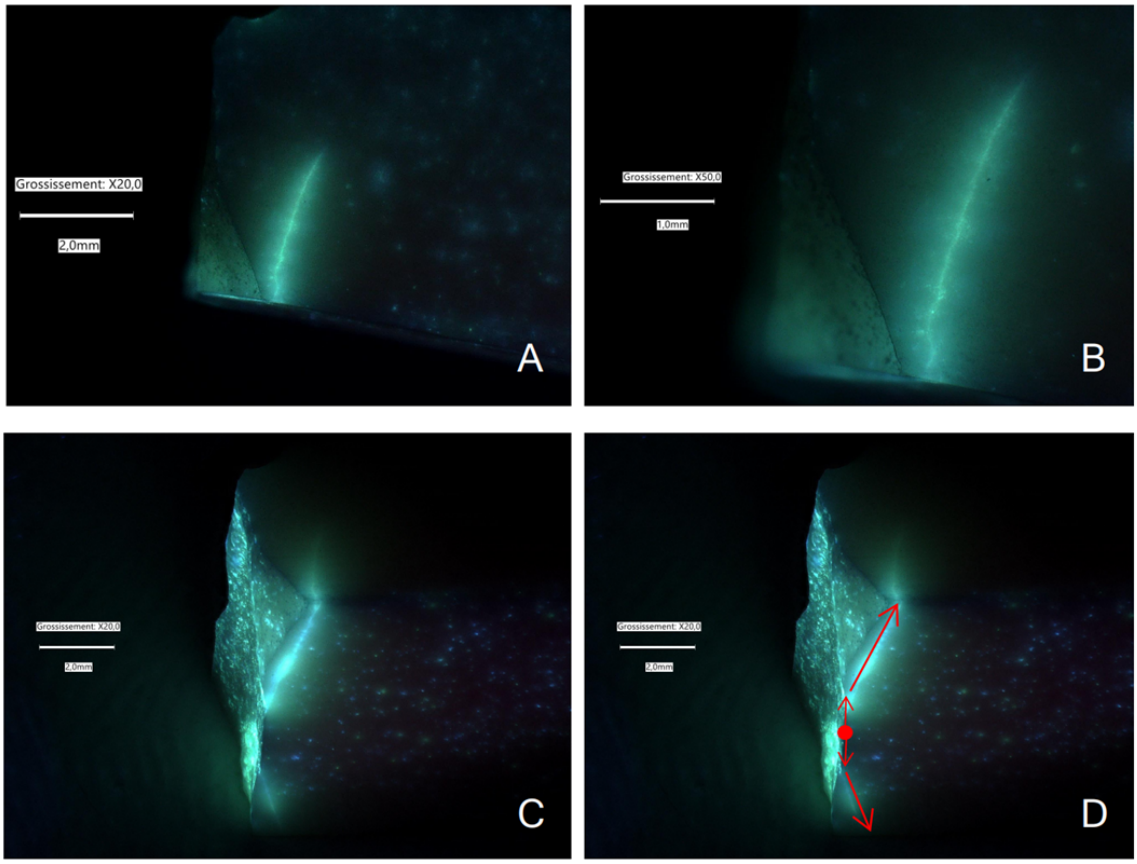

Figure 32: Specimen 1 analyzed with penetrant liquids: In figure A (20x) and B (50x), a secondary crack is visible, branching from the lower side (tensile side: the load is applied to the upper surface) next to the main fracture line. In figure C, a 3/4 view is shown: the specimen was slightly rotated to appreciate the depth of the secondary crack. From the crack path we could suppose a central nucleation point: a defect might have generated a series of fracture lines, including the central main one (figure D: the point indicates the nucleation defect while the arrows show the crack path, which splits into secondary cracks next to the main one).

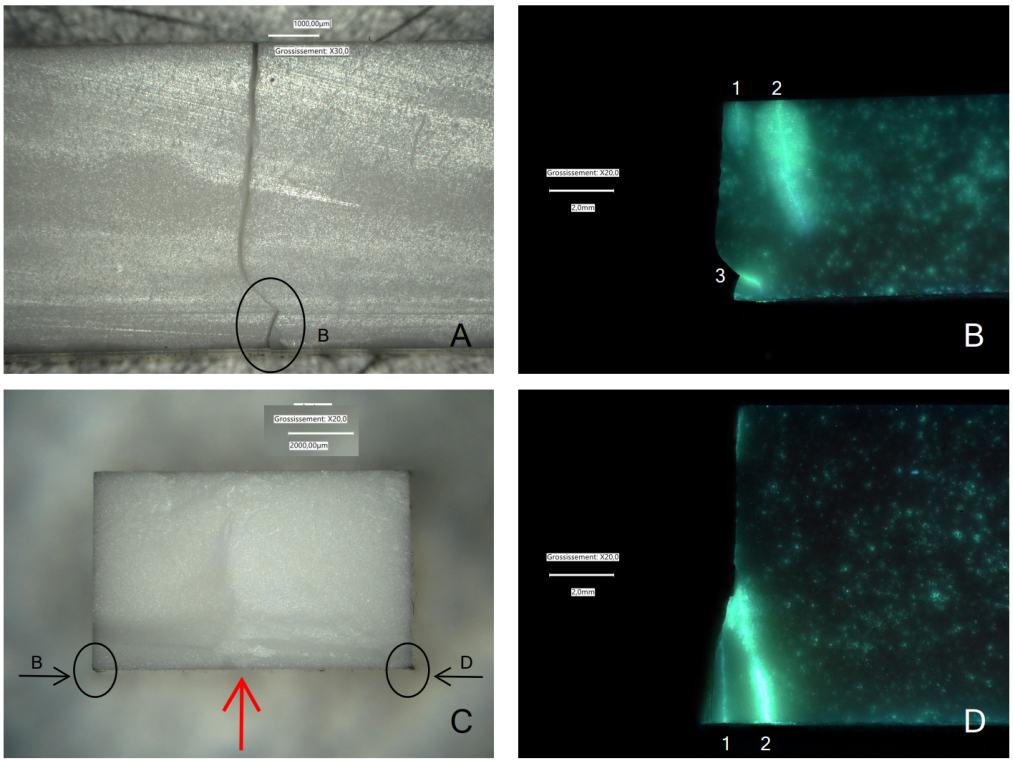

Figure 33: The images relate to specimen number three: it broke into two parts and exhibits the typical compression curling in the area immediately adjacent to the application of the load. The red arrow represents the direction of load application. In figure A, the lateral fracture pattern of the specimen is visible, with the compression curling adjacent to the load point (detail B). In figure B, the right side of the specimen is shown, observed with penetrant liquids: two secondary fractures near the main fracture surface are visible (marked "1" and "2"), and a crack is present at the compression curling ("3"). In figure C, a microscope photo of the specimen fracture face is shown, with the sides represented in photos B and D indicated. Finally, in figure D, a photo of the compression curling is shown from the opposite side of figure B: the fracture originates from the tensile side (upper side in the photo) and splits the specimen all the way to the compression zone, where near the loading pin, it branches into several cracks ("1" and "2"). Due to the local stiffening caused by the loading pin, the fracture then deviates from its main path, following one of the generated cracks and forming the compression curling.

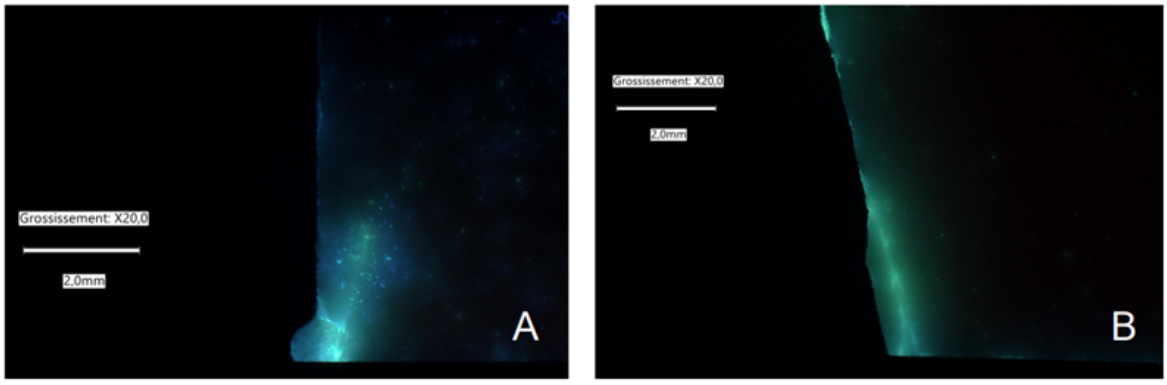

Figure 34: Two photos related to specimen number 4 are shown, previously analyzed in figure 28 and figure 29, which show the presence of secondary fractures on the compression curling (photo A), similarly to specimen number three (Fig. 33), and the presence of secondary cracks (photo B) next to the main fracture line.

3.2 FEM modeling of the test

In order to test and compare the three selected models ("Holmquist", "Nadal" and "Khan") the three-point bending test was simulated using the FEM software Abaqus. Some material properties required for the JH2 model, in fact, are not easily deducible from experimental data (or are not even experimentally obtainable) and it is therefore necessary to calibrate the numerical dataset through comparison with experimental tests.

3.2.1 FEM model settings

The support and loading cylinders were modeled using explicit shell elements "R3D4" (four-node bilinear rigid quadrilateral elements) while the ceramic was modeled using explicit solid elements "C3D8R" (eight-node linear hexahedral elements with reduced integration).
The specimen was partitioned into different sections to obtain a mesh with varying element sizes according to the needs. In particular, in the central zone, a mesh size of 0.2 mm was used, which increases in dimensions towards the ends up to a maximum size of 0.5 mm.

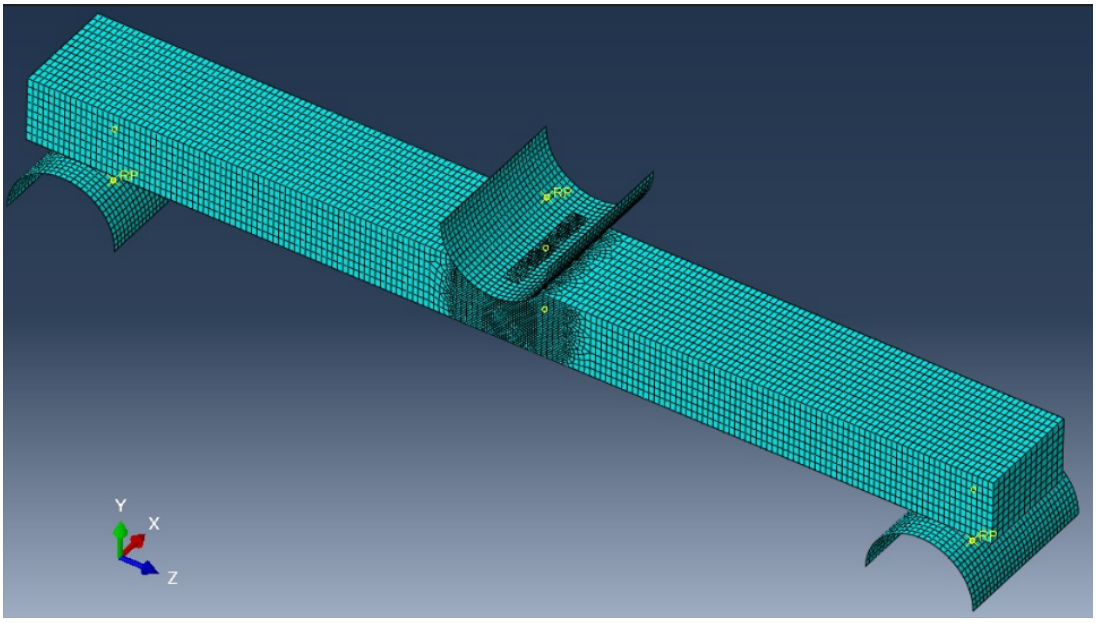

Figure 35: Mesh of the FEM model. The mesh transition was achieved by using the "sweep" option.

The loading and support cylinders also have a size of 0.5 mm and are in contact with the specimen using the "contact" command, defining a "tangential behaviour" with "penalty friction" (the friction coefficient between ceramic and steel is assumed to be 0.05) and "normal behaviour" ("hard contact"). A "smooth step" displacement was applied to the reference point of the loading cylinder in order to minimize the inertia effect of the load on the specimen (since this is an explicit simulation it is necessary to impose the shortest possible simulation time to avoid very long computation times).
The results of the simulations with the three parameter sets "Holmquist", "Nadal" and "Khan" (table 2) are presented in the following sections.

3.2.2 Numerical results: "Holmquist" parameters set

The "Holmquist" parameter set, as already seen from the tests on the single cubic mesh element presented in Section 2.2.3, defines a material with lower resistance compared to the other models. This is mainly due to the HEL value of 2.76 GPa, which is much lower then "Nadal" and especially "Khan" ones.
This parameter set performs excellently: the maximum force is correctly predicted within a 10% error, and the fracture mode is accurately represented.
The results of the analysis are shown in Figure 36 along with the experimental data from the second bending test ("Test 2"), chosen because it is considered the most representative of the experimental average.

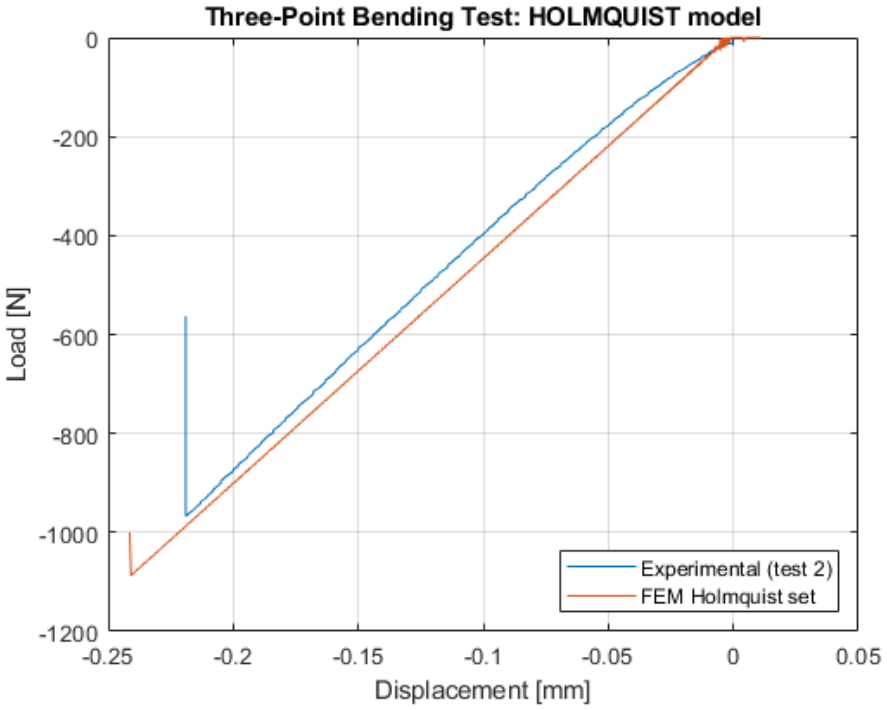

Figure 36

The fracture pattern is also extremely faithful to the laboratory test: a single central crack develops that propagates very quickly (within two hundredths of second) and affects an increasingly larger area as it approaches the loading cylinder.
In particular, as shown in Figure 37, the presence of the loading cylinder alters the stress distribution spreading the damaged area.
We can consider this behavior as something very similar to compression curling in reality: the model likely fails to accurately represent this phenomenon due to the insufficient fineness of the mesh elements near the loading cylinder.

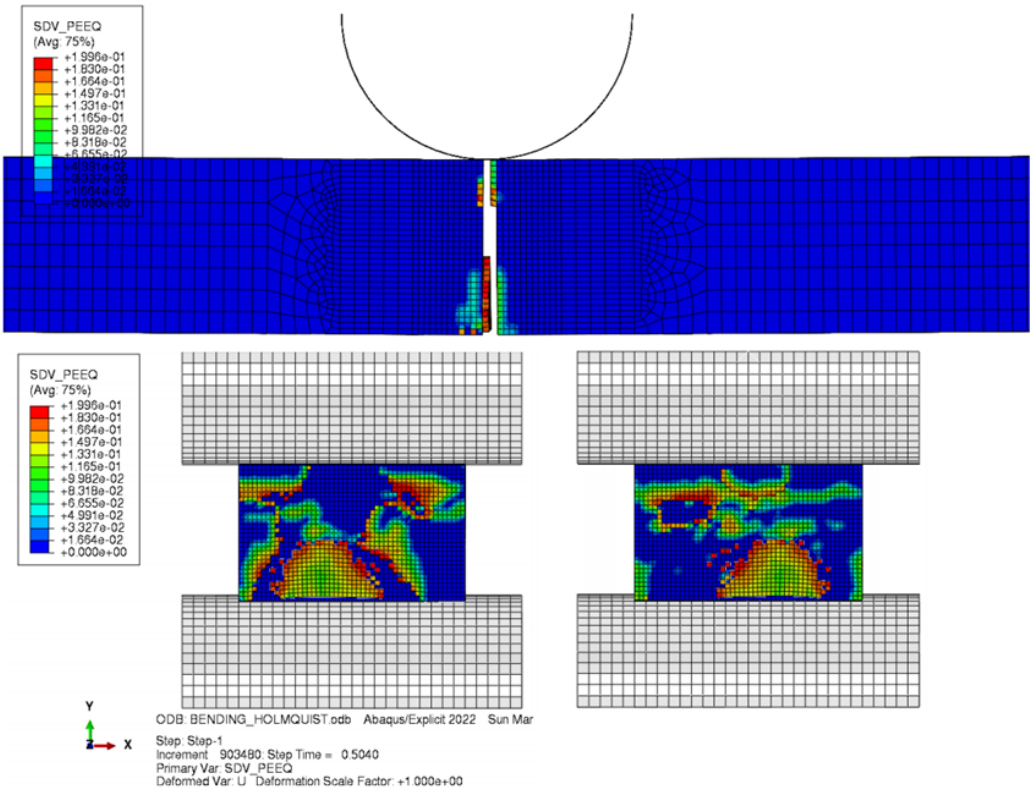

Figure 37

The different stress distribution causes the damage zone to expand. This is clearly visible when observing the variable SDV_PEEQ ("Plastic Equivalent Strain") on the fracture surface through the thickness (figure 37): this variable predicts the material damage and represents an overall measure of the intensity of plastic deformation in the mesh element.
This quantity provides a more accurate indication of the damage level: in the JH2 model, in fact, the damage variable changes from 0 to 1 following the accumulation of plastic deformation (indicated by $PEEQ$), but the transition between the two values is represented in Abaqus as discrete, and only the two values of $D = 0$ and $D = 1$ are visible in the damage plot. Therefore, we can check the damage level by referring to the accumulation of equivalent plastic strain.

3.2.3 Numerical results: ”Nadal” parameters set

The model is less accurate than the previous one: the force levels are almost twice as high as the experimental values. This is consistent with the value of HEL, which is almost double compared to the Holmquist model (here it is 6.57 compared to 2.76 GPa):

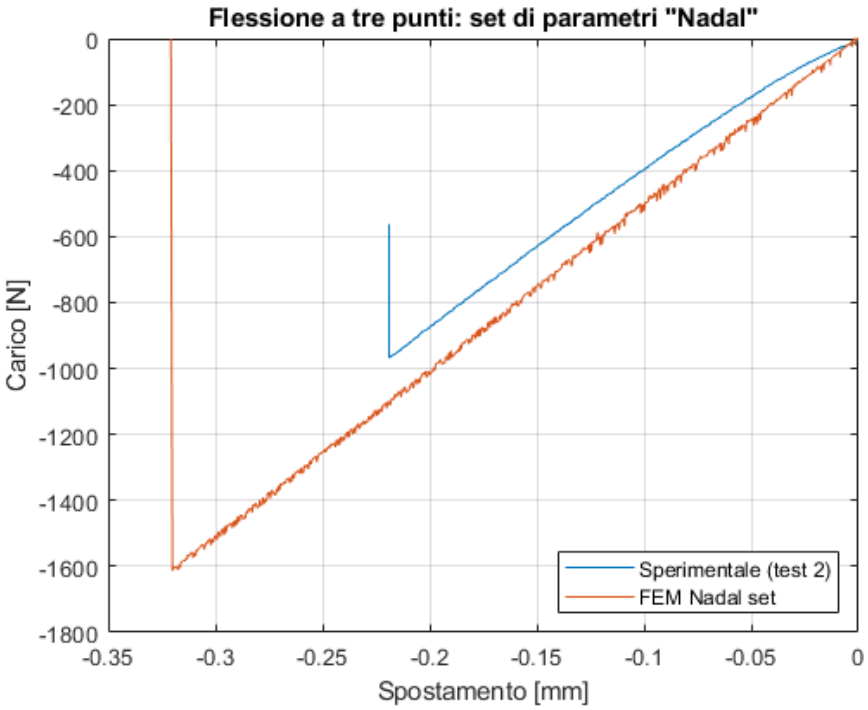

Figure 38

The fracture mode is still faithful to the experimental reality and is entirely similar to that observed with the ”Holmquist” parameter set (Figure 39).

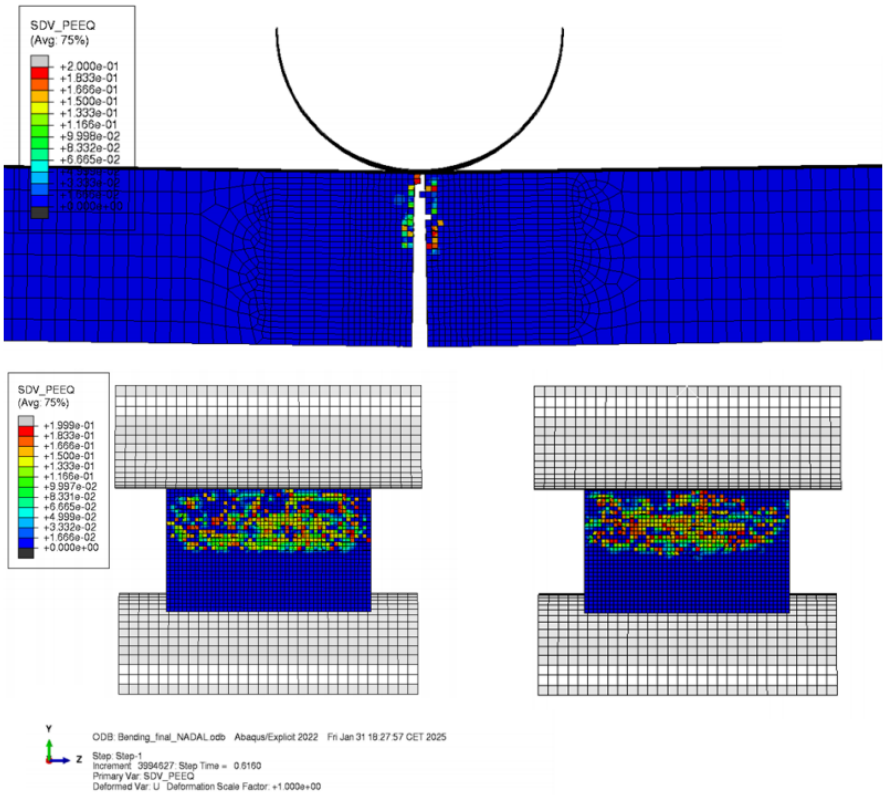

Figure 39: The fracture develops as a single line in the tensile zone and widens, damaging adjacent elements in the compression zone of the specimen. This is also due to the presence of the loading cylinder which, acting as a local stiffening, alters the stress distribution. The phenomenology is therefore similar to what happens in the real case (compression curling).

3.2.4 Numerical results: "Khan" parameters set

The third parameter set proved inadequate for representing the material behavior: the specimen does not develop any form of damage, nor do we observe significant stresses. This is certainly due to the extremely high HEL value of 19 GPa, which is far from the values of the previous sets and those found in the literature for this class of materials.
Therefore, we decided to focus on the other two parameter sets and set aside the "Khan" set.
For completeness, the force-displacement curve resulting from the analysis is still presented:

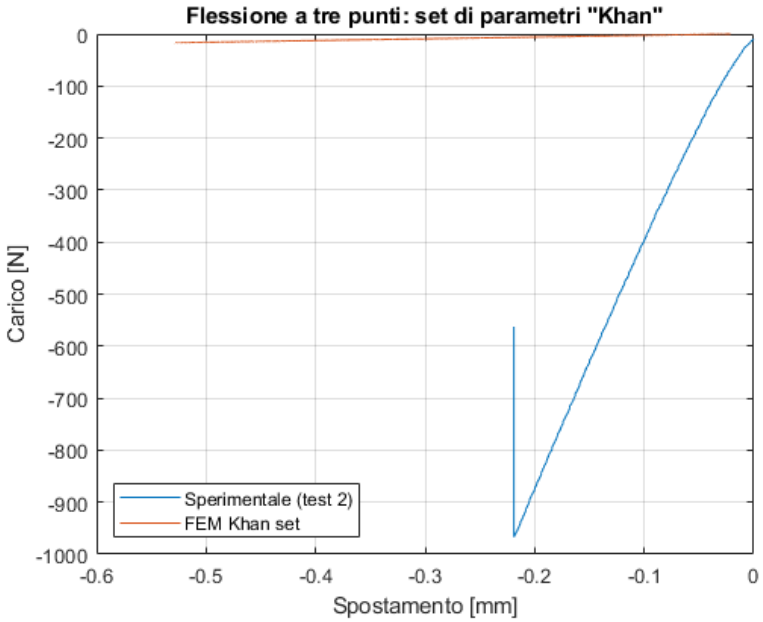

Figure 40: The model is inadequate for representing the material. It is therefore discarded: from now on, only the "Holmquist" and "Nadal" parameter sets will be considered.

3.2.5 Conclusions and observations

The parameter set that best represents the material is certainly the "Holmquist" set, while the least representative is the "Khan" set, which will be discarded in favor of the other two. The value of the Hugoniot Elastic Limit in the latter set is indeed extremely high (19 GPa) and inconsistent with the values reported in the literature for similar materials.
The comparison between the two sets, "Holmquist" and "Nadal," is shown in figure 41:

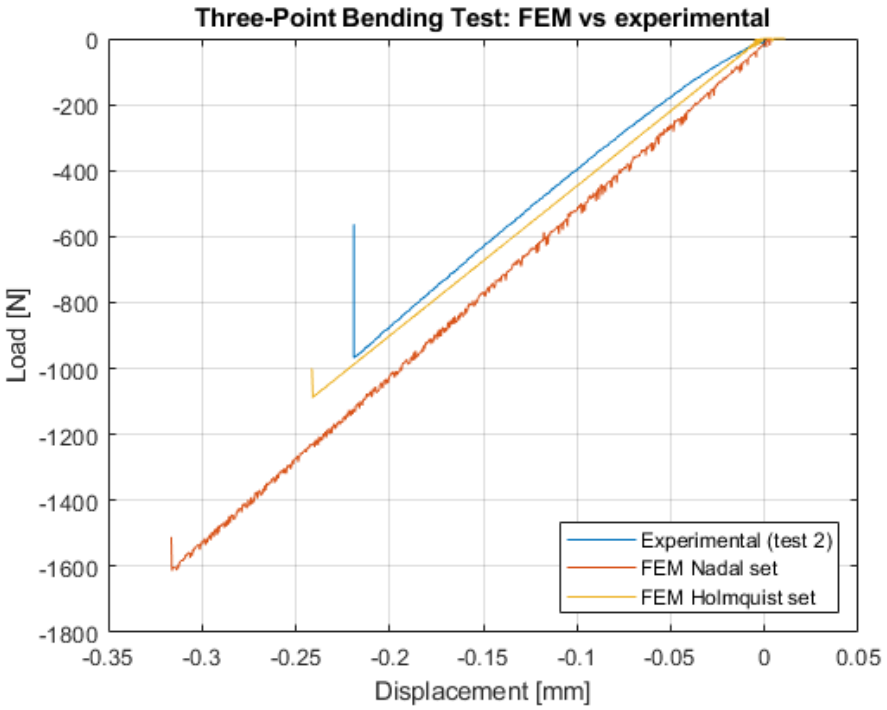

Figure 41

In view of future calibrations of the model for dynamic tests, it was considered useful to verify the effect of variations in some parameters on the "Nadal" set: it indeed differs from the "Holmquist" set mainly in the value of HEL, the parameter A in the definition of the formula for σ_i^* (see Chapter 2.1.2), and the moduli K_1, K_2 and K_3 (Table 2), but it is undoubtedly the former parameter that most impacts the behavior of the model.
In particular, the following variants were tested:

- "Nadal HEL4000": changed the Hugoniot Elastic Limit HEL value from 6.57 GPa to 4 GPa;
- "Nadal A06": changed the coefficient A from 0.88 to 0.6;
- "Nadal HEL4000 A06": version with both changes: $HEL = 4\,\text{GPa}$ and $A = 0.6$.

The results are shown in Figure 42: the lowering of the parameters A and HEL negatively impacts the material resistance, lowering the maximum fracture force peak.

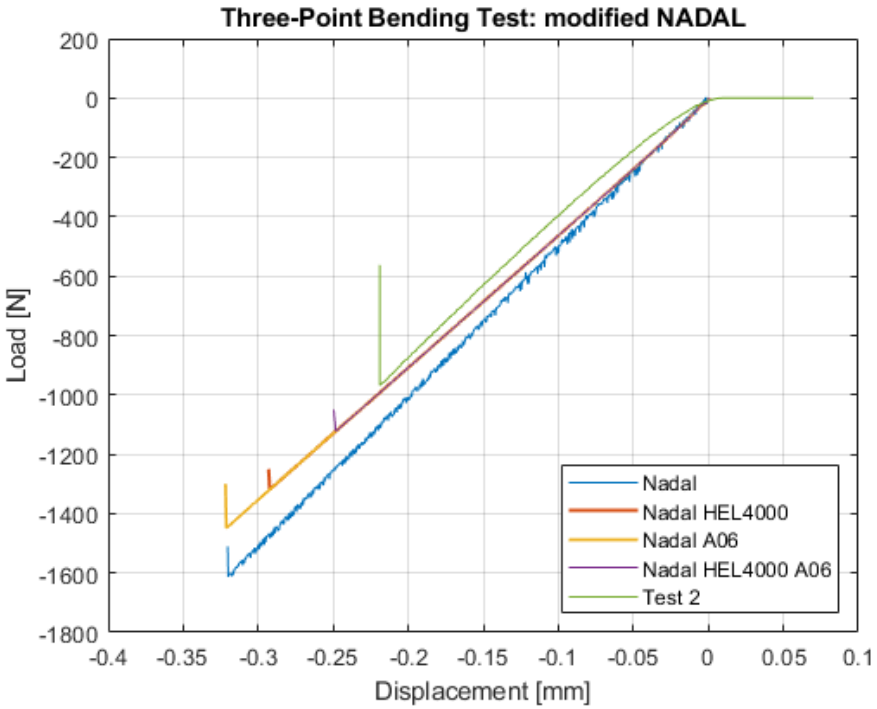

Figure 42: Effects of the variation of HEL and A on the "Nadal" parameter set. Note that the simulations on the model variants ("Nadal HEL4000", "Nadal A06", and "Nadal HEL4000 A06") were conducted with a different mesh (both in the number and shape of the elements in the fracture zone, which are slightly prismatic rather than cubic): this accounts for the difference compared to the "Nadal" simulation, which is slightly more accurate in terms of stiffness. However, a convergence analysis highlighted the small difference in peak force results between the model with a fine mesh ("Nadal") and the variants: the results are precise and more than acceptable.

It is noted that the version with both modifications reaches load levels that are absolutely comparable to those of the real test: we will therefore keep this modification in mind to potentially propose it later in the calibration of dynamic tests.
These modifications do not affect the fracture mode, which occurs in a way that is entirely faithful to reality and similar to the "Nadal" and "Holmquist" models.

4 Hopkinson Bar experimental test

The Split-Hopkinson Pressure Bar (SHPB) was originally developed by Hopkinson and further updated to its present days by Kolsky [3], and is the most common experimental method used in the study of engineering materials under high strain rate loading.
The Hopkinson-Kolsky bar testing is the standard for the determination of the dynamic stress-strain properties of materials in the case of strain rates ranging from $10^3\,\mathrm{s}^{-1}$ to $10^4\,\mathrm{s}^{-1}$.
The testing machine scheme is illustrated in figure 43.

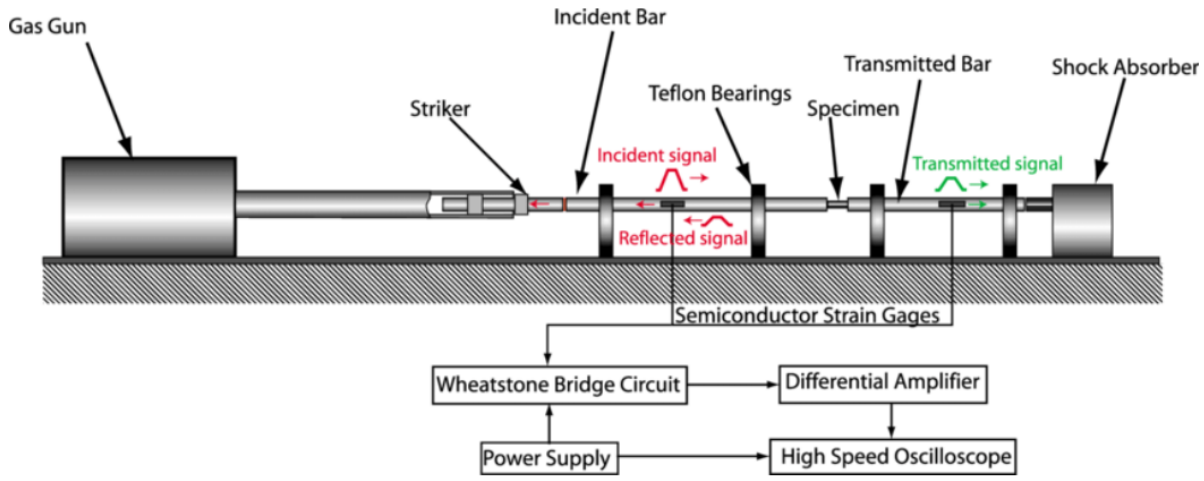

Figure 43: Hopkinson bar scheme [21]

The Hopkinson bar consists of a set of two cylindrical steel bars that are both free to move along their common axis. Along this line, a shorter bar, referred to as the striker bar, can be accelerated to a certain velocity using for instance compressed air or other gases. When the striker impacts the incident bar an incident elastic stress wave is generated in the incident bar.
The wave thus generated partly reflects onto it when it impinges upon the specimen ultimately reaching the transmitted bar. The incident stress pulse and transmitted stress pulse are measured in real time using strain gages on the incident and transmitted bars. If the two bar remain elastic and the wave dispersion is ignored, then the measured stress pulses can be assumed to be the same ones acting on the sample.
Starting from dynamic wave propagation theory it is possible to deduce the equations to be used to extract the stress-strain curve from a SHPB test. The strain rate can be calculated through the strain data of the incident bar caused by the reflected wave as it follows:

$$\dot{\varepsilon} = \frac{2\,c_0\,\varepsilon_R}{l_i} \tag{11}$$

where:

- c_0 is the one-dimensional wave speed in the bar;
- ε_R is the reflected strain signal measured in the input bar;
- l_i is the relevant gauge length of the specimen or the length used in the test setup.

The strain is calculated by direct integration of the strain rate:

$$\varepsilon(t) = \int \dot{\varepsilon}(\tau) d\tau \tag{12}$$

The stress values can be found using two different methodologies:

- Using just the transmitted wave:

$$\sigma_s(t) = \frac{A_b E \varepsilon_T(t)}{A_s} \tag{13}$$

  where:

  - A_b is the cross-sectional area of the bar;
  - E is the Young modulus of the bar material;
  - $\varepsilon_T(t)$ is the strain signal measured in the transmitted bar;
  - A_s is the cross-sectional area of the specimen.

- Averaging the force applied by the three different waves implied in this type of tests: the incident, the reflected and the transmitted wave:

$$\sigma(t) = \frac{A_b E(\varepsilon_I + \varepsilon_R + \varepsilon_T)}{2A_s} \tag{14}$$

In order to extrapolate the strain and stress data from the experimental tests, a Matlab script was implemented. The code takes as input the strain waves of the bars and calculates the strain and stress data in the specimen using the equations for strain rate (Equation 11), strain (Equation 12) and stress with the reflected wave only (Equation 13).

4.1 Experimental setup and test challenges

The Hopkinson Bar testing equipment available in the ISAE Supaero and ICA laboratories is typically used for testing composite materials and is not optimized for tests on extremely fragile and resistant ceramic materials like alumina. This has led to a series of challenges that are considered useful to report, in order to provide guidance and practical advice for replicating the tests in the future.
This study must to be considered as a "simple" introduction to the study and calibration of alumina ceramic with the Hopkinson Bar technique, and experimental settings improvements are required to obtain stress-strain data at different strain rates, as will be explained in following sections.

4.1.1 Hopkinson Bar: test challenges

A first difficulty in performing tests on extremely fragile materials such as ceramics lies in the high sensitivity required to measure the low strain values (usually in the order of 0.3-0.5% at fracture). This difficulty obviously increases as the test speed decreases and with the associated strain of the material: we can generally state that the main issue in data acquisition is the calculation of strain, given the necessary integration of strain rate, which is dependent on the often imprecise reflected wave.
In this regard, it would be advisable to measure deformation using alternative techniques, such as optical systems (laser or cameras) capable of measuring the displacement of the surfaces of the bars in contact with the specimen.
In general, to characterize a material subjected to dynamic testing and describe its behaviour at different strain rates, it is necessary for the specimen to deform uniformly (it must be in dynamic equilibrium) and at a constant strain rate.
Due to the relatively low stiffness of the bars, the conditions required to achieve these two prerequisites greatly depend on the specimen and the type of material being tested.
In a Hopkinson Bar test, the bars must remain in the elastic behavior zone, so that the deformation of the surfaces is linearly dependent on the stress waves inside the bars, and the elastic wave theory can be applied for data processing (hence the need for high-strength steel).
Moreover, the bars must be long enough to ensure the propagation of a one-dimensional wave.
These requirements are naturally all met by the machines available in the laboratory.
A problem that had to be addressed, especially in high-speed tests, was the need to insert tungsten carbide spacers between the specimen and the bars to prevent indentation.
Especially for specimens made of hard material with a diameter smaller than the bar, indentation can introduce significant errors in the measurement of strain, particularly when the strain is very low (as in our case), in addition to causing premature failure due to the amplification of stresses at the corners of the specimen.

Another source of error to monitor is related to the different impedances of the materials comprising the bars and the specimen. The mechanical impedance Z of a material is given by:

$$Z = \rho c \tag{15}$$

where:

- ρ is the material density (kg/m^3),
- c is the speed of elastic waves in the material (m/s).

This quantity represents a material resistance to the propagation of an elastic wave.
If the specimen and the bars have very different impedances, there are primarily two effects:

- Increase of the reflected wave, leading to an overestimation of the strain rate (11) and thus strain (12);
- Decrease of the transmitted wave, leading to an underestimation of the stress (13).

From this perspective, the steel-alumina coupling does not present particular issues, as these materials have very similar impedances:

$$Z_{\text{steel}} = 7850 \times 5200 = 4.082 \times 10^7 \text{ kg/(m}^2\text{s)} \tag{16}$$

$$Z_{\text{alumina}} = 3900 \times 9884 = 3.856 \times 10^7 \text{ kg/(m}^2\text{s)} \tag{17}$$

This implies a low wave reflection coefficient R, calculated as:

$$R = \frac{Z_1 - Z_2}{Z_1 + Z_2} \tag{18}$$

where:

- Z_1 is the impedance of the first material,
- Z_2 is the impedance of the second material.

For the steel-alumina interface, we thus obtain:

$$R_{\text{steel-alumina}} = \frac{4.082 \times 10^7 - 3.856 \times 10^7}{4.082 \times 10^7 + 3.856 \times 10^7} = \frac{6.155 \times 10^7}{1.387 \times 10^8} \approx 0.028 \tag{19}$$

The value of R is very small in absolute terms, indicating that the wave is almost entirely transmitted, with only a slight reflection (ca 0.028% of the wave energy).
The Hopkinson bar test aims to obtain families of stress-strain curves as a function of different strain rates: for this reason, it is necessary for the strain rate to remain constant during the test, especially for strain rate sensitive materials like alumina.
In many cases, the trapezoidal wave generated by a "classic" Hopkinson test with a cylindrical striker does not meet the requirement of constant strain rate deformation. Anyway, the transmitted wave still provides information about the specimen response and can estimate its stress.
To model the shape of the incident wave in order to achieve the correct impulse shape and generate constant strain rate deformation, a "pulse shaping technique" may be used.
The pulse shaping technique was developed to allow for the correct characterization of the dynamic behaviour of certain materials, such as rocks, which require impulses with a shape different from the trapezoidal ones generated by the impact of a cylindrical striker.
It is common, for example, to use a ramp impulse, obtained by using conical strikers ([6], [2]) or a combination of a cone and a cylinder ([6]). By varying the ratios between the areas of the cylinder and the cone, it is possible to obtain different shapes of the incident wave depending on the reaction of the tested material (figure 44).

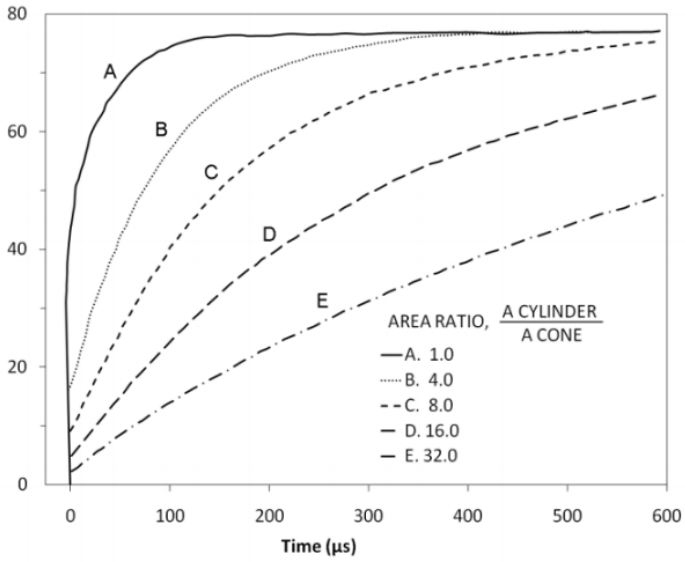

Figure 44: The incident wave can be modified by changing the ratios between the areas of the cylindrical and conical parts of the striker [6].

Another technique to modify the shape of the incident wave is to use an intermediate material between the striker and the input bar (figure 45) that acts as a "pulse shaper" minimizing wave dispersion and facilitating the achievement of dynamic equilibrium and constant strain rate deformation in the specimen.

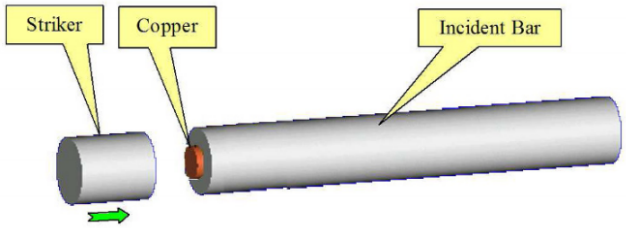

Figure 45: Pulse shaping technique with a copper "tip" material [2].

A common choice for the pulse shaping material is copper: during the initial compression phase, the shaper deformation due to its ductility generates a low initial loading rate, so that the specimen reaches a condition of dynamic equilibrium during the early phases of the wave arrival and then deforms uniformly at a constant strain rate.
In general, thanks to this technique, it is possible to achieve a wide variation in the shape of the incident wave (figure 46): the important thing is that the incident wave satisfies the requirements for constant strain rate deformation and stress equilibrium.

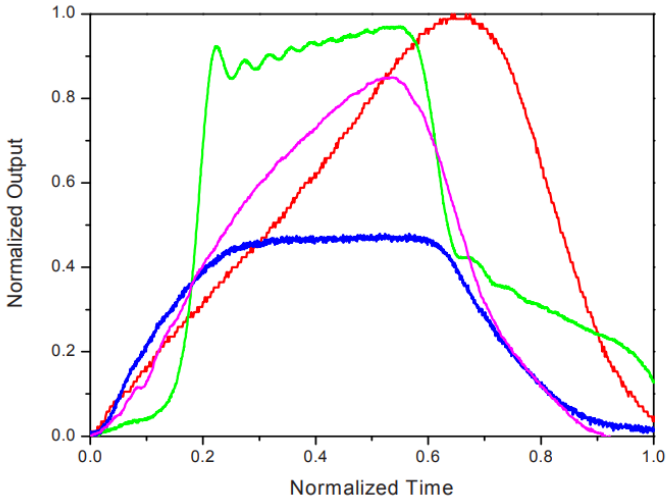

Figure 46: Different waveforms produced using the shaping technique [2]. The green wave is generated using a cylindrical striker without pulse shaping. The ideal waveform for achieving constant strain rate for the ceramic material is the red wave, which can be obtained using either a cylindrical striker or placing a tip between the striker and the input bar.

For ceramic materials like alumina, deformation occurs in an elastic-linear manner fracturing at very low strain values (around 0.3-0.5%). This low fracture strain value makes extremely difficult to measure the specimen strain through wave analysis.
Moreover, these materials do not locally yield and are therefore highly susceptible to stress concentrations, especially at the contact points with the bars.
In general, the main sources of stress concentrations are:

- Poor parallelism of the contact surfaces of the specimen with the bars. In our case, this issue was avoided using the sintering surfaces of the ceramic as contact faces (the cut was made through the thickness). On the downside, the specimen thickness is constrained to that of the original plates (6 mm);
- Misalignment of the bars, leading to poor quality of the contact surface with the specimen (in addition to disturbance waves caused by bar bending, etc.);
- Indentation of the bars due to the high resistance and stiffness of the tested material. This causes an increase in localized stress at the edges of the specimen, leading to premature failure (figure 48). To solve this issue and avoid damaging the steel bars, it is necessary to use tungsten carbide spacers between the bars and the specimen.

Figure 47: Tungsten carbide spacers used in high velocity Hopkinson bar tests.

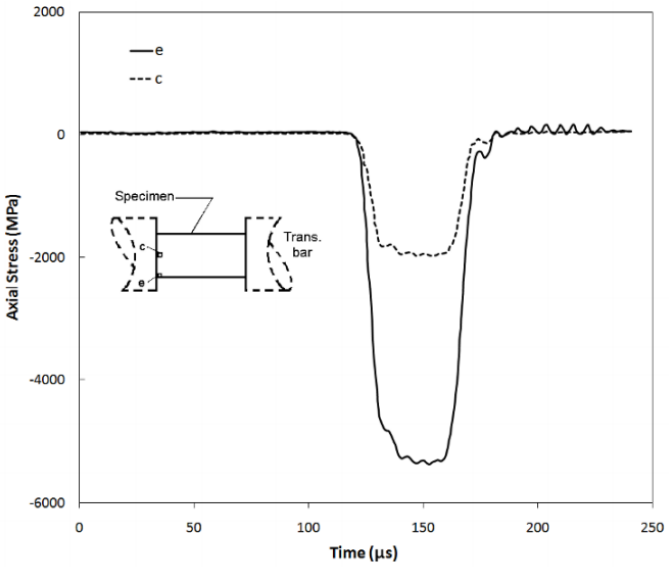

Figure 48: Due to bars indentation, stress concentration occurs at specimen contact surface corners ([2]). These localized stresses decrease if we use spacers made of an harder and more rigid material than steel, such as tungsten carbide.

In our case, the use of tungsten carbide spacers at the specimen sides significantly reduces the risk of indentation and, therefore, the stress concentration on the ceramic. At the same time, the choice of this material does not introduce wave reflection issues at the interface with the bars, as it has a mechanical impedance very similar to that of steel.
Due to the elastic linear response of alumina, it is necessary to generate a "ramp" incident impulse to deform the material at a constant strain rate and ensure the dynamic equilibrium of the specimen. This can be achieved through the pulse shaping technique.

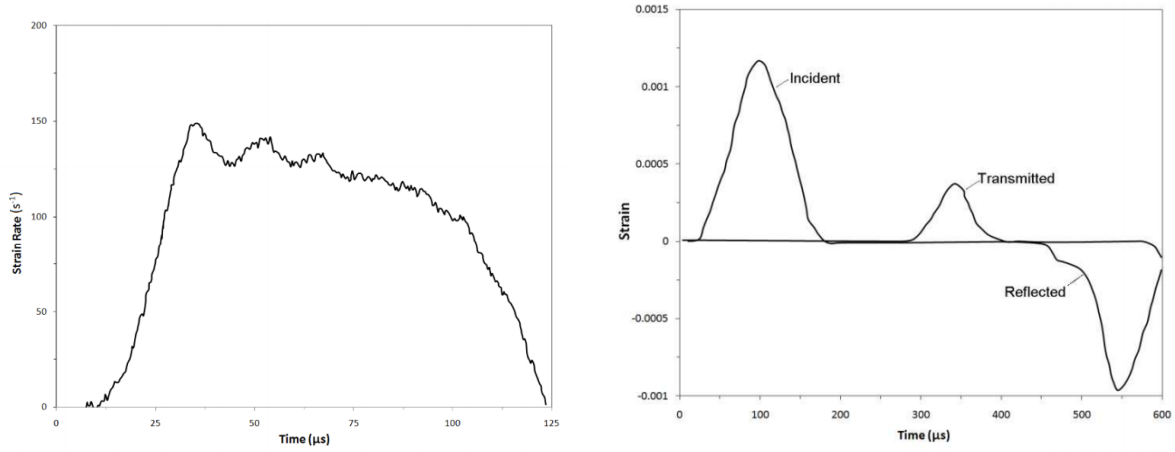

(a) (b)

Figure 49: Constant strain rate and resulting strain achieved through a ramp impulse (like the red curve in figure 45) on Macor ceramic [2].

The tests conducted in the ISAE laboratory are part of an initial series of introductory tests and were performed on a Hopkinson Bar without pulse shaping: this implies that the strain rate obtained has not been constant, and therefore, it has not been possible to characterize the material and obtain its stress-strain curves at different strain rate values.
However, the results are still considered useful as they highlight the issues and challenges of the test and remain valid for comparison with numerical models, the ultimate goal of this work.

4.2 Experimental data aquisition

During the Hopkinson Bar tests conducted in the ISAE Supaero and ICA laboratories, 42 prismatic specimens with a square base of 10x10 mm and a height of 6 mm (figure 50) were tested, cut from 90x90x6 mm alumina plates using a diamond blade.
This method allowed for minimizing chipping and defects on the sides of the specimen, which would have increased test dispersion and potentially invalidated the results. After cutting a sufficient number of specimens, those with visible macro defects were excluded from the test. It should be noted that the other available alternative for cutting was the waterjet technique, but this method proved ineffective due to "tapering" (conical cutting caused by the divergence of the jet: the water loses energy along the thickness widening the cutting jet). This phenomenon produces cutting surfaces that are not perfectly planar but rather inclined, which is unacceptable for this test, that requires flat contact surfaces between the specimen and the bars.

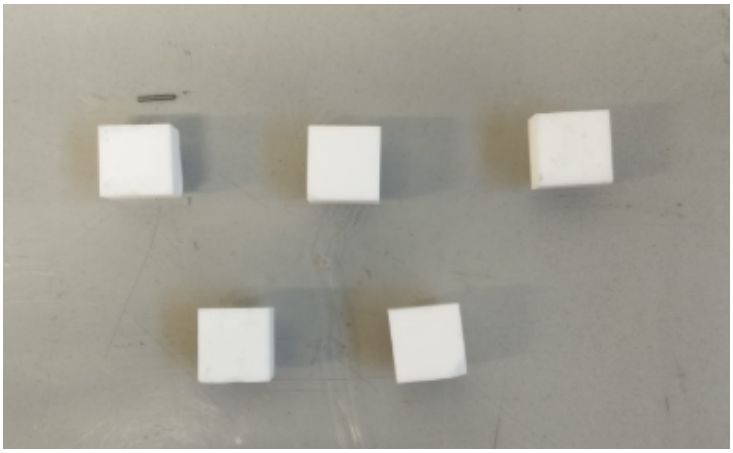

Figure 50: Some alumina specimens for the Hopkinson bar test.

Two experimental campaigns were conducted for the Hopkinson Bar test: the first at low velocity (from 4 to 6 m/s) and the second at higher velocity (from 15 to 26 m/s). Depending on the test velocity, two different machines were used: in the first case, the striker is set in motion by a spring, while in the higher velocity case it is driven by a pressurized tank.
The machines were designed by the ISAE Supaero laboratory and are schematized in figure 43 (in the case of the low-velocity machine, the pneumatic system was replaced by a "leaf spring," as shown in figure 51).

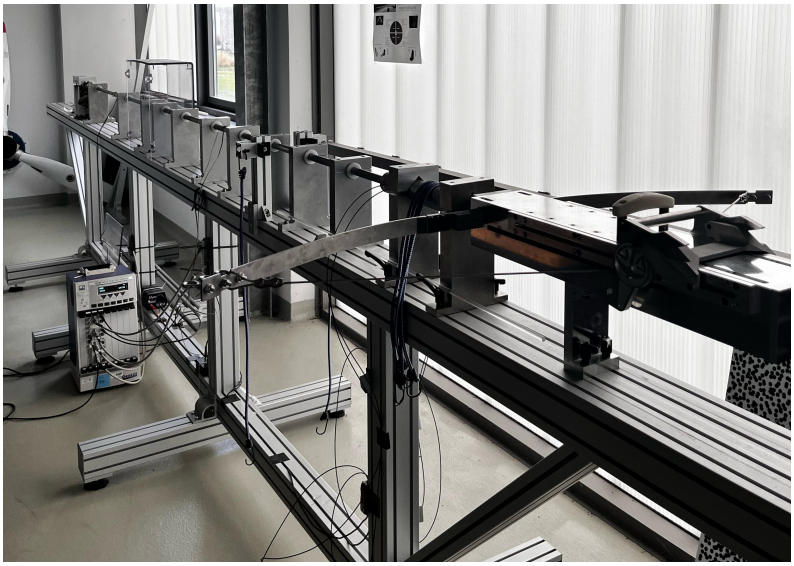

Figure 51: Low velocity Hopkinson bar.

The specimen is mounted between the incident and the transmitted bar, in contact with tungsten spacers to prevent indentation.
Bars and spacers are fixed together by the use of adhesive tape (figure 52).
The specimen is held in position by a thin layer of grease, which "glues" it to the bars and helps making the input pressure wave clean and uniform (this prevents the presence of air gaps and imperfections in the contact between the bar and the specimen).

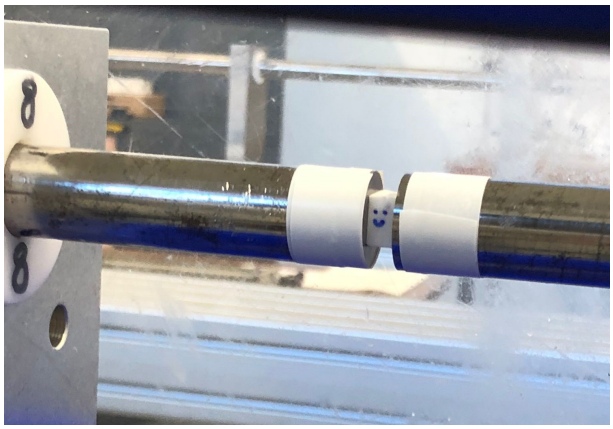

Figure 52: Mounting of the specimen on the Hopkinson Bar testing machine.

The experimental setup also includes a high-speed camera and led lights (figure 53): this made possible to capture images of the specimens fragmentation process. These photos will be very important in the evaluation of the numerical cracking patterns.

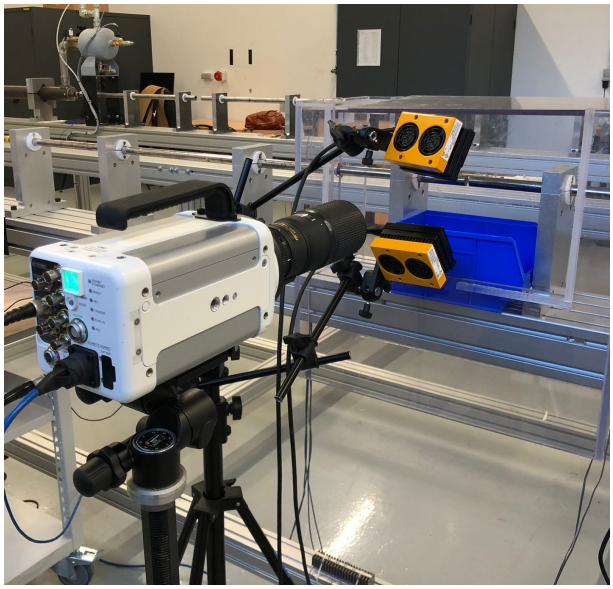

Figure 53: High-speed camera and LED lights for illumination.

The striker velocity is adjusted by adding springs in the low-velocity setup and through a pressure regulation system for the high-velocity setup (the relationship between pressure and striker velocity is shown in figure 54).

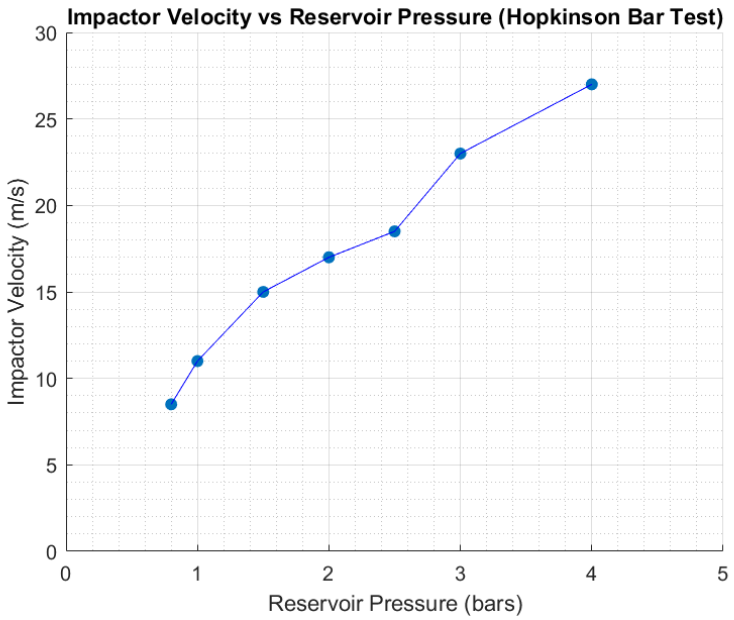

Figure 54: Tank pressure and striker velocity relation.

The specimens were tested with the following striker velocities:

- Low-velocity setup:
  - 4.2 m/s (2 tests);
  - 5 m/s (3 tests, velocity achieved by adding one spring);
  - 6 m/s (3 tests, velocity achieved by adding two springs);
- High-velocity setup:
  - 15 m/s at 1.5 bar (3 tests);
  - 18.5 m/s at 2 bar (3 tests);
  - 18.5 m/s at 2.5 bar (1 test);
  - 23 m/s at 3 bar (2 tests);
  - 26 m/s at 3.5 bar (2 tests);

These velocities will be used to set the boundary conditions for the FEM simulations in Abaqus.

4.3 Low velocity tests

During the test, the time-deformation history of the strain gauges located on the input and output bars is recorded as output data, corresponding to the incident and reflected and transmitted waves respectively. From these curves it is possible to derive the stress-strain specimen graph by applying the equations presented earlier in the chapter.
A Matlab script was implemented to calculate the stress-strain plots from the incident, reflected and transmitted wave curves at different strain rates in order to assess the performance of the numerical models.
Figure 55 shows an example of experimental curves in the bars at low velocity: similar behavior is observed for all test velocities.

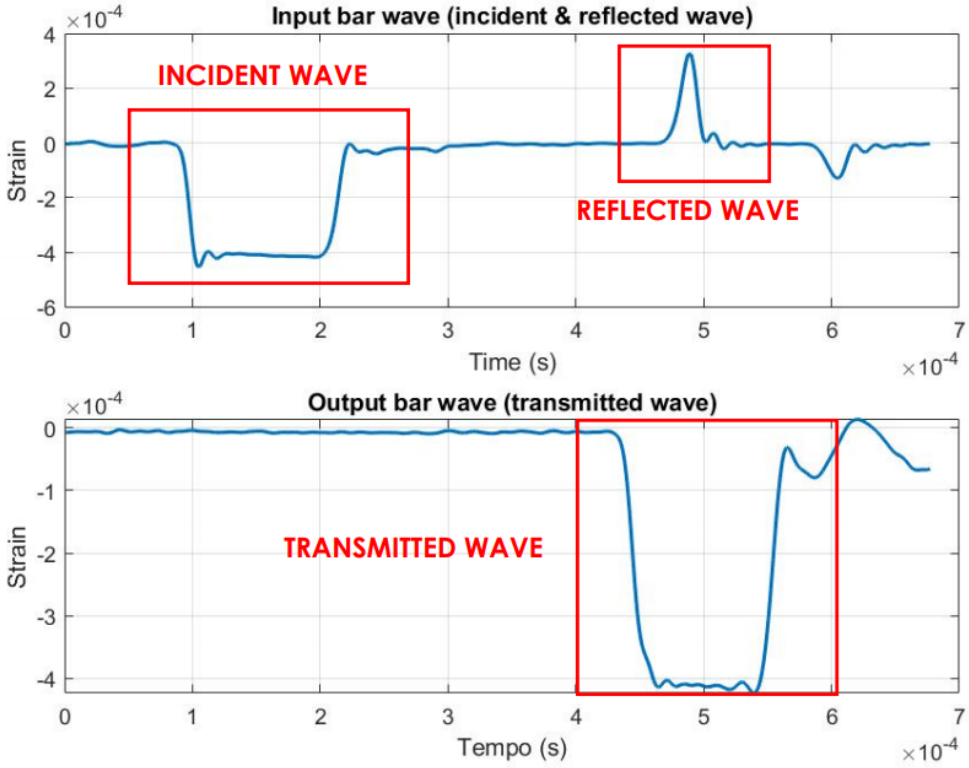

Figure 55: Example of incident, reflected, and transmitted waves in a low-velocity Hopkinson Bar test (4.21 m/s).

The plots related to the specimens tested at low velocities (4.2, 5 and 6 m/s) are shown below for each test (left figures) and averaged (right figures). In all the graphs, data that deviated too much from the average were removed (for examples with 5_3 and 6_1 tests). The average strain rate peaks obtained during the tests (elastic phase) are highlighted in figure 58.

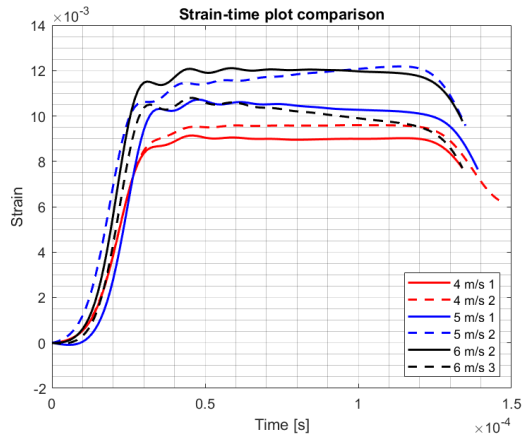

(a)

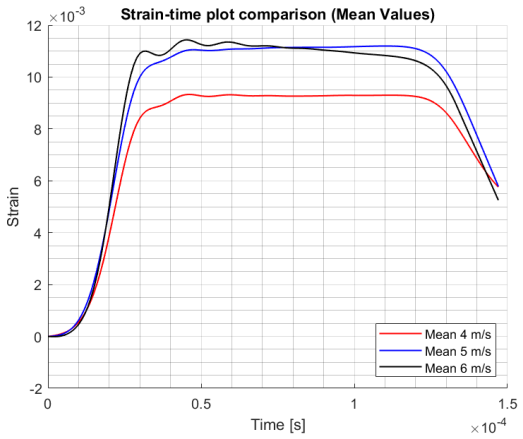

(b)

Figure 56

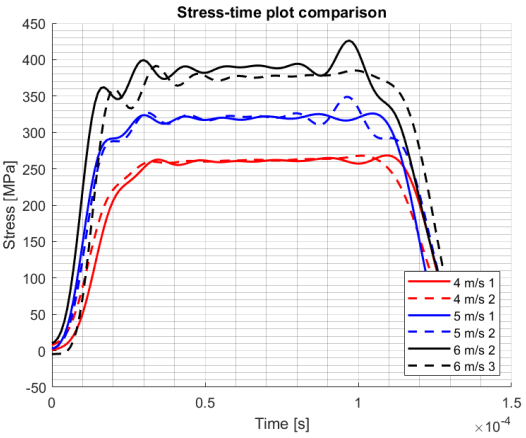

(a)

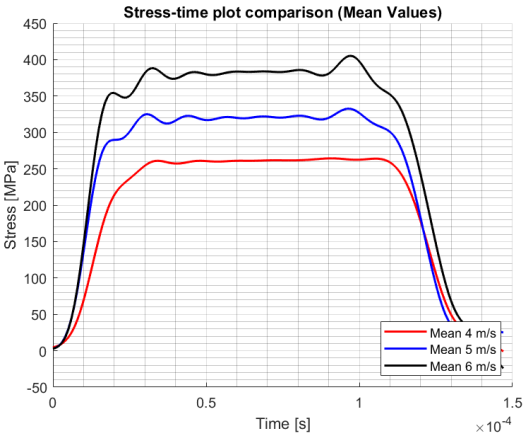

(b)

Figure 57

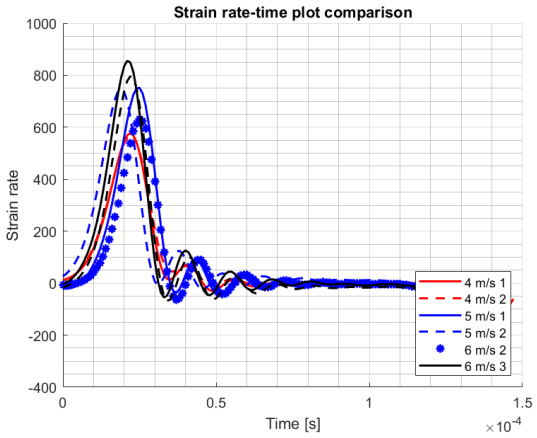

(a)

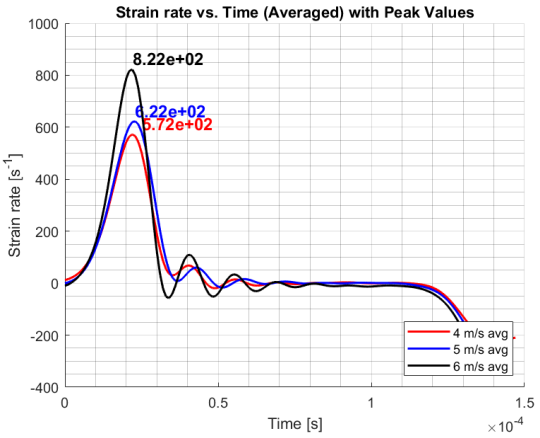

(b)

Figure 58

It is believed that the initial oscillations in the early phase of the tests are due to the arrival of the wave at the interface between the bar and the specimen. While these oscillatory phenomena are of secondary importance in understanding the graphs (they reduce to oscillations only in the rising phase of the curves) they significantly affect the stress-strain plots.
Since no specimen fracture was observed during the first compression wave in these low-velocity tests, a linear graph would be expected. The material undergoes only elastic deformation, and thus the stress-strain plot should theoretically be a straight line, apart from minor hysteresis effects that are always present. An example of the theoretical behavior is shown in figure 59.

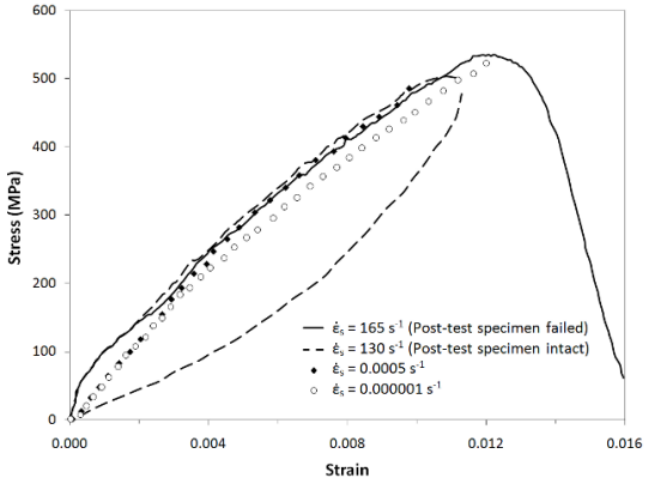

Figure 59: Stress-strain plot for "Macor" ceramic from Hopkinson Bar tests [2]: whereas in the case of failure the stress decreases as the strain increases (solid line), when no fracture occurs the stress returns to zero exhibiting hysteresis behavior (dashed line). Since no fractures were observed in low velocity tests, this kind of behaviour is expected.

After appropriate filtering, the resulting stress-strain plot is as follows:

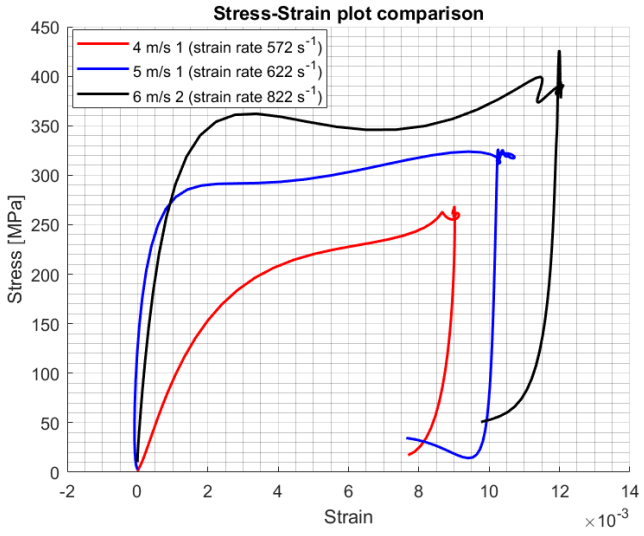

Figure 60

As expected, the stress increases with the striker velocity; however, it was not possible to identify strain-rate effects on the material strength, since the specimens did not reach fracture stress during the tests.
For this reason, another series of tests at higher velocity was carried out.

4.4 High velocity tests

The tests were performed using a pneumatic Hopkinson Bar, which allows reaching striker velocities significantly higher than those of the previous tests.
Thanks to the use of the high-speed camera, it was possible to observe the fracture mechanisms in the specimen during the test and verify its behavior. The fracture mechanisms and their evolution were then compared with the stress-strain curves obtained from the input and output bar measurements. Experimental results are reported below in terms of stress-strain curves, along with the deformation waves recorded by strain gauges on the input and output bars.

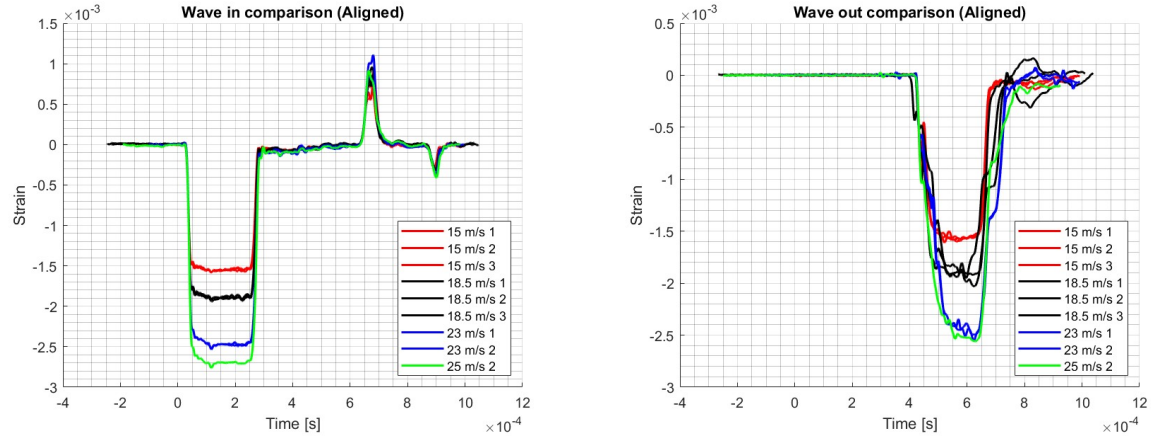

(a) (b)

Figure 61

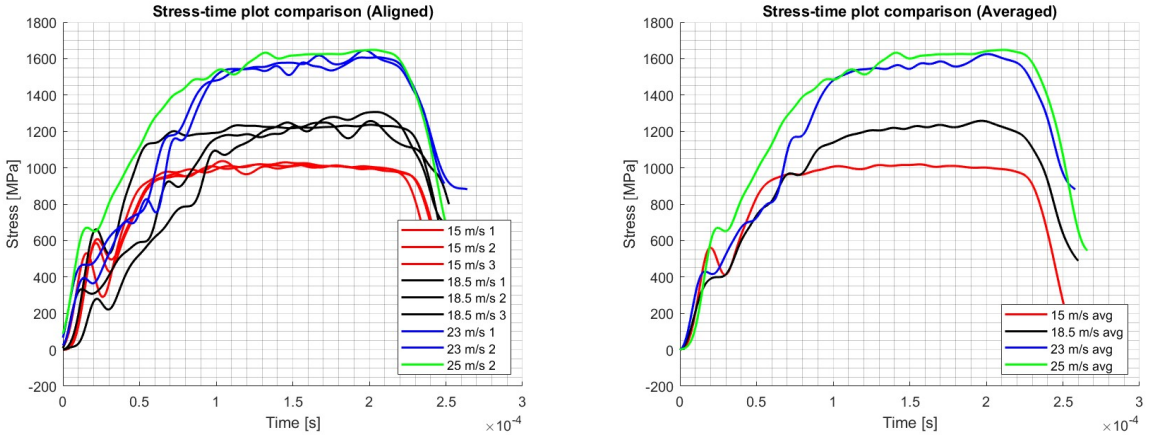

(a) (b)

Figure 62

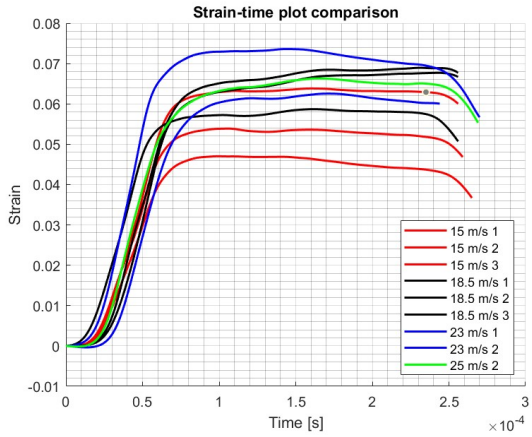

(a)

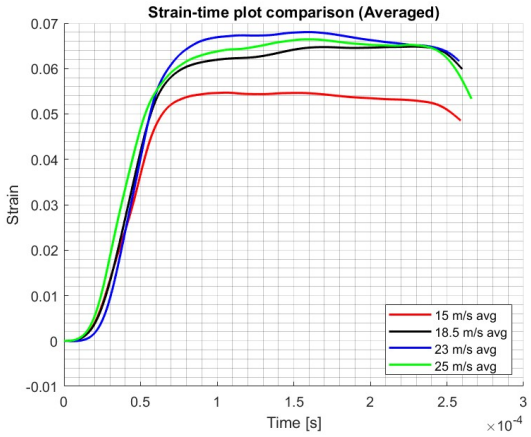

(b)

Figure 63

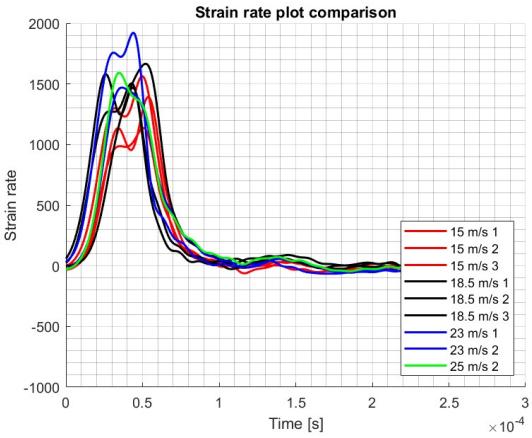

(a)

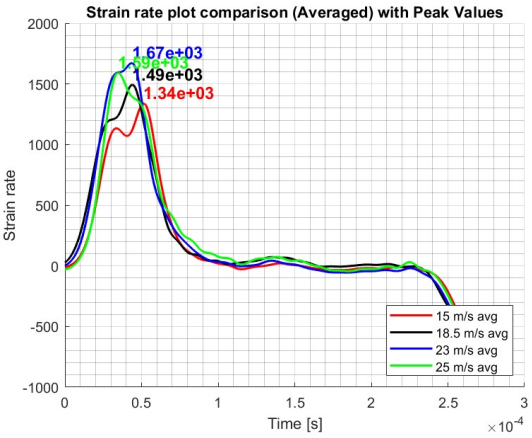

(b)

Figure 64

Figure 65

For completeness, a final comparison between the two low and high velocity test campaigns is reported:

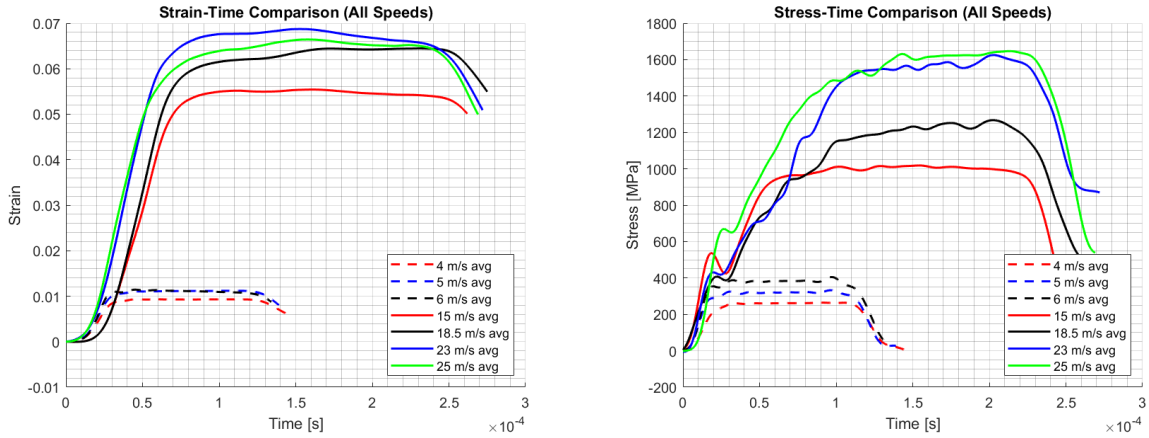

(a) (b)

Figure 66

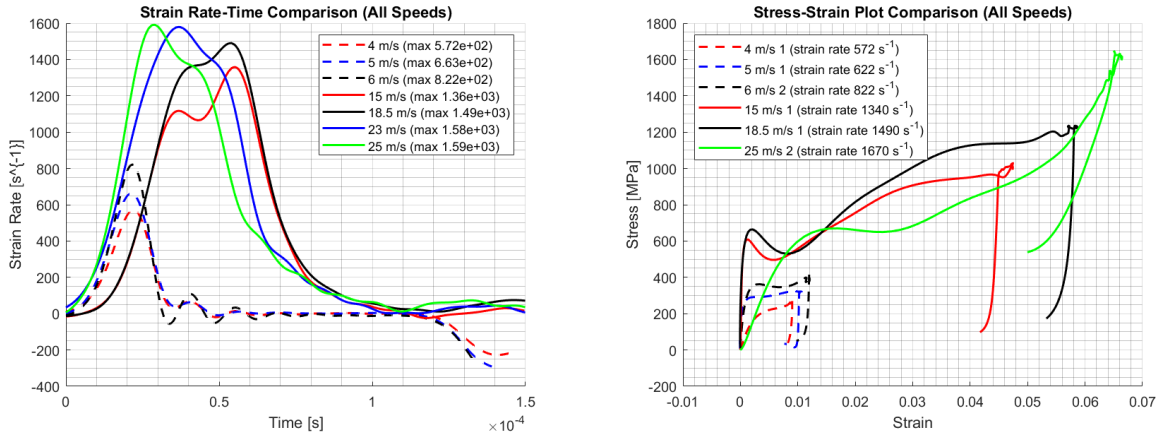

(a) (b)

Figure 67

The observed differences show that the curves obtained from low-velocity tests are significantly smoother compared to those from high-velocity tests.
This difference is primarily due to the use of tungsten carbide spacers (required in high-velocity tests to prevent bar indentation) and the application of grease as an intermediate layer between bars and spacers. The grease ensures that the signal is transmitted as uniformly as possible, compensating for potential surface non-parallelism, but introduces a disturb in the wave generated in the high velocity tests.
To further investigate these effects, three different configurations were tested at low velocity (5 m/s):

- Configuration without interfaces between bars and specimen: the ceramic is directly in contact with the steel bars;
- Configuration with tungsten carbide spacers but without grease on the contact surfaces with the bars;
- Configuration with tungsten carbide spacers and grease at the contact surfaces with the bars.

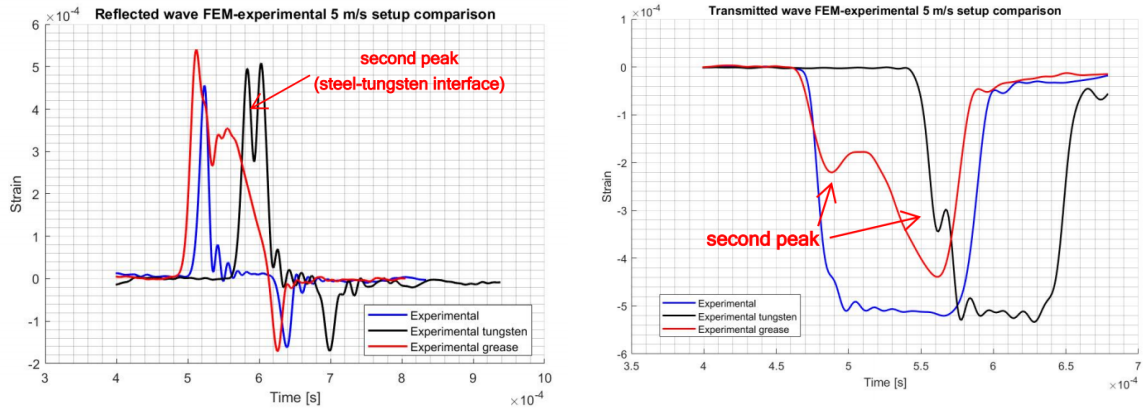

(a) (b)

Figure 68

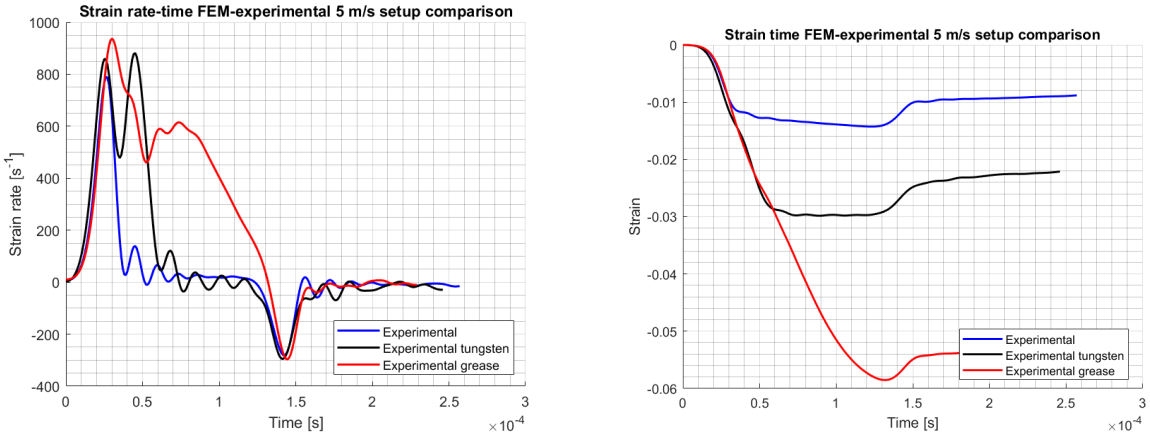

(a) (b)

Figure 69

The observed effects on the reflected wave are significant and can be attributed to the following factors:

- Presence of interfaces between the bars and tungsten carbide spacers: the incident wave is partially reflected at the interface before reaching the ceramic, causing a second peak in the reflected wave, as visible in figure 68a. This peak is responsible for the oscillations during the rising phase of the stress-strain curve obtained from the high-velocity tests, where spacers are necessary;
- Compression of the thin grease layer between the bars and spacers: the incident wave compresses the grease, causing it to escape laterally from the adhesive tape at high velocities (figure 70). This leads to a relatively large displacement compared to the very low deformation of the ceramic. This phenomenon significantly contributes to the overestimation of strain measured during the tests.

These observed effects are responsible for the extremely high strain values measured during the high-velocity tests (figure 63a): indeed, such values are entirely incompatible with the fracture strain of alumina, which ranges between 0.05 and 0.3%. A similar effect is also present in the low-velocity tests although significantly reduced by the absence of grease at the interface (indentation was not a risk at lower velocities).

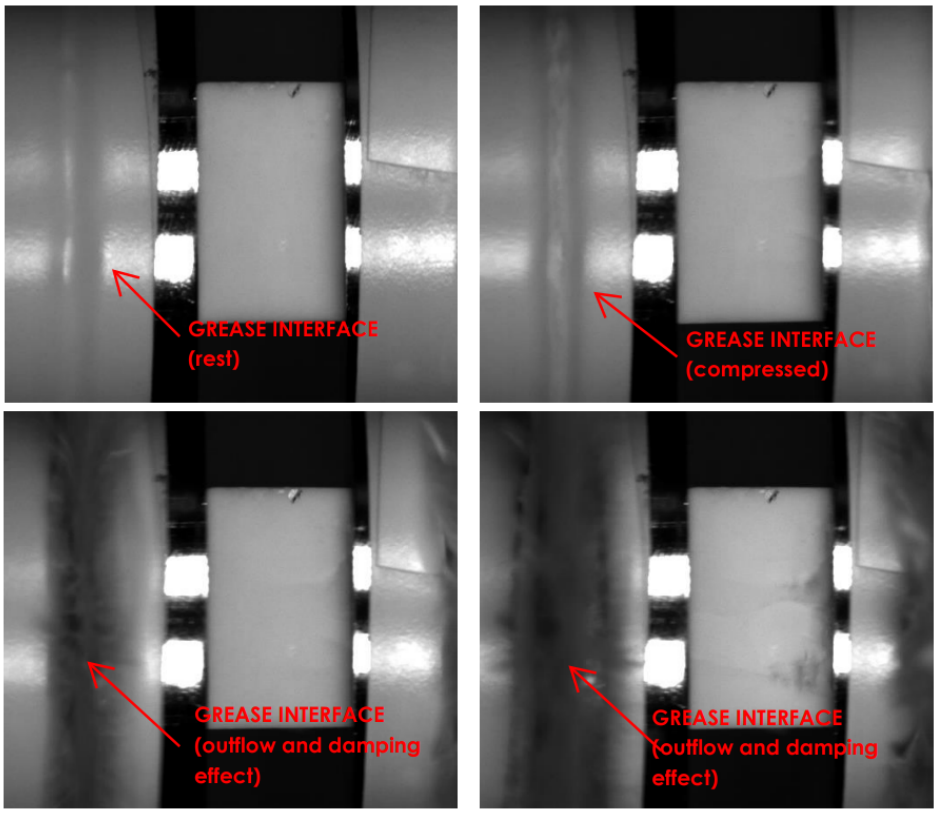

Figure 70

To obtain a more accurate strain estimation only the linear rising and falling portions of the curve have been analyzed, and the strain has been corrected accordingly, ignoring the region characterized by a drop and subsequent linear increase of the strain, as shown in figure 71.

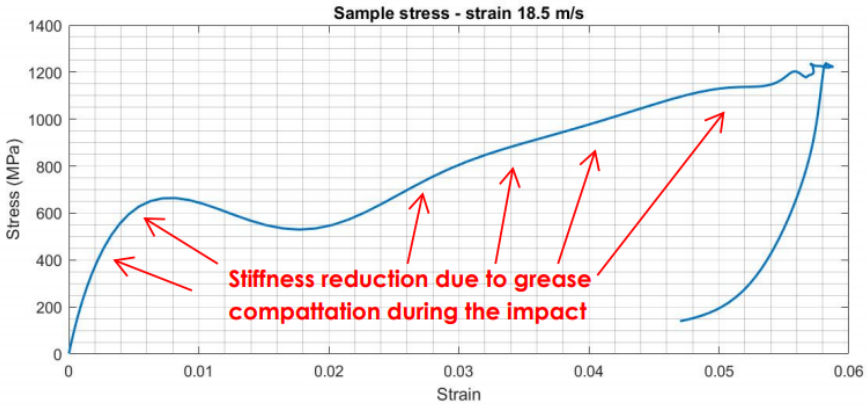

Figure 71

4.5 Specimen fracture analysis and post processing of the data

4.5.1 Fracture analysis

The use of a high-speed camera during the high-velocity tests allowed for the verification of specimen fracture. During each test conducted, whether at low or high velocity, specimen fragmentation was observed, but it is important to identify when it occurs: in all cases, catastrophic fracture occurs during the return phase of the compressive wave and not following the first arrival (which is the one of interest, that we analyze using Matlab code and from which we derive the strain and stress estimations).
The following table reports the results of the specimen observations during the high-velocity tests along with the corresponding reference stress reached during the test:

Test	**Fracture observed**	**Type of fracture**	**Stress [MPa]**
15 m/s (1,5 bar) 1	No	–	–
15 m/s (1,5 bar) 2	Yes	Lateral fracture due to local defect	ca 1000
15 m/s (1,5 bar) 3	No	–	–
18,5 m/s (2 bar) 1	No	–	–
18,5 m/s (2 bar) 2	No	–	–
18,5 m/s (2 bar) 3	No	–	–
21 m/s (2,5 bar) 1	No	–	–
23 m/s (3 bar) 1	Yes	At least 4 macrofractures	ca 1600
23 m/s (3 bar) 2	Yes	At least 4 macrofractures	ca 1600
26 m/s (3.5 bar) 1	Yes	Initial macrofractures followed by fine lateral fragmentation (test to be discarded due to bar misalignment)	ca 1650
26 m/s (3.5 bar) 2	Yes	At least 2 macrofractures	ca 1650

Table 4: High-speed Hopkinson bar tests: only specimens from tests at 23 and 25 m/s exhibited visible fractures to the naked eye during testing.

In all observed cases, the macroscopic fractures originate from the specimen second side and immediately extend to the contact surface with the first bar. The images indicate that cracks begin to form during the specimen loading phase: the fractures occur at the moment when the wave reaches the exit surface, approximately after 0.02 milliseconds. It is noted that this happens shortly after the valley of the stress-strain curve due to the first interface between tungsten and steel. The fracture might be caused by the sudden compaction of the ceramic against the bar, triggering an impact phenomenon and crack initiation, rather than by the wave exceeding the material inherent strength.

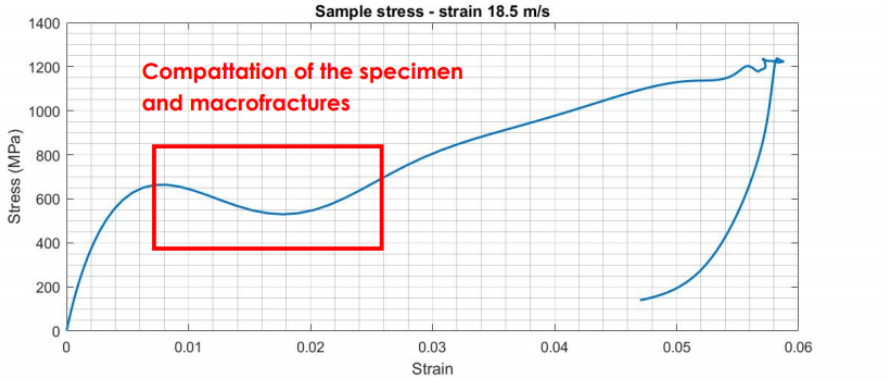

Figure 72

It is important to note that oscillatory phenomena like the one shown in figure 72 could also be due to wave oscillations caused by bar bending, or by the simple superposition of small valleys and peaks in the curves, later amplified by the Matlab script.
In light of these considerations and those presented in the previous paragraph (figure 71), only the linear unloading portion was used for the comparison with the numerical model: in this region, there are neither phenomena of grease compaction at the interface nor other disturbances (bar bending, wave reverberation phenomena) that could cause oscillations like those observed during the loading phase. Figure 73 shows the case of the 23 m/s test (pressure 3 bar), where the specimen fracture is clearly visible, along with the previously illustrated phenomena of stiffness reduction due to the presence of grease at the interface.

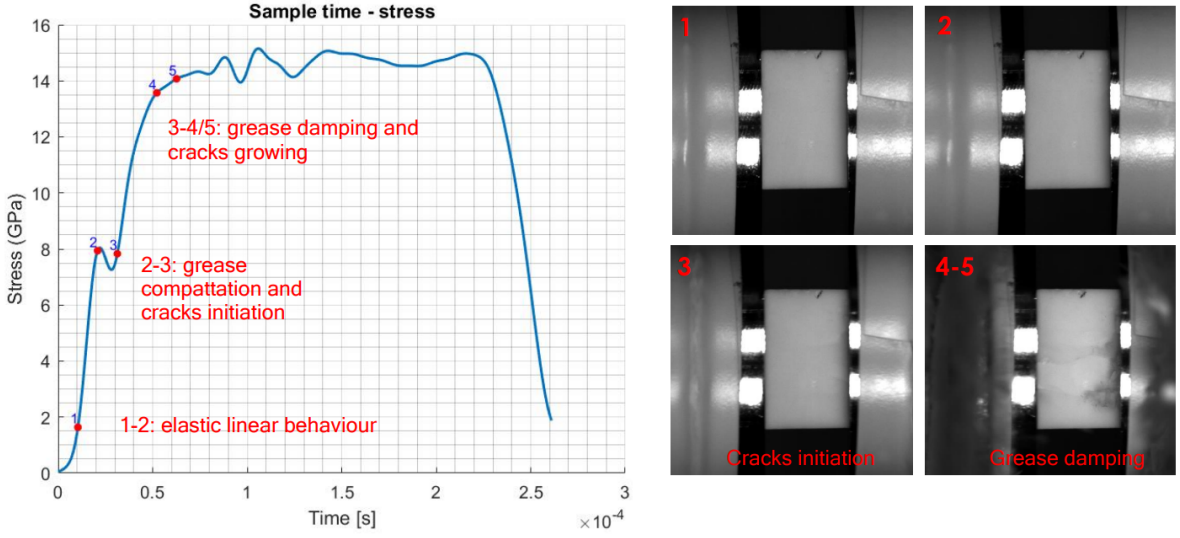

Figure 73: Stress-time plot of the 3 bar test (23 m/s). Comparing the curve with the images we can confirm the hypothesis that the presence of grease at the interfaces plays a decisive role in reducing the material stiffness and in the formation of an extensive region of constant stress with increasing strain.

4.5.2 Experimental data cleaning

As mentioned in the previous paragraphs (4.4 and 4.5), in order to compare the numerical simulations with the experimental results, it is necessary to clean the data eliminating oscillations in the curves that are believed to be due to disturbances and spurious elements such as the presence of grease, bar vibrations etc.

In particular, the curves were cleaned by retaining only the linear portions during the loading and/or unloading of the specimen. The validity of this methodology is supported by the comparison between the results of the Matlab algorithm on the curves generated by the Abaqus simulation and the stress and strain values recorded by the software. In fact, many of the mentioned issues remain even when using the algorithm on the deformation curves of the bars generated during the simulation: this implies that even in a clean environment, free of all the disturbances already mentioned (grease compaction, bar bending, etc.), there is still a considerable difficulty in extracting the data using the written Matlab code (and also using the "David" analysis software, which provides the same results), especially regarding the final strain value, as shown in figure 74a.
The stress values, on the other hand, are correct (see figure 74b), even if with a slight overestimation of the maximum stress.

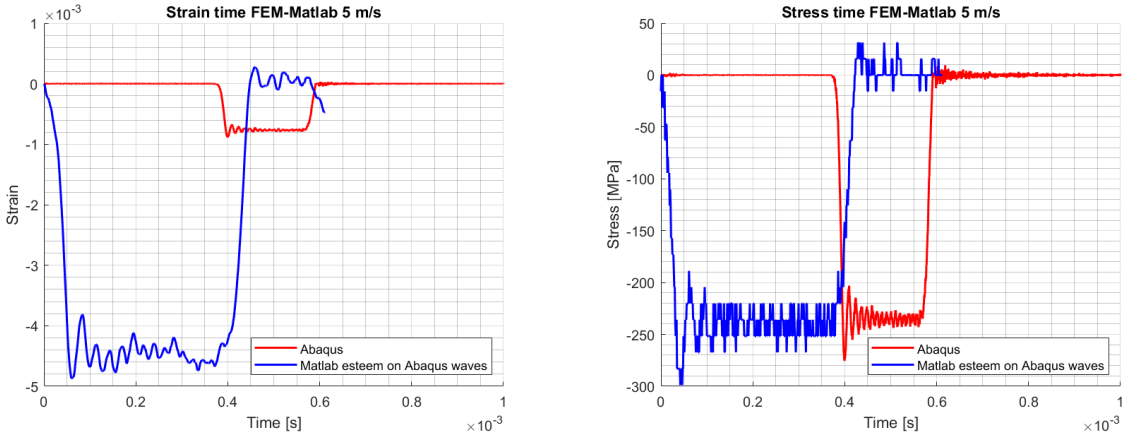

(a) (b)

Figure 74: Strain and stress "Abaqus" red curves are computed averaging the history output plots requested for some elements by the software.

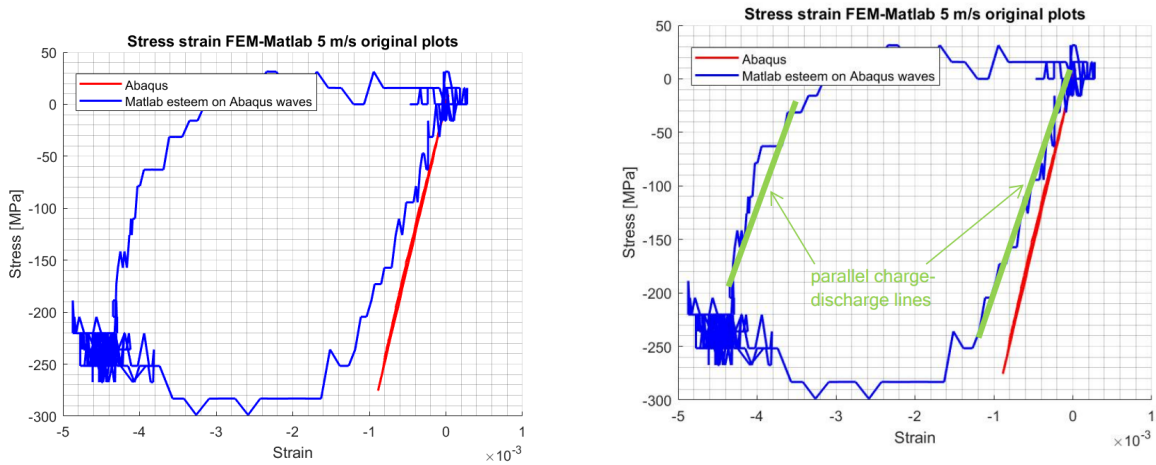

(a) (b)

Figure 75: Strain and stress "Abaqus" red curves are computed averaging the history output plots requested for some elements by the software.

If we consider valid the final stress values and Young modulus calculated from the first part of the curve, we can then obtain an almost exact estimate of the actual stress-strain curve computed by the software: this will be the approach for extracting data from the experimental campaign and comparing them with the numerical results.
It is, however, absolutely necessary to correct and improve the Matlab code in order to properly analyze the data from upcoming experimental campaigns.

These results are nonetheless useful as a preliminary comparison with the experimental simulations and for the calibration of the parameters sets.
It is noted that the slope of the initial experimental curve, which is practically identical to that predicted by the numerical model, is the same for both the loading and unloading phase (figure 75b). The problem is attributed to numerical amplifications in Matlab, which requires the manual superposition of the bars deformation curves. This process inevitably introduces alignment errors. The result is an overestimation of the strain rate and, consequently, of the strain, leading to the semi-constant region in the lower part of the graph. As can be seen from the graphs, the Nadal set predicts with good accuracy the real behavior of the material in terms of stiffness and maximum stress.

4.6 FEM modeling

Two different FEM models have been created to simulate the two test conditions: low velocity with a smaller striker, and high velocity with a longer striker and tungsten spacers.
The numerical model replicates all the geometric features of the real testing system, and is composed of 4 or 6 parts, depending on the presence of the spacers:

- The striker ("Impacteur"), where the velocity field is applied and which generates the compressive wave following impact with the first bar ("Barre Entree");
- The input bar, which receives the impulse from the striker and transmits it as a compressive wave to the specimen, with which it is in direct contact (in low velocity tests) or via a tungsten spacer (in high velocity tests);
- The tungsten spacers placed between the bars and the specimen (high velocity tests);
- The output bar ("Barre Sortie"), which receives the compressive wave from the specimen, via the tungsten spacer in high velocity tests or directly in low velocity ones.

The simulation is an explicit dynamic analysis with a duration of 1 millisecond.
Simulations were performed at high velocity (23 m/s) in order to compare the behaviors of the two parameters sets "Nadal" and "Holmquist" with the experimental results.

4.6.1 FEM model settings

As in the case of the three-point bending test, both the ceramic and the bars were modeled using explicit solid "C3D8R" elements (8-node hexahedral, linear, reduced integration elements).
The mesh size is different in bars and specimen, respectively 3 and 0.1 mm.

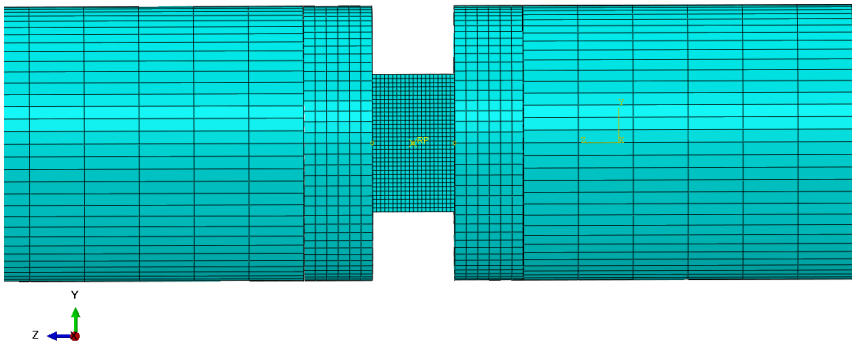

Figure 76: Detail of the FEM model for a high-velocity Hopkinson bar test. The central specimen is visible with the two tungsten spacers connecting it to the lateral bars.

A contact of type "normal behaviour/hard contact" was imposed between the contact surfaces of the model, and the "convert to particle" option was activated in the mesh card of the ceramic material. This option allows to resolve the numerical instability issues related to the excessive deformation of the mesh elements that can occur at high damage levels, by erasing the heavy distorted elements converting them into small pieces free to move in space. The threshold to activate material fragmentation and

conversion into small particles was set using a strain criterion of 0.2, which implies the destruction of the element when a 20% strain is reached. This value was chosen as analogous to the "FS" ("Fail Strain") parameter included in the parameter sets for JH2, which governs the elimination of the mesh element within the model routine: damage is accumulated up to a unitary value with degradation (but not complete annulment) of the mechanical properties, eventually leading to the complete removal from the calculation of elements deformed beyond 20%.

4.6.2 Numerical results: "Holmquist" parameters set

As can be seen from the following images, the "Holmquist" parameter set is able to predict the correct stiffness of the system, but fails once the maximum stress is reached. This is not in accordance with the experimental data, as fracture in the numerical model is catastrophic and occurs since the material dynamic compressive strength is reached, while the experiments show just some little cracks due to local defects (the compressive strength is not reached: we can't observe the typical strain drop in reflected wave).
The failure is clearly visible with the sudden surge in strain in figure 77a and in stress in figure 77b.

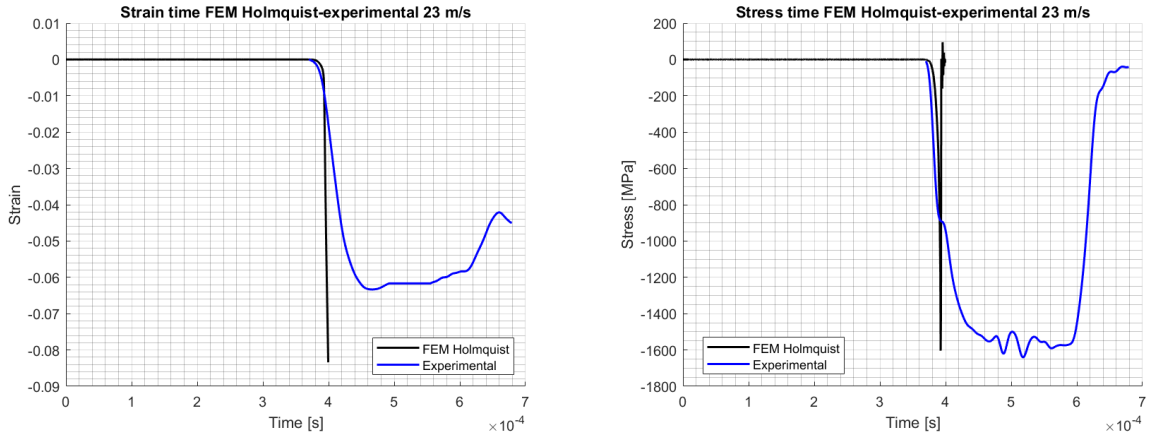

(a) (b)

Figure 77: Experimental and numerical strain and stress comparison at high velocity (23 m/s) with the "Holmquist" parameters set. The spike in strain and the sudden drop in stress indicate that the material undergoes catastrophic failure.

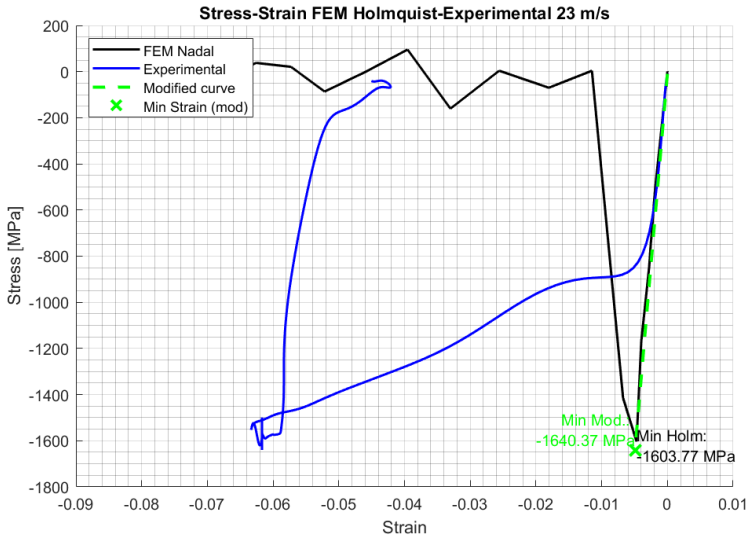

Figure 78

The result indicates that while the set is able to predict the correct behavior under static loading, as observed in the three-point bending test (36), it underestimates the material strength when subjected to dynamic loads. This is due to the low level of the Hugoniot Elastic Limit (HEL): when the stress exceeds this value, a transition from elastic to plastic behavior occurs with a rapid accumulation of damage governed by the coefficient D ($0 < D < 1$).
In fact, the HEL value determines the dynamic strength of the material and is measured under impulsive or shock loading conditions: it is therefore not a static strength limit but a dynamic parameter that depends on the loading rate. We can conclude that the HEL value of the Holmquist model is calibrated on a static case and therefore underestimates the material strength under dynamic loading.
In the following figures the fracture pattern of the specimen during the dynamic compression phase is presented. It is useful to visualize the results using the state variable $SDVPEEQ$ ("Plastic Equivalent Strain"), which indirectly manages the accumulation of damage in each element: damage develops proportionally to the plastic deformation, degrading the material properties as it increases (once D=1 is reached, the element has only a residual degraded strength as determined by the damage equation, see equation 7).

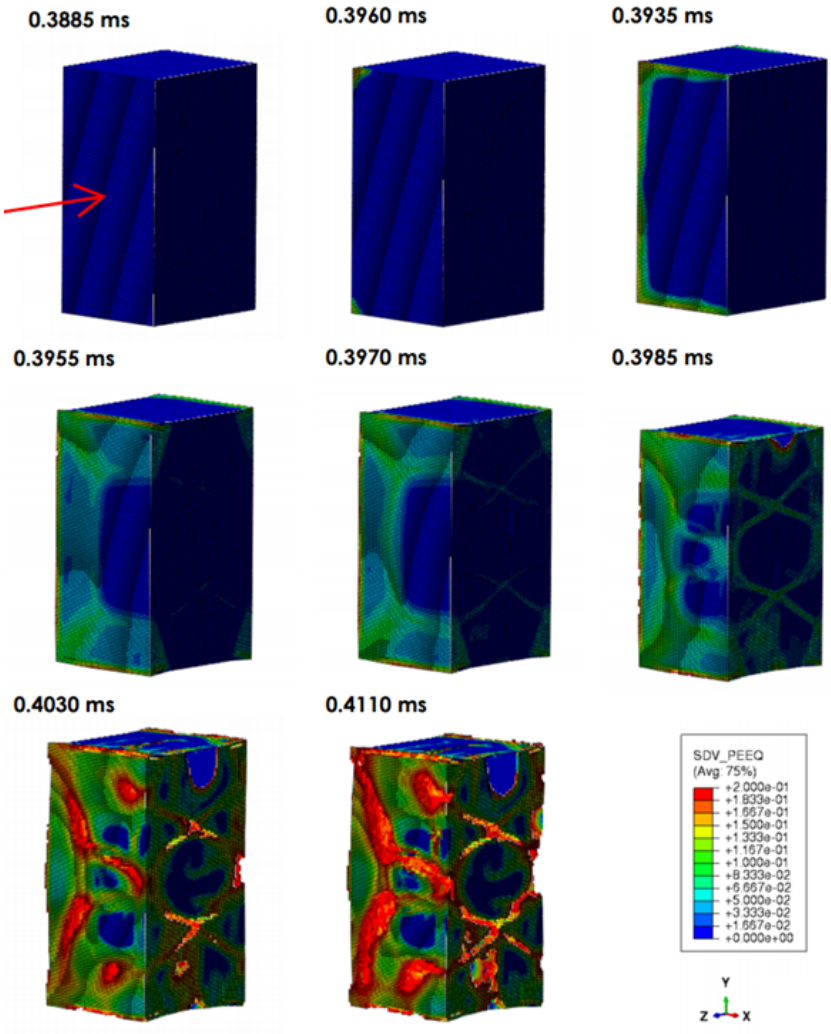

Figure 79: Specimen damage history in the 23 m/s Hopkinson bar test using the "Holmquist" parameters set. The arrow indicates the direction of the applied load and is normal to the contact surface between the input bar and the specimen. The variable $PEEQ$ represents the accumulation of equivalent plastic strain, directly linked to the damage variable. When $PEEQ$ reaches 0.2, the damage becomes complete (as determined by the Failure Strain = 0.2). In Abaqus, the "convert to particles" option was activated: beyond a certain deformation, the element is removed. The specimen is shown in section.

We can observe that, except for the low predicted failure stress level, the fracture pattern is similar to the real one.
The difference with the experimental results is that fracture here happens at the first loading wave and is catastrophic, while the laboratory tests show a real fracturing just in the second reverberation returning wave.

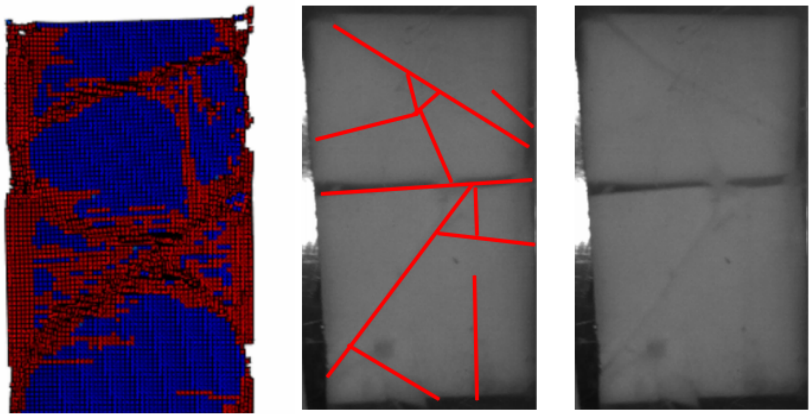

Figure 80: Comparison between the fragmentation predicted by the "Holmquist" set on the first wave and that observed experimentally on the second returning wave.

Indeed the experimental fragmentation shown in figure 80 is not caused by the initial compressive wave (the one of our interest), but rather by the subsequent reverberation and impact with the tungsten carbide spacers. Thus, our previous observations remain valid: there is no widespread fragmentation in the high-velocity tests, but only isolated fractures caused by superficial defects.
This final consideration is based on the fact that the reflected and transmitted curves do not show any sign of the ceramic yielding. This indicates that even in the presence of fractures, the material is still able to withstand the impact, and the fracture has essentially no effect the material dynamic response. A very different effect would occur if the specimen were to undergo catastrophic failure due to a generalized exceedance of its dynamic compressive strength.

4.6.3 Numerical results: "Nadal" parameters set

The model behaves in good agreement with the experimental data at both high and low velocities: the material remains in the linear elastic phase, reaching a significantly lower stress level but with correct stiffness. Moreover, as in reality, the numerical model has only minor scattered damage due to local failure of some elements. The fractures in the 23 m/s experimental test are due to defects on the ceramic surface and not to the material exceeding its compressive strength: the absence of catastrophic damage in the numerical result is therefore completely consistent with reality, as there are no defects in the model acting as stress concentrators for major cracks development.

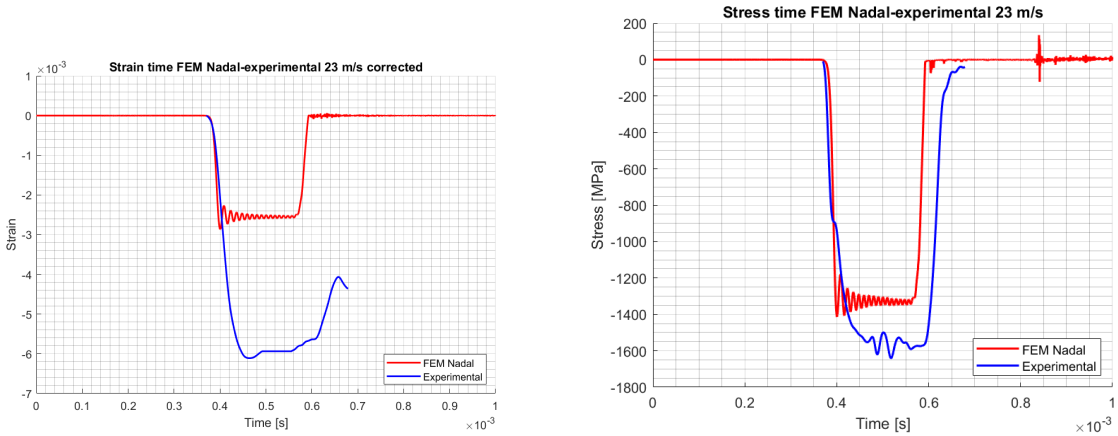

(a) (b)

Figure 81: Comparison between strain and stress of the experimental and numerical case at high velocity (23 m/s) with the "Nadal" parameters set. Strain and stress "Abaqus" red curves are computed averaging the history output plots requested for some elements by the software.

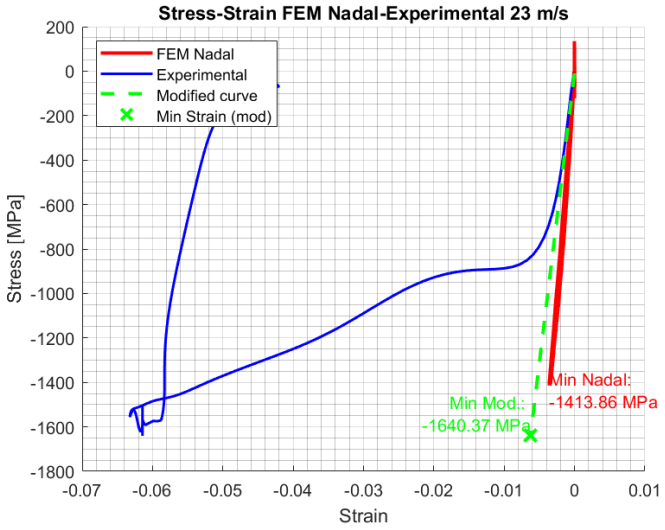

Figure 82: Final results: the original experimental stress-strain curve (in blue) is shown alongside the corrected one, which considers only the linear modulus of the loading and unloading phases and the maximum stress level reached (in green).

As explained before, the experimental curves were corrected by considering as valid only the elastic modulus calculated from the linear, parallel portions of the loading and unloading phases and the maximum stress level reached during the test. The maximum strain was recalculated based on these two values using Young's formula, and a linear curve with the determined stiffness was then plotted up to the new maximum stress and strain point (green line in figure 82).

Figure 83 shows an image of the stress distribution within the sectioned specimen.

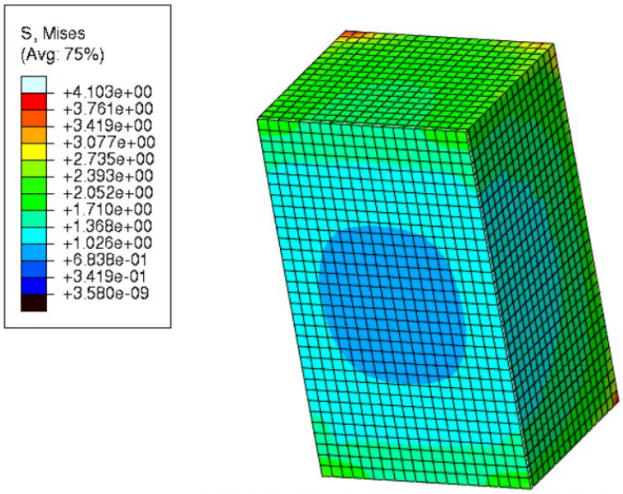

Figure 83

It can be seen that the stresses in the central area of the specimen are much lower (up to more than 2 times lower) than those in the peripheral areas. This complicates the acquisition of average stresses, which must necessarily be obtained from Abaqus via a history output on specific elements.
The stress was therefore averaged among various central and peripheral elements. As mentioned, the material undergoes slight scattered damage without experiencing catastrophic failure, exactly as in the real case where micro-fractures form due to surface defects. In both cases, these damages are not detected by the reflected and transmitted waves, indicating the preservation of the material structural integrity. In the figure 84 is shown the image of the damaged numerical model.

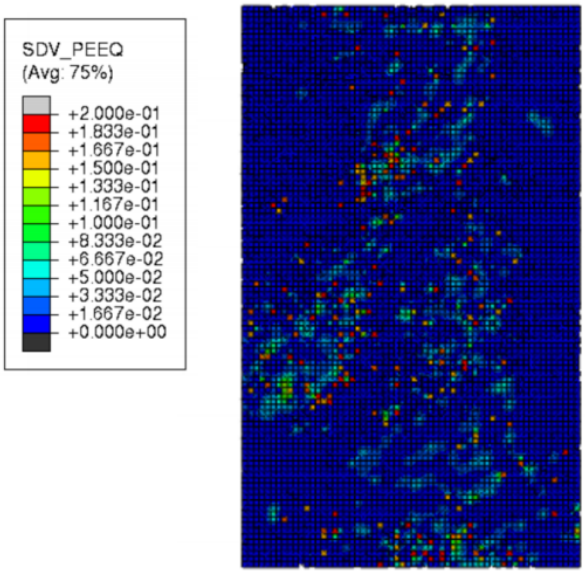

Figure 84: Damage on "Nadal" material model. The PEEQ indicates that there is plastic strain accumulation, that brings to damage and failure in some scattered elements. This damage doesn't affect the structural response on the material and the reflected and transmitted waves, just like in the reality.

4.6.4 Conclusions

Considering the "correct" experimental stress–strain curve reconstructed based on the initial elastic modulus value and the maximum stress computed by the MATLAB code, it is possible to scale the "raw" strain values output from the experimental test in order to reduce them and bring them closer to the estimated real value.
In figure 86, the comparison graphs between the numerical models and the original and corrected experimental results are presented.

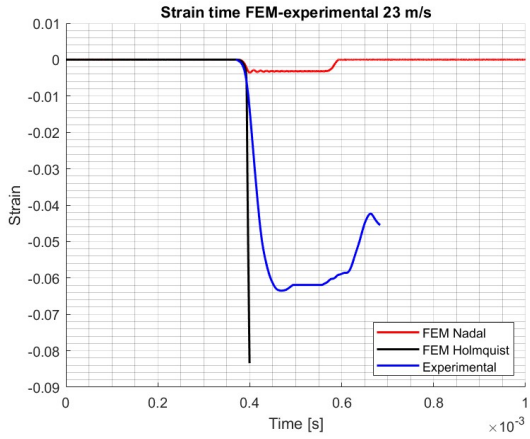

(a)

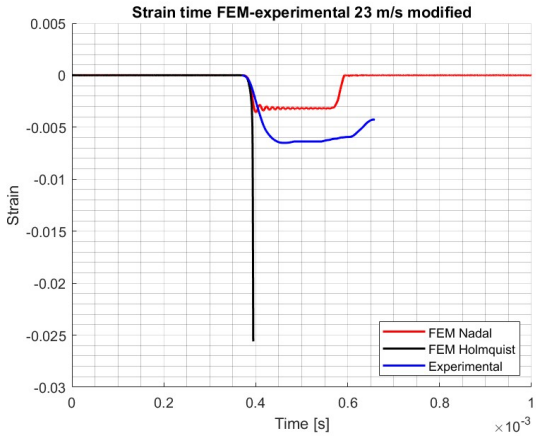

(b)

Figure 85

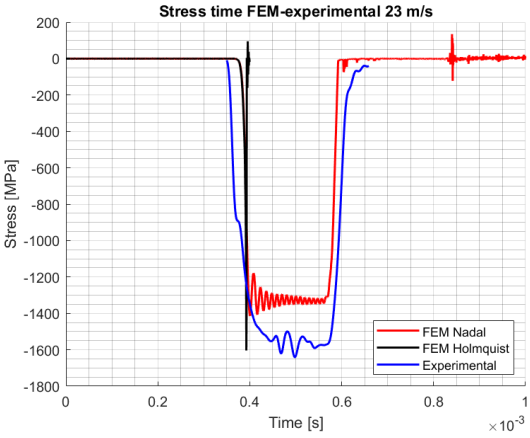

(a)

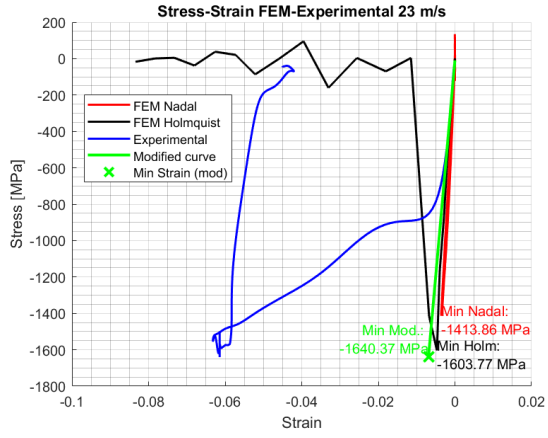

(b)

Figure 86

As can be observed, when considering the corrected experimental curve, the stiffness is extremely similar to that predicted by the FEM model, as are the stress values. In contrast, the original strain values are completely distorted: this is due to the multitude of experimental factors already investigated as well to issues related to data processing by the Matlab algorithm, particularly regarding the reflected wave.
On the other hand, there are no problems in the stress calculation, which is based on the transmitted wave (Equation 13).

4.7 Hopkinson bar test: Conclusions

Analyzing the numerical results it is evident that both parameter sets successfully predict the real material stiffness, as confirmed by the bending test data. While the "Nadal" parameter set slightly underestimates the stress levels achieved during the test, the "Holmquist" set, on the contrary, experiences catastrophic failure prematurely.
In the dynamic case, we observe that the material strength increases compared to that predicted by the "Holmquist" set, which almost exactly estimated the static failure load levels.
On the other hand, the "Nadal" set consistently exhibits linear elastic behavior with a scattered damage accumulation. This set is therefore considered the most appropriate for simulating the dynamic test: despite the fact that real tests show scattered fractures, these are not perceptible in the strain gauge recordings and are attributable to local failures caused by defects rather than to a catastrophic rupture as predicted by the "Holmquist" set.
It would be interesting to evaluate the impact of a localized defect in the mesh within the "Nadal" parameter set to assess its behavior and verify the formation of cracks in a manner analogous to the real case.

4.8 Hopkinson bar test: future developments

Considering the experimental results and the considerations made in paragraphs 4.4 and 4.5, we can compile a list of measures to be adopted in the next experimental test campaign:

- Eliminate tungsten spacers whenever possible. If they are necessary to prevent bar indentation, minimize the amount of grease at the interface as much as possible, taking care to thoroughly remove any excess (press firmly to expel all unnecessary grease);
- Conduct a preliminary leading test to obtain the deformation waves for a known material, in order to evaluate and, if necessary, correct any oscillations in the waves due to poor machine settings (for example, this could help us identify disturbances generated by any oscillatory motion of the bars caused by overly thin bars guides or excessive clearance);
- Display on-screen and save the acquisition times of each frame during the recording of the test images (in the present work, the times were reconstructed based on the camera frame rate and through a visual comparison between the specimen photos and the graphs);
- If possible, equip the setup with laser devices capable of recording the relative displacement of the bar surfaces during the passage of the compressive wave, in order to obtain an estimate of the specimen deformation;
- Develop a more robust Matlab algorithm capable of processing the test data comprehensively (both loading and unloading curves) and automatically.
- Modify the shape of the incident wave: to achieve constant strain rate deformation in extremely fragile specimens such as alumina, it is necessary to generate a "ramp" incident wave rather than a trapezoidal one. This can be done using the "pulse shaping" technique introduced in paragraph 4.1.1;
- If possible, produce smaller specimens to increase the stress and conduct fracture tests. Ideally, the specimens should be directly sintered in cylindrical form to avoid the introduction of surface defects due to cutting processes.

These measures will allow the obtaining of stress-strain curves at different strain rates and the calibration of the "C" parameter in the Johnson Holmquist II model for the increase in material strength with increasing strain rate.

5 Impact test

Ceramics are good candidates for ballistic protection systems due to their high hardness and relatively low weight. During an impact, the surface hardness of the ceramic plays a fundamental role in the deformation and damage of the projectile, and it is crucial to understand the interaction mechanisms between the ceramic and the projectile, as well as the material fracture mechanisms.
Damage in ceramics subjected to impacts manifests in various ways: from the formation of cracks due to brittle behavior to ductile plasticity when sufficient confinement is present. Understanding and modeling the fracture behavior of ceramics is a task as challenging as useful to improve the performance of ballistic protections.
The primary test from this perspective is undoubtedly the impact test conducted with a gas gun, where a projectile impacts the ceramic protection at high velocity. Such test provides very useful information about the protective capacity of the ceramic, but it is expensive and complicated to perform. Moreover, after impact, the ceramic is often pulverized, making it very difficult, if not impossible, to trace the mechanism of damage of the material.
A simpler method for studying fracture in ceramics is provided by drop tests of spherical projectiles at relatively low velocities. Such tests exhibit many similarities to high-velocity impacts, maintaining the projectile-target interaction and preserving a dynamic nature, albeit at lower speeds.
The target fracture in these cases is much less catastrophic but analogous to that of higher-energy impacts: the primary failure mechanism of the ceramic remains similar to that observed in the case of projectile impact and manifests in the formation of conical, radial, and lateral fractures.
On the other hand, the absence of material pulverization and reduced fragmentation allows for a post-mortem study of the fractured specimens and the identification of various failure criteria in the material.
In order to observe the fragmentation mechanisms and validate the behavior of numerical models, 18 impact tests (commonly referred to as "drop tests") were conducted on 6 different ceramic plate configurations.
The objective is to compare the numerical values of force and displacement with those obtained from the experimental tests and to validate the ceramic fragmentation pattern, in order to determine which model performs best under dynamic conditions and, if necessary, refine its parameters.

5.1 Impact tests: mechanisms of dynamic fracture in ceramics

Before analyzing the fractured specimens and comparing them with the results of numerical simulations, it is of primary importance to recall the fracture mechanisms observed in the literature during impact tests.
The main failure mechanism observed in medium-low velocity impact tests is "cone cracking": the fracture develops in the initial moments of the impact, starting from the central zone, and continues to grow, widening toward the sides as the contact area with the projectile increases.
Subsequently, other failure mechanisms develop, primarily radial cracking and lateral cracking.
Additionally, at medium-high velocities, a "quasi-plastic" zone is observed immediately below the impact zone, where the ceramic, confined by the surrounding material, finely fragments and undergoes slight plastic deformation.
In Figure 87, an example of the fracture pattern of ceramics under the impact of a spherical projectile at medium-low velocities is shown: it is possible to distinguish the conical structure, main fracture mechanism, which originates from the boundaries of the projectile and expands through the thickness until it reaches the lower surface of the plate. This type of fracture is extremely important in the projectile-stopping mechanism, as it allows the ceramic to increase the final contact area of the damaged material with the lower layer of the armor, which is responsible for absorbing energy through deflection. The replication of this conical structure is therefore of vital importance in evaluating the effectiveness of the numerical model: one of the purposes of using the first layer of ceramic material is precisely to increase the energy dissipation area, in addition to reducing the penetrating power of the projectile by plastically deforming its tip.

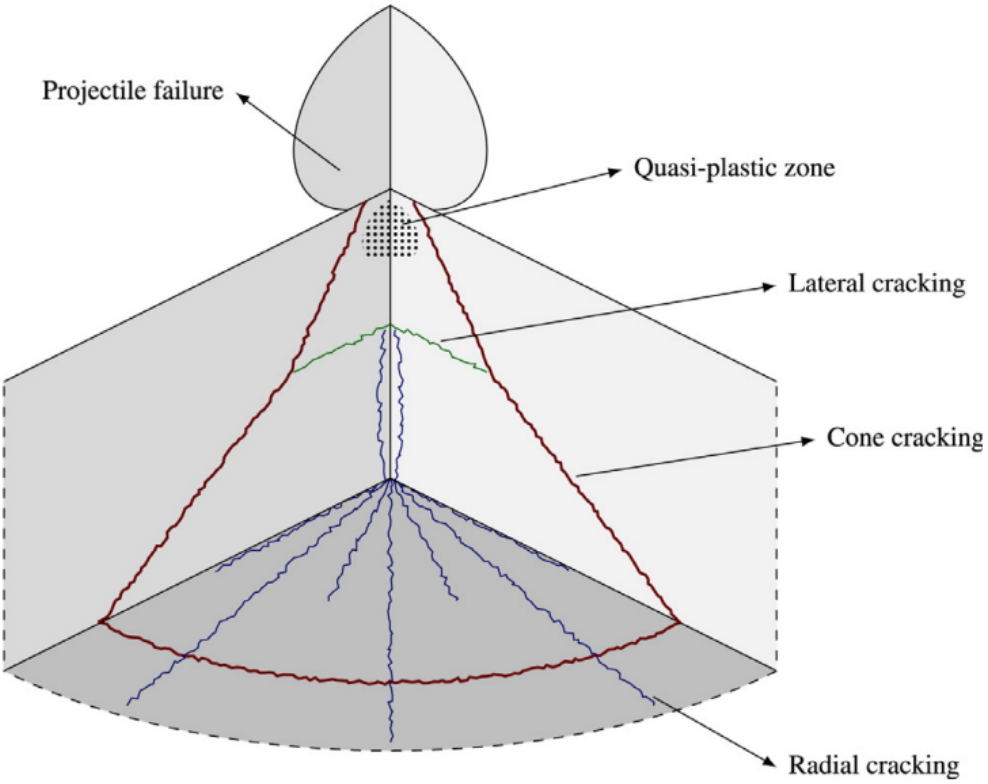

Figure 87: Crack pattern in ceramic under point of impact [20].

Another extremely important feature in evaluating the effectiveness of the numerical model is certainly the presence and number of fracture lines on the plane of the plate. Fractures of this type are called "radial cracks" and originate from the point immediately below the impact, extending to the edges of the plate while crossing the conical fracture lines perpendicularly.
Finally, in figure 87, transverse fracture structures can be observed, acting as a "bridge" between the sides of the cone fracture. Such structures are called "lateral cracking" and are typically found immediately below the impacted zone. In general, we can consider this latter fracture mode as secondary compared to the mechanisms of cone and radial cracking, as it mainly forms during and after the unloading and rebound phase of the projectile ([20]).
As previously explained in the chapter 1.3, the formation of cracks in ceramics following an impact is related to shock wave propagation phenomena: at the moment of projectile impact, a compressive shock wave is generated and propagates through the material. This wave reflects at the lower interface of the plate and returns as a tensile wave, which ceramic materials cannot withstand well due to their very low tensile strength, especially when compared to their compressive one.
This mechanism explains the timing of the various fracture modes in the impacted target: after the initiation of the fracture cone at the contact point between the projectile and the plate, the reflected wave leads to the development of radial cracks, which propagate both radially and vertically. It should be noted that starting of damage and the formation of radial cracks does not occur immediately upon the arrival of the compressive wave but requires some time to develop as the wave amplitude reaches the dynamic fracture threshold. Clearly, this time varies depending on the impact velocity, which modifies the amplitude and energy associated with the compressive wave (and consequently, the returning tensile wave) ([20]).

5.2 Experimental setting

The test was conducted using a specialized machine that allows the controlled release of a mass connected to a spherical impactor, inside which accelerometers are positioned. It is therefore possible to record the time history of the impact force experienced by the impactor, which will later be useful for comparison with the numerical model. The equipment also allows for the recording of the displacement undergone by the back of the impacted plate through a laser displacement sensor positioned below the impact point.
The machine consists of:

- Aluminum support structure, equipped with a steel base plate for the sample, featuring a central window that allows the deflection of the lower side of the impacted plate (detail 1 in fig 88);
- Impactor with a release mechanism and height adjustment (detail 1 in fig 88), allowing the variation of the kinetic energy associated with the impact. The impactor has a hemispherical shape with a radius of 8 mm and houses an accelerometer inside;
- System for acquiring the displacements of the back of the plate, implemented using a laser sensor.

Figure 88: Experimental machine for impact tests: "1" indicates the steel base plate with the window to observe the posterior deflections of the impacted plate, "2" indicates the loading system (i.e. the impactor with an accelerometer connected to the impact mass). The image on the right shows the placement of the aluminum plate ("3") above the window.

For our tests, an impact load of 2.236 kg was used with a terminal velocity of 4.23 m/s.

5.3 Test description and data aquisition

The tests were conducted on alumina plates with dimensions of 90x90 mm and a thickness of 6 mm. The samples were tested with different backing configurations, as preliminary tests highlighted that the system response varies significantly depending on the materials used in the layers placed behind the ceramic layer.
One of the objectives of the test will therefore be to understand how the backing layers influence the ceramic response to impacts and to verify if the numerical model correctly captures the system

behaviour. The numerical simulations have been carried out just in the configuration without any interlayer and the elastic interlayer effect has been analyzed just in a qualitative way.
A total of 18 impacts were performed on 6 different sample configurations (figure 89):

- Configuration 1: the ceramic plate is simply placed on an aluminum plate, which is placed on the steel test bench;
- Configuration 2: similar to the previous one but with a layer of double-sided tape between the ceramic plate and the aluminum backing;
- Configuration 3: a 1 mm thick layer of silicone elastomer is placed between the ceramic and the aluminum. The layers are all simply placed on top of each other;
- Configuration 4: similar to configuration 3 (ceramic - elastomer - aluminum simply placed) but with a 2 mm thick layer of silicone material;
- Configuration 5: similar to configurations 3 and 4, but with a central layer thickness of 3.5 mm;
- Configuration 6: similar to configuration 5 (ceramic - 3.5 mm elastomer - aluminum) but with double-sided tape between the layers.

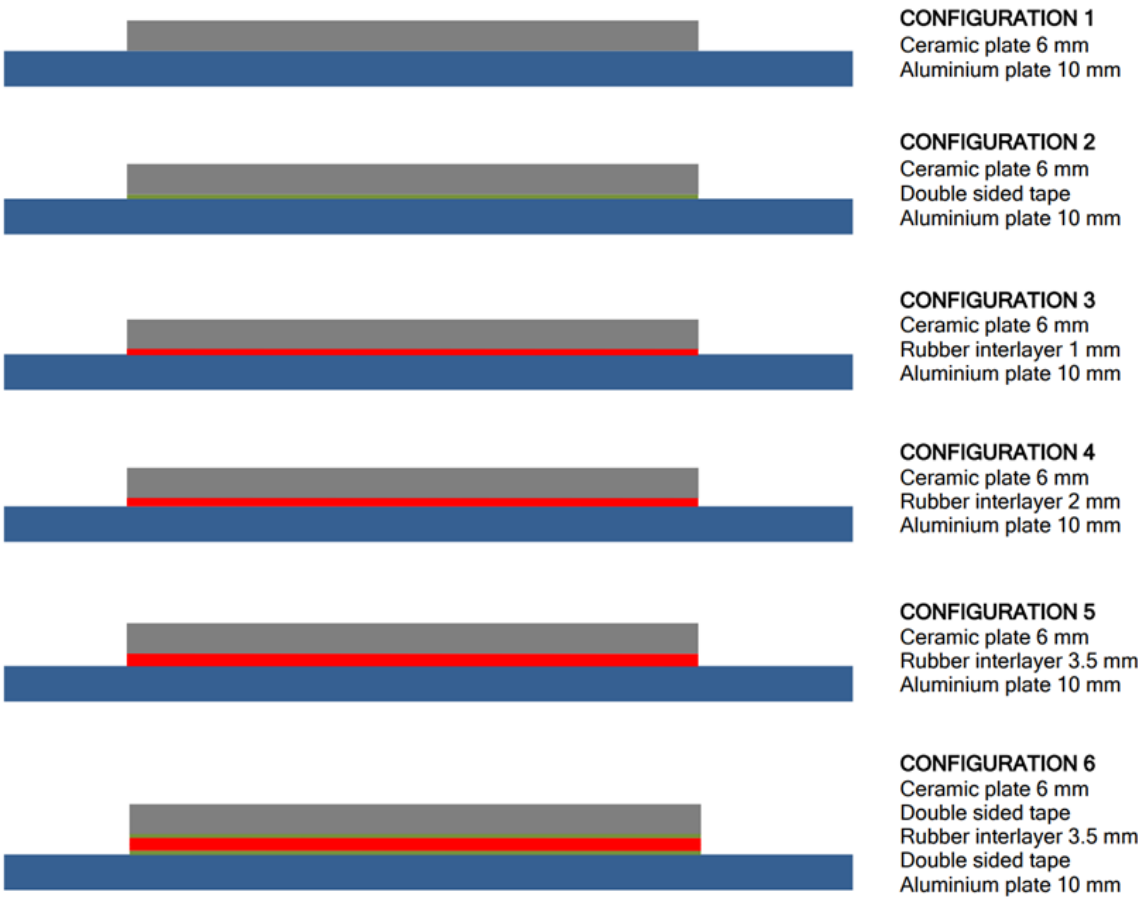

Figure 89

During the test, the load history on the impactor (figure 90) and the temporal deflection of the back of the aluminum plate (figure 91) were acquired. here are reported just the plots for the tests deemed most representative (configurations 1, 3, 4, 5).

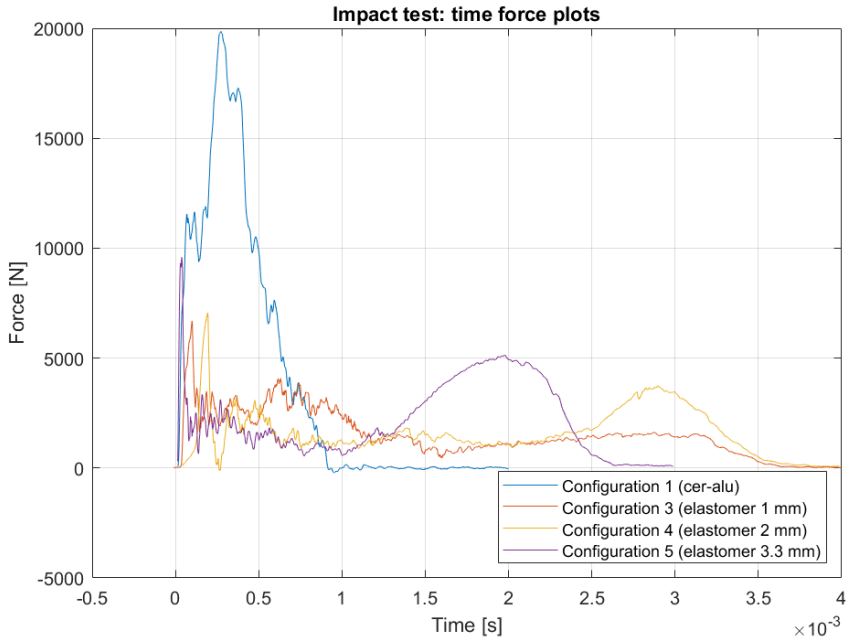

Figure 90: Force-time graphs of the drop tests conducted in the laboratory. The force was obtained by multiplying the vertical acceleration recorded by the accelerometer in the impactor by the mass of the impactor. The graphs related to the most representative tests (configurations with and without elastomer interlayer) are shown.

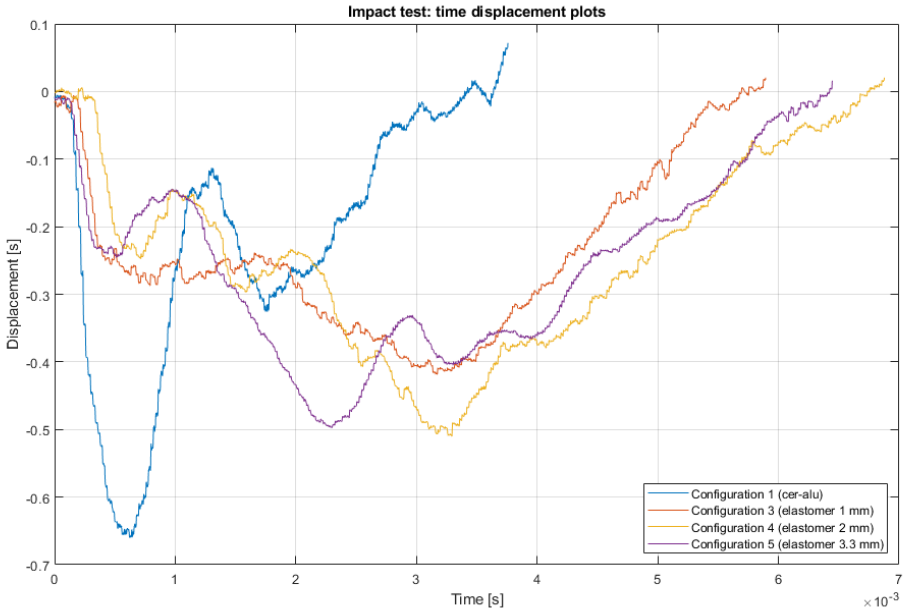

Figure 91: Displacement-time graphs related to the most representative tests (configurations with and without elastomer interlayer). The displacement is the deflection recorded by the laser sensor on the aluminum backing.

As can be clearly seen from the graphs, the addition of an elastomer interlayer has the effect of relaxing the force peak on the impactor, "spreading it" over a longer period of time, while also significantly reducing the posterior deflection of the aluminum backing.
The effect of relaxing the reaction force and reducing the maximum deflection of the system appears to

be more or less independent of the thickness of the interlayer. In fact, the results shown seem to suggest that the best effect is achieved with the 1 mm thick interlayer, which exhibits slightly lower force and deflection peaks compared to the other two configurations with 2 mm and 3.3 mm thicknesses, and significantly lower peaks compared to the configuration without an interlayer.
This may be due to the damping effect on wave propagation and energy distribution introduced by the interlayer: the elastomer modifies the impact dynamics by acting as a shock absorber for the ceramic.

5.4 Specimen fracture analysis

It is extremely important to analyze the fracture mode of the plates to gather information on any differences due to the presence of the elastomer layer and to evaluate the accuracy of the numerical models in simulating the fracture pattern.
Below are the photos of the fractured specimens in the various configurations.

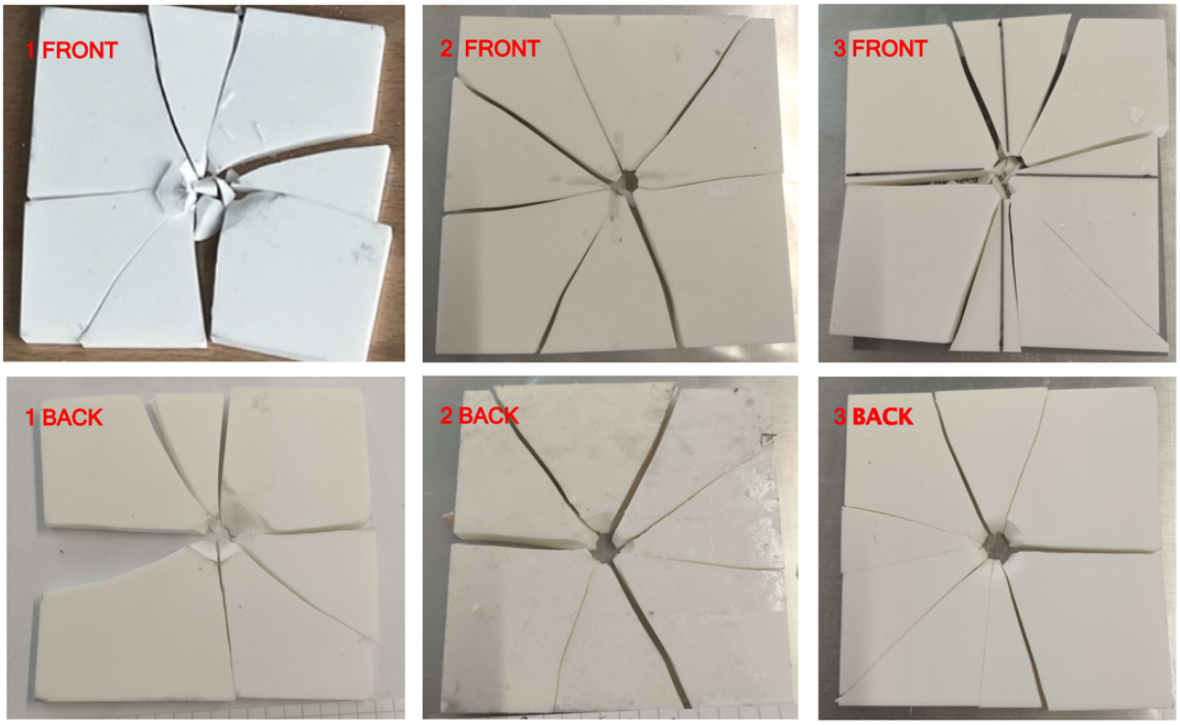

Figure 92: Fracture patterns of the tested specimens (configurations 1-3). Top photos represent the impacted front surface, bottom ones represent the back sides on the plates.

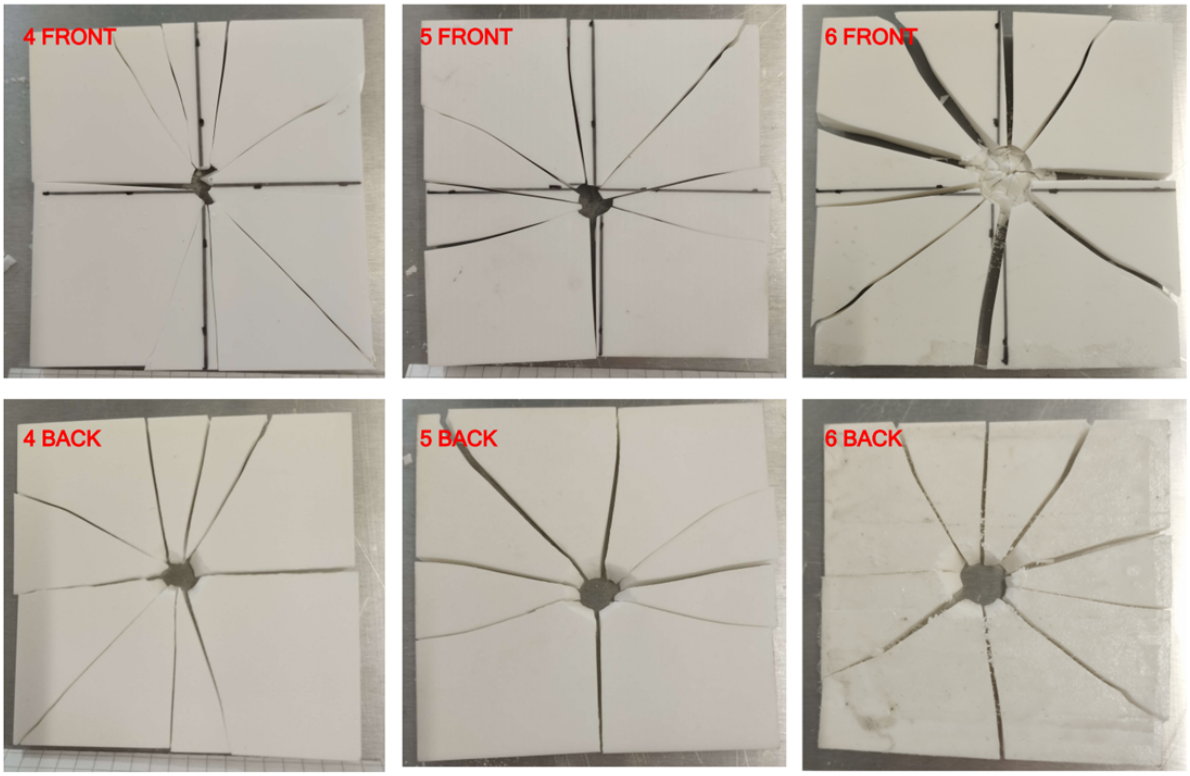

Figure 93: Fracture patterns of the tested specimens (configurations 1-3). Top photos represent the impacted front surface, bottom ones represent the back sides on the plates.

An effective numerical model is expected to predict with good approximation the number of fractures and, most importantly, the correct development of the fracture cone beneath the impact point. These data are therefore reported in Table 5.

Test	**Number of fracture lines (avg)**	**Fracture cone angle (avg)**	**Impactor footprint diameter (avg)**
Test 1	7	30–35°	10 mm
Test 2	7	30–35°	10 mm
Test 3	8	30–36°	11 mm
Test 4	9	34–39°	12 mm
Test 5	8	47–50°	13 mm
Test 6	9	48–52°	13 mm

Table 5: Fracture characteristics and impactor footprint diameter for each test.

It is noted that the addition of the elastomer layer tends to increase the number of fractures and widen the fracture cone.

5.5 FEM modeling

5.5.1 Model settings

A numerical model was implemented to reproduce the experimental setup of the drop test.
In particular, the following parts were modeled:

- Steel base with a window of the same dimensions and geometric characteristics as the one in the laboratory. The part was modeled as a shell starting from a 3D part using the "remove cells" command (rigid body);
- Aluminum support: the part is 3D, and the material is aluminum (Young modulus = 72 GPa, Poisson ratio = 0.33);
- Ceramic plate with dimensions 90x90x6, simply placed on the aluminum support. The plate has a finer mesh near the central impact point and expands toward the corners through three zones with different sizes (0.3, 0.5 and 0.7 mm as visible in 95b). The elements are "C3D8R" (8-node linear brick, reduced integration with hourglass control) and the "convert to particles" option was activated, similar to what was done for the Hopkinson Bar test;
- Steel impactor with solid properties and an elastic-perfectly plastic material. The Young modulus is 210 GPa with a Poisson ratio of 0.33 and a yield point of 1000 MPa. A small indentation was added to the spherical impact surface, as it was noticed in the laboratory that the impactor was not perfectly spherical. To simulate the mass of the entire structure combined with the impactor (element 2 in figure 95b), a reference point with concentrated mass was connected to the impactor using RBE3.

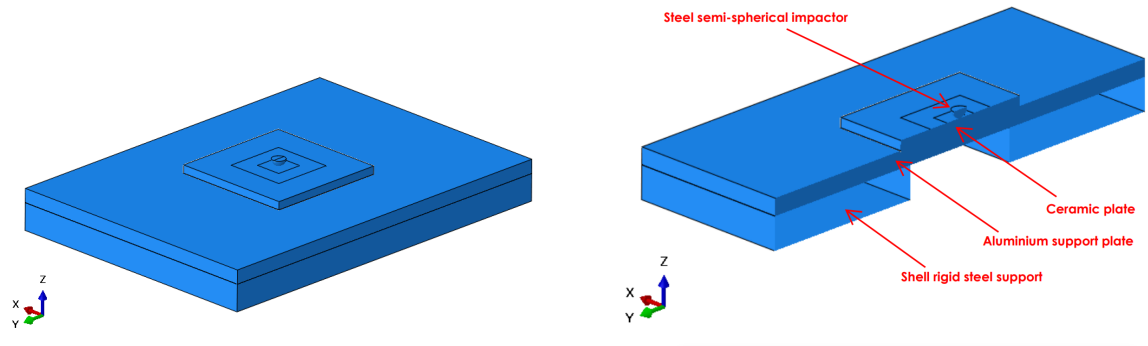

(a) (b)

Figure 94

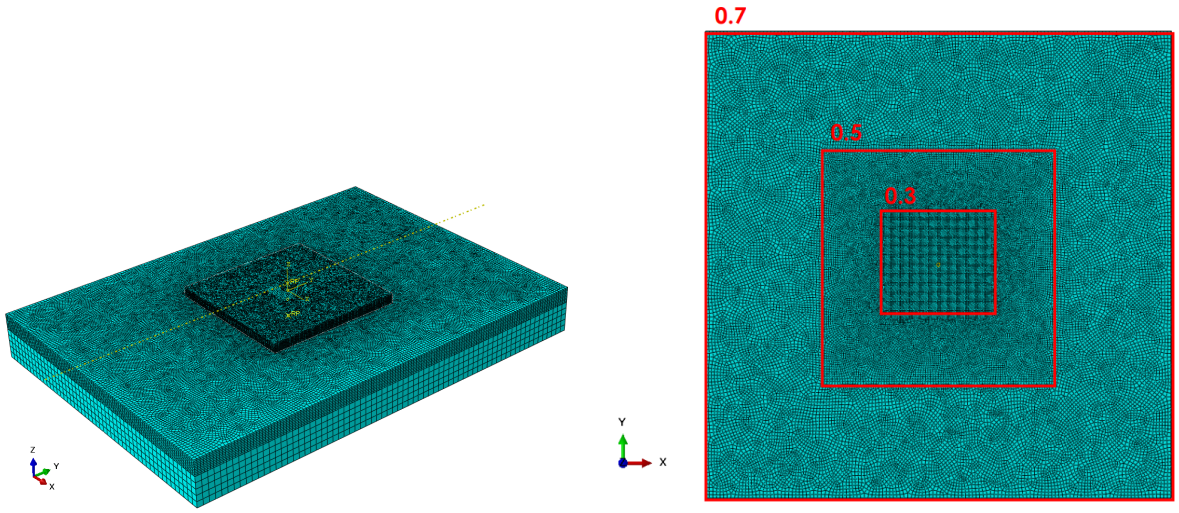

(a) (b)

Figure 95

The parts were brought into contact using surface contact definitions with a "hard contact" normal behaviour and a "penalty" tangential behaviour. The penalty value varies depending on the estimated friction coefficient: a value of 0.1 was set for the contact between aluminum and steel, and 0.05 for the contact between ceramic and aluminum, as well as ceramic and steel.
For models that involve fracture and element deletion, as in the case under examination, it is important to include in the contact definition the entire mesh of the ceramic with the other elements and with itself. This ensures the interaction of the fragments with the rest of the structure even after the material has fractured.
The simulation is of the dynamic explicit type, with a simulation time of 0.001 seconds, and the calculation is performed in double precision.

5.5.2 "Holmquist" parameters set

The model is able to predict with excellent precision the maximum level of reaction force on the impactor (96a), but with a wrong timing compared to the experimental test. Additionally, the deflection of the aluminum backing, calculated as the history output of the U3 displacement of the central point of the plate, turns out to be significantly different from the real one both in peak and duration (figure 96b).

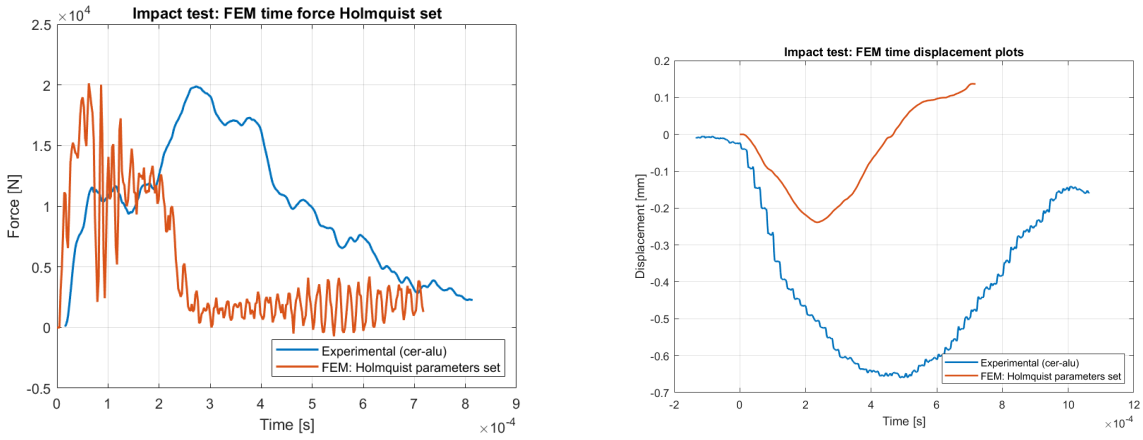

(a) (b)

Figure 96: Temporal history of force and displacement for the "Holmquist" parameter set. While the reaction force level is correctly captured by the model, the posterior deflection of the plate is much lower than the real one.

The shape of the force and displacement curves is very similar to that of the experimental case. In Figure 96a, two peaks can be recognized both in the experimental case (blue curve, at 0.1 ms and at 0.3 ms approximately) and in the numerical case (orange curve, the first peak at approximately 0.05 ms and the second at approximately 0.13 ms). In the FEM model, therefore, the impact phenomenon is faster compared to reality, and everything occurs and concludes earlier than in the experimental case. This is also confirmed by the plot of the backing deflection, which in the numerical case concludes within a few tens of milliseconds, returning to zero and bouncing back, while the experimental case is still at the plateau of the displacement curve.
Observing the fracture patterns, it is noted that the model predicts the development of five radial fracture lines (98) on the lower side of the plate, which originate from the impact point and stop when they encounter the outermost zone with a coarser mesh. Similarly, the fracture lines are unable to traverse the entire thickness, as seen in Figure 97, where only the imprint of the impactor is visible but not the radial cracks.
This phenomenon is attributable to the numerical effect caused by excessively large mesh elements: the elements do not accumulate damage correctly because the fracture energy is distributed over volumes that are too large, preventing adequate localization of the damage and thus the arrest of the crack.

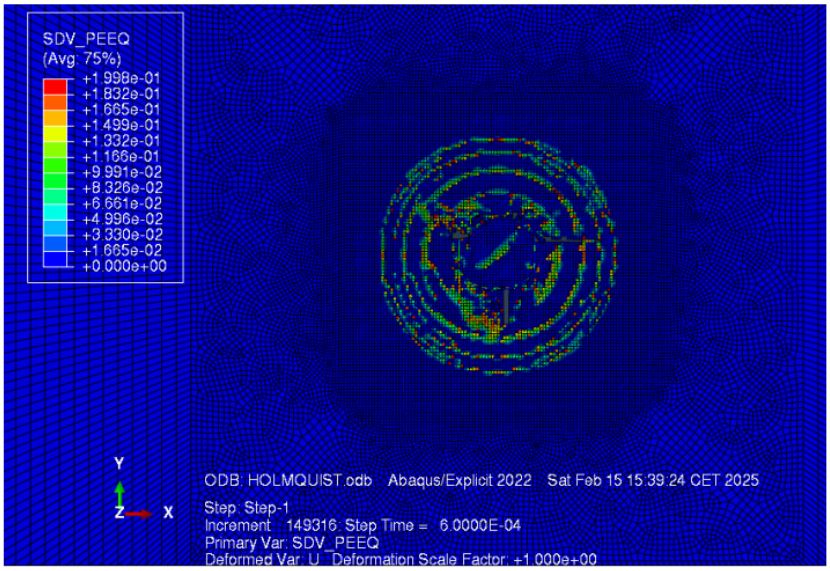

Figure 97: Impactor footprint on the upper side of the plate. The absence of radial fractures is due to the mesh size: the model fails to erode all the elements through the thickness, despite the fractures being present on the lower face of the plate.

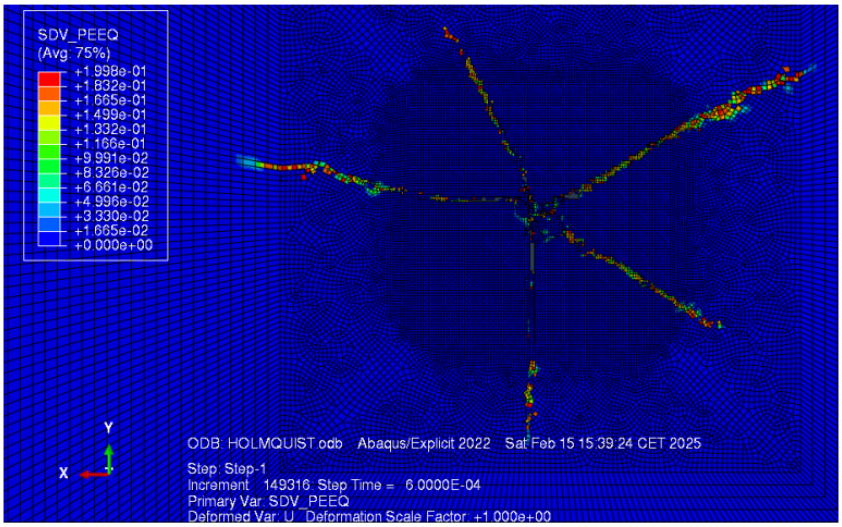

Figure 98: The "Holmquist" parameter set predicts the appearance of 5 radial cracks, which is fewer than observed in the experimental tests.

As visible from the imprint of the impactor on the upper surface of the plate in Figure 97, the sphere sinks into the ceramic material up to almost half of the plate thickness before coming to a complete stop, pushing the underlying material downward.
Fracturing occurs in multiple phases: Figure 99 shows the damage history in the ceramic section, with the damage variable ranging from 0 (intact element, in blue) to 1 (completely damaged element, in red). The various phases of material fracturing are visible, consistent with what is reported in the literature (1.3): the formation of a fracture cone occurs following the arrival of the compression wave at the aluminum-ceramic interface and its reflection as a tensile wave (visible at 10 μs in Figure 99), followed by the appearance of fracture lines at the edges of the contact surface with the impactor (20 μs in Figure 99).
After the initial moments, the impactor penetrates the material, pushing and crushing the fracture cone beneath the impact point (70-500 μs), eventually causing the erosion of the elements (evident at 500 μs in 99).
It can be observed that the appearance of the fracture cone and the development of radial cracks, along with the erosion of the elements, correspond to the drop in the reaction force in the graph in Figure 96a. This confirms the centrality of these two fracture mechanisms in absorbing the impact energy, as predicted by the literature.

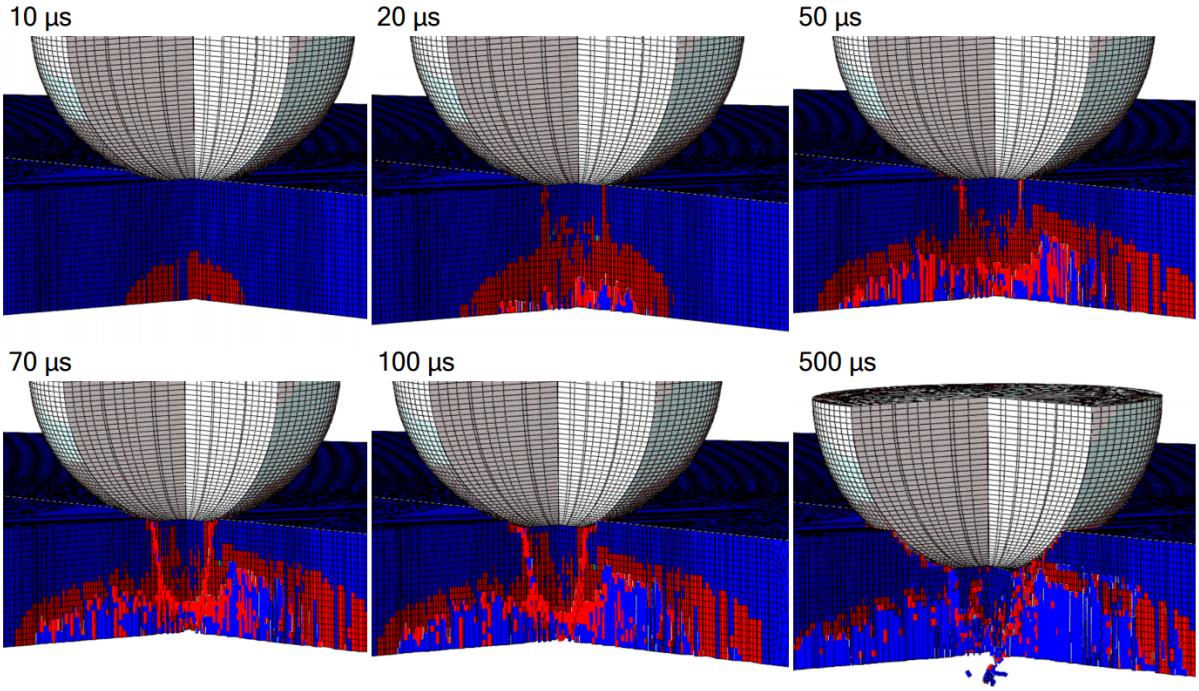

Figure 99

Due to the development of the fracture cone from the lower side of the plate and the weakening of the material at the edges, the impactor penetrates deeply into the thickness, pushing a sort of wedge of material downward, clearly visible from 70 to 500 μs. This "double cone" structure (Figure 101b) is observed in the experimental tests also, where this area is subjected to fragmentation and penetration of the impactor.
Anyway, the penetration of the impactor into the ceramic plate is much more modest in the experimental case compared to what is predicted by this simulation.

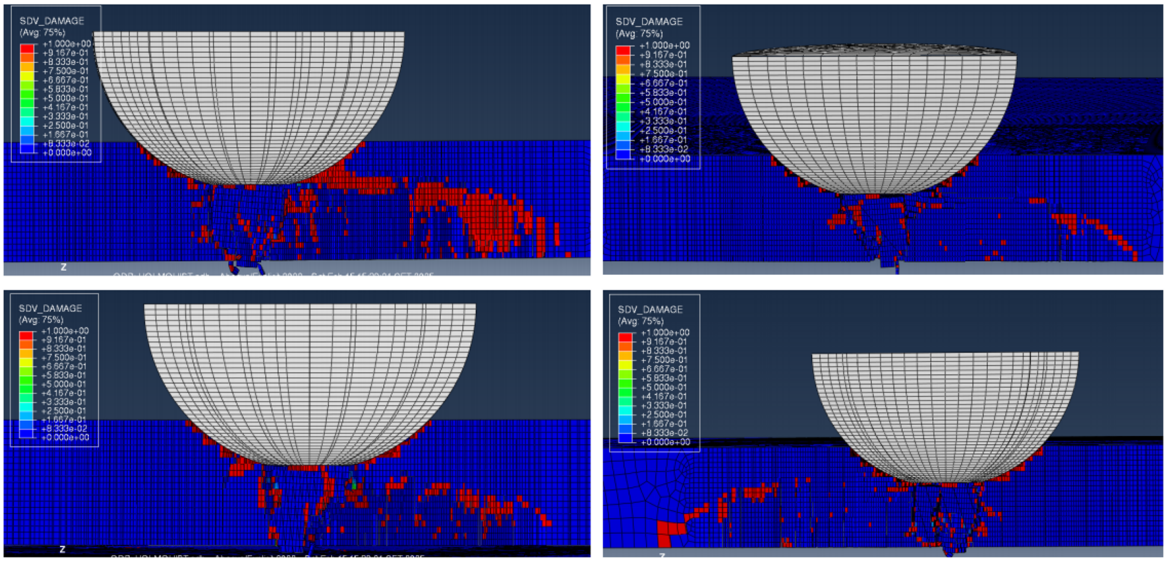

Figure 100

Figure 100 shows the sections corresponding to radial fractures to illustrate their structure. It should be noted that, for the reasons mentioned above, the coarsening of the mesh prevents the fracture from reaching the sides of the plate or traversing the entire thickness.
The sections shown in 100 were taken at four of the five fractures observed on the back of the plate to

demonstrate the evolution of the radial cracks through the thickness. It is important to note that these sections do not highlight the presence of the three-dimensional cone at the center of the plate: the damaged zone beneath the impact point overlaps with the radial fractures but is also present outside their planes.
The width and inclination of the damage cone are indicated in Figure 101a, along with the "inverse cone" pushed by the impactor into the thickness (Figure 101b).

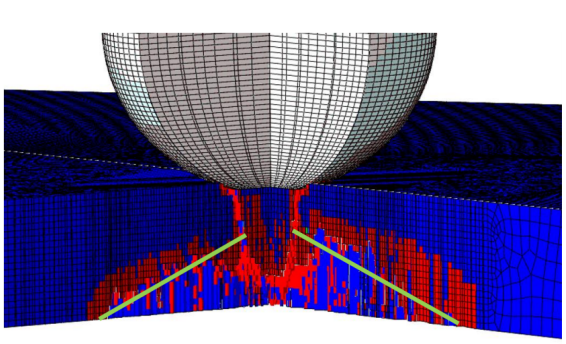

(a) The image shows the fracture cone immediately beneath the impact point. The presence of this structure reflects what has been observed in experimental tests and in the literature.

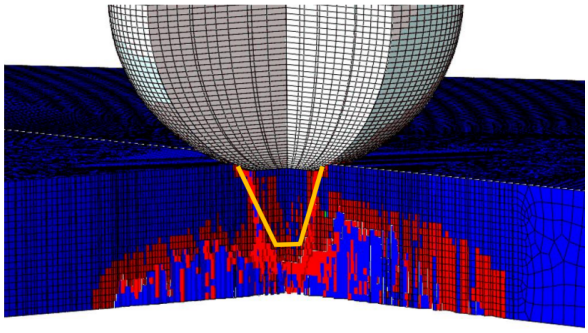

(b) The "inverse fracture cone" created by the impactor push on the damaged material is highlighted in yellow. This structure is present in the experimental tests also but with a reduced area, and could be a sign of excessive material damage.

Figure 101

A fracture cone inclination of approximately 25° is observed, which is lower than the experimental inclination (approximately 30-35° for this configuration, see Table 5).
In conclusion, the "Holmquist" parameter set is considered a good starting model. The main issues are due to the poor representation of the posterior deflection of the aluminum backing, likely caused by the rapid exhaustion of the impact phenomenon (visible when comparing the curves obtained in Figure 96) due to overestimated damage: the elements fail too early, absorbing a large amount of energy and not providing sufficient resistance to the impact. This is confirmed by the observation of the fracture, which shows greater penetration of the impactor into the plate than in reality and a more inclined (and thus more extensive) cone compared to the one observed experimentally.
A potential solution could be to increase the resistance of the fractured material (parameter B in Equation 8) or to adjust the damage parameters D1 and D2 in Equation 10. The main reference values obtained with the "Holmquist" parameter set are summarized in the table:

	Holmquist parameters	**Experimental values**
Max force on the indenter [kN]	20.1	19.9
Max displacement of the backing [mm]	0.239	0.66
Radial fractures	5	7
Fracture cone tilt angle [°]	20-25	30-35
Indenter imprint diameter [mm]	7	4-5

5.5.3 ”Nadal” parameters set

The model overestimates the levels of reaction force on the impactor but is much more accurate than the previous set in predicting the deflection of the aluminum backing, as shown in Figure 102.

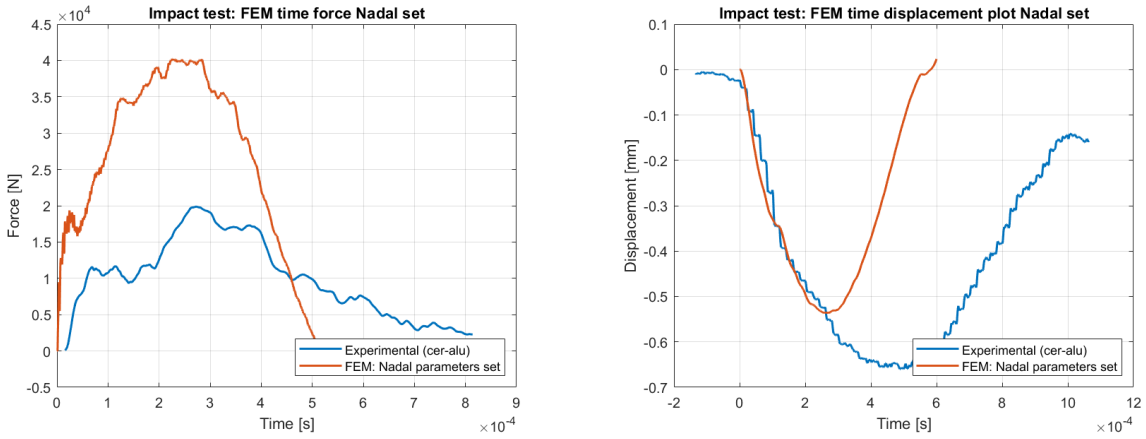

(a) (b)

Figure 102

Despite the calculated force level being almost double the real one, the shape of the force-displacement curve is extremely faithful to the experimental experience and very different from that obtained with the ”Holmquist” parameter set: the impact is gradually dissipated by the ceramic, which has time to distribute the damage and absorb the impact energy progressively.
In this case as well, two peaks in the force values are visible, the first at approximately 0.3 milliseconds and the second at approximately 2.5 milliseconds, almost perfectly aligned with the experimental ones. The initiation of damage is primarily regulated by the material Hugoniot Elastic Limit (HEL) value, which, as we know, is more than double in this set compared to the ”Holmquist” set. An almost directly proportional correlation is observed between the HEL value and the maximum reaction force recorded in the simulations: the ratio is approximately 2 for both the HEL values (6.570 vs 2.79 GPa, see Table 2) and the maximum force value reached.
The ”Nadal” set predicts the formation of radial fractures very faithfully to reality, both in number and distribution, as can be observed in Figure 104, while it falls short in representing the damage on the upper part of the plate: the impactor fails to penetrate the ceramic even slightly, and the damage develops in the areas surrounding the impact point rather than immediately beneath it (Figure 103). It should be noted, however, that although the elements in direct contact with the impactor are not damaged as they were with the ”Holmquist” parameter set (Figure 97), there is still damage in the surrounding elements due to the formation of the fracture cone, visible in the sections shown in Figure 105.

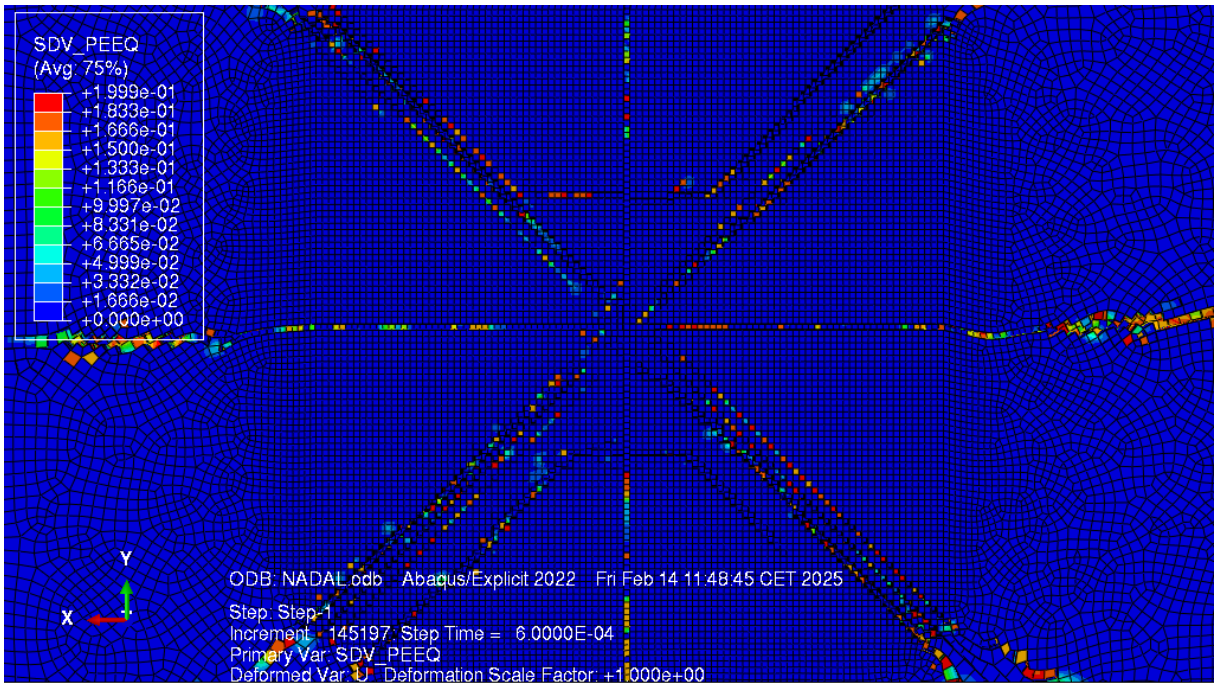

Figure 103

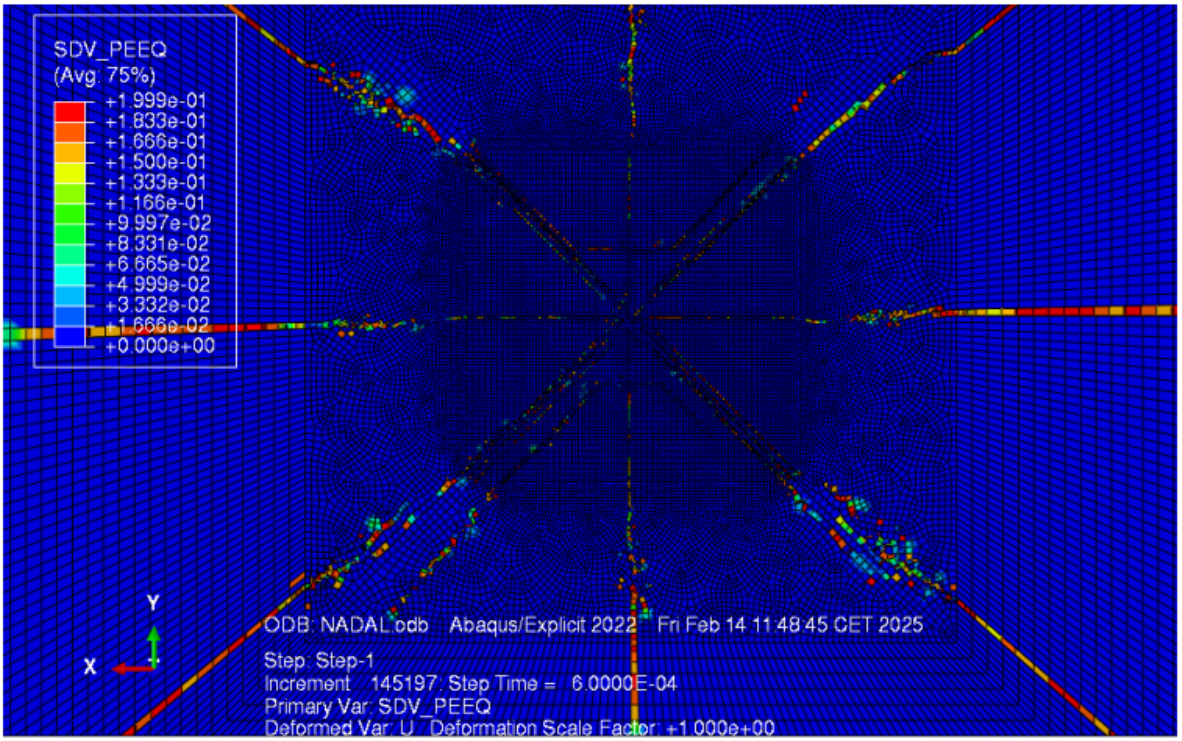

Figure 104

It may be useful to analyze the development of the fracture within the ceramic during the impact phenomenon: in figure 106, it can be observed that, similarly to what was obtained with the "Holmquist" parameter set, the material at the interface with the backing is damaged within the first 10 μs.

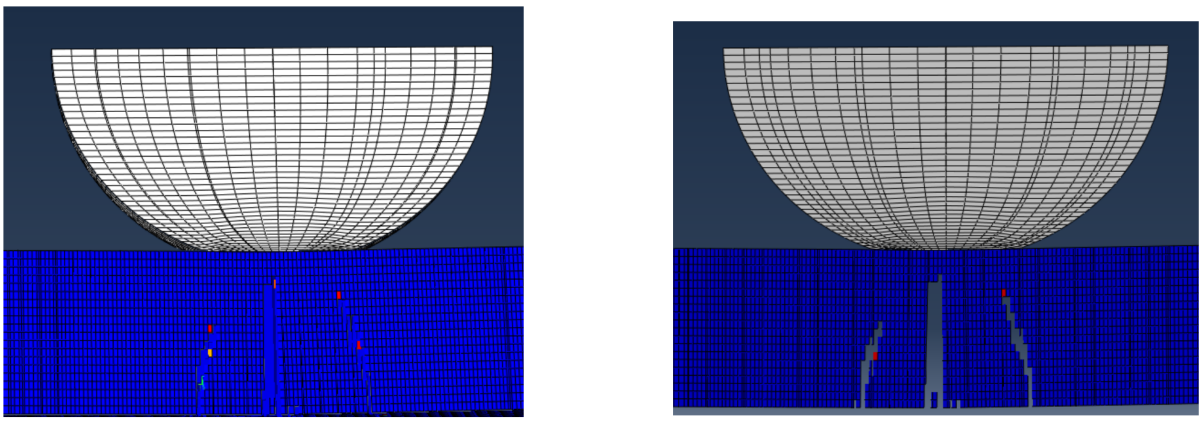

(a) (b)

Figure 105

This damage leads to the formation of a cone from which the radial fractures then originate, in accordance with the literature. Note that the images in figure 106 are taken at the fracture lines that develop starting from approximately 50 μs, and thus the fracture cone is not directly visible except in the initial moments of the impact (the damaged elements of the radial fractures cover the visualization of those related to the fracture cone).

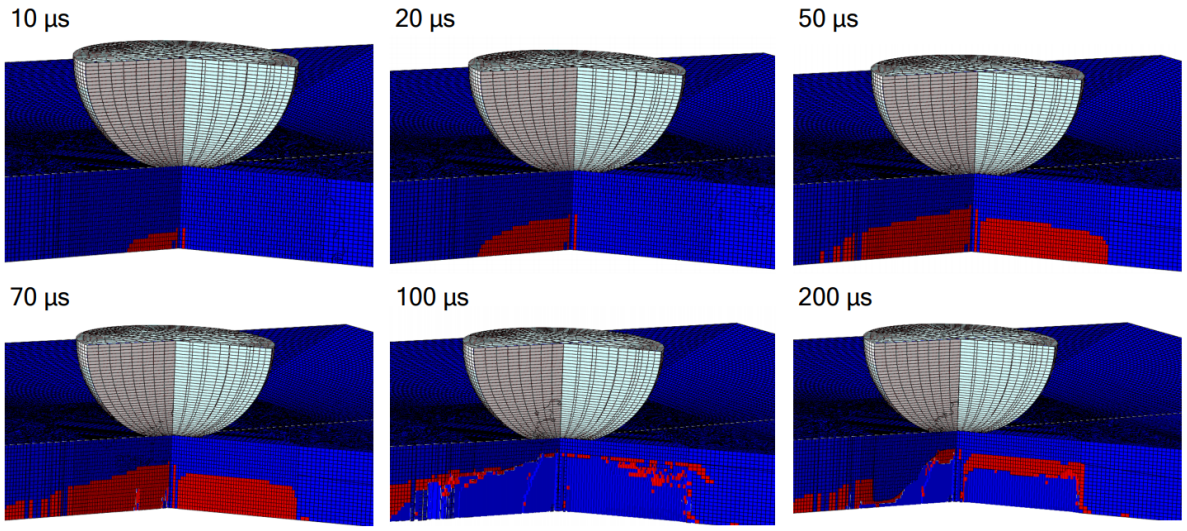

Figure 106

During the formation of the cone and the beginning of damage, the radial fractures start to develop, as shown in Figure 107. Contrary to what was obtained with the "Holmquist" set, here the fractures maintain a certain symmetry, but the number of fragments is overestimated (10 fragments instead of 7-8 in the experimental experience).
The fact that this material model presents a greater number of fractures compared to the previous, less resistant parameter set might seem counterintuitive, but can be explained by the damage and erosion mechanism adopted by the software: in the first case analyzed, there is much more widespread and massive damage from the very first moments of the impact, which leads to the absorption of a large part of the kinetic energy and, consequently, the development of fewer fractures. With the "Nadal" parameter set, on the other hand, the material, being more resistant, initially offers more resistance to the impact, and the conical fracture zone is more limited: thus, more fractures develop because of the greater available kinetic energy that discharges onto the material in certain preferential directions. This hypothesis is confirmed by the greater inclination angle of the fracture cone obtained using the "Holmquist" set compared to that of the "Nadal" set.

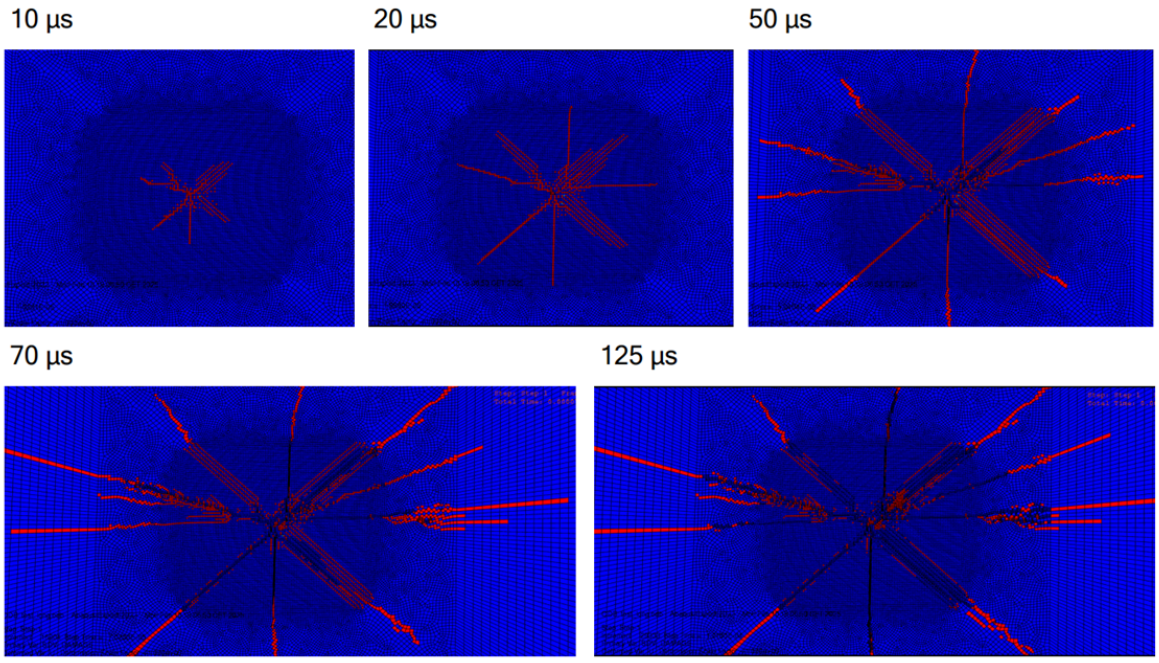

Figure 107

Figure 108 shows the section corresponding to a radial fracture: it can be seen that, also in this case, the progression of damage is limited by the size of the mesh. Immediately below the impact point there is a large area where the damaged elements have been removed by the software in accordance with the erosion criterion (removal occurs when the element deformation reaches a very high value, around 0.2).

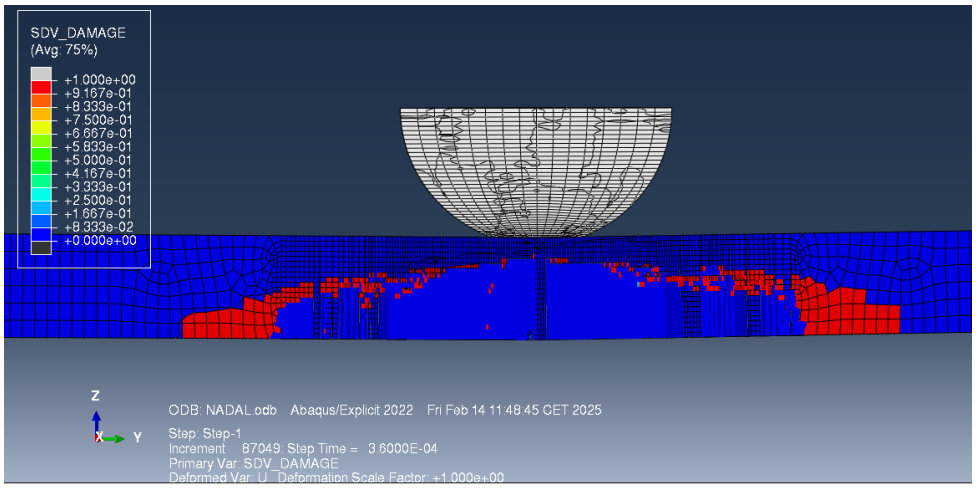

Figure 108

The main reference values obtained with the "Nadal" parameter set are summarized in the table:

	Nadal parameters	**Experimental values**
Max force on the indenter [kN]	40	19.9
Max displacement of the backing [mm]	0.447	0.660
Radial fractures	10	7
Fracture cone tilt angle [°]	45-50	30-35
Indenter imprint diameter	-	4-5

5.5.4 Results comparison and proposed set

From the comparison of the two parameter sets "Holmquist" and "Nadal" it can be concluded that for a low-velocity impact case both models are able to capture the fracture process. However, the representation of the forces and the backing deflection remains unsatisfactory and requires further study. To better visualize the comparison between the two sets, the graphs of reaction force and backing deflection for the two models are shown in figure 109 and figure 111, respectively.

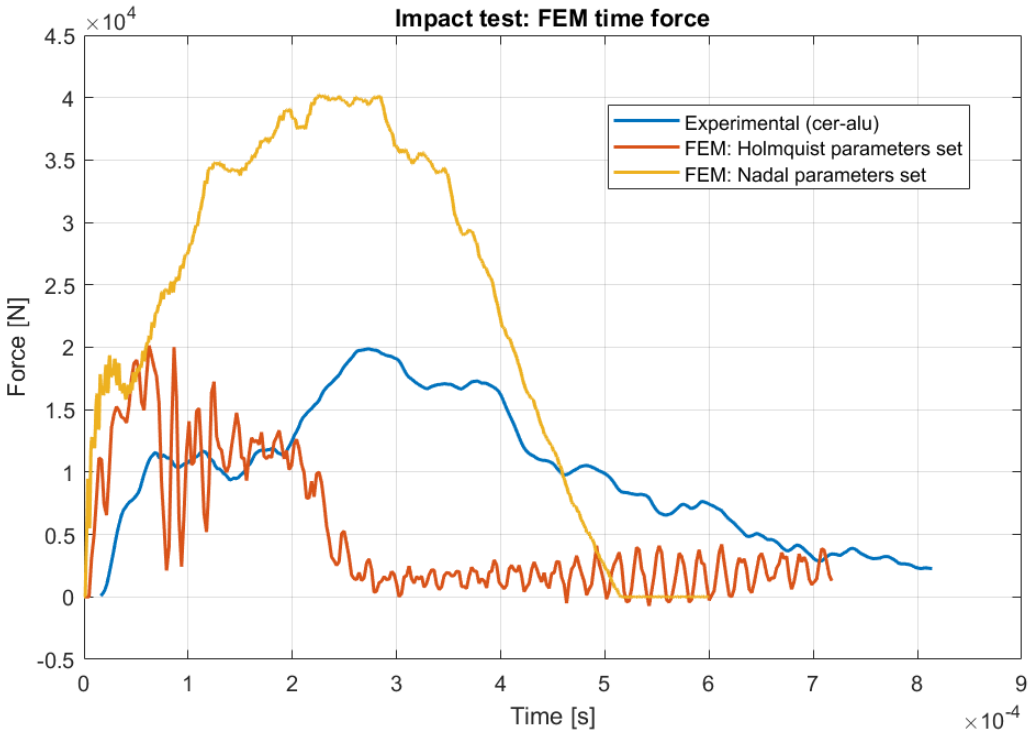

Figure 109

Figure 110: "Holmquist" and "Nadal" force plot comparison.

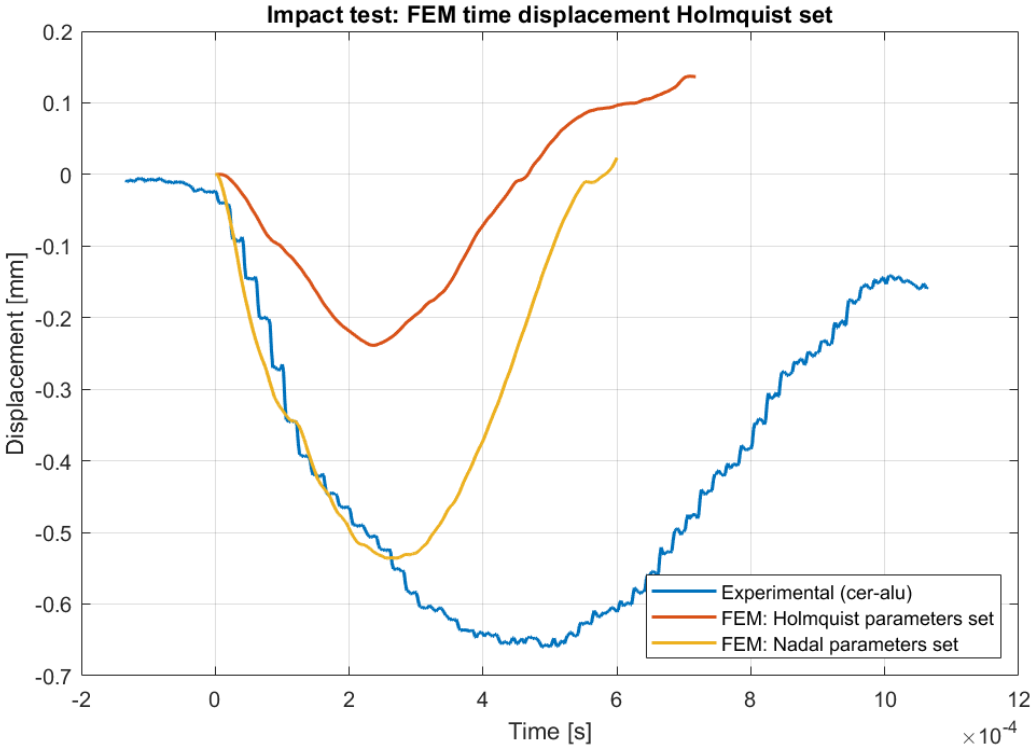

Figure 111

Figure 112: "Holmquist" and "Nadal" displacement plot comparison.

As is clear from the graphs the resistance of the material modeled with the "Nadal" set is too high, while that obtained with the "Holmquist" set is almost exact. This can be attributed to the different HEL value, which for low-velocity and low-strain-rate impacts is lower than the over 6 GPa predicted by the "Nadal" set. As shown in section 3.2.5, we can lower the maximum force values of the "Nadal" model by adjusting the HEL and A parameters (material strength coefficient, see equation 7) to try to correct the model.
An attempt was therefore made to correct the set by setting HEL=4000 GPa and A=0.6 to verify this hypothesis, which had proven correct in the static case by reducing the reaction force on the loading pin (see section 3.2.5 on the three-point bending test).
The comparison graphs of the new model "NadalHEL4000A06" are shown in figure 113 and figure 115.

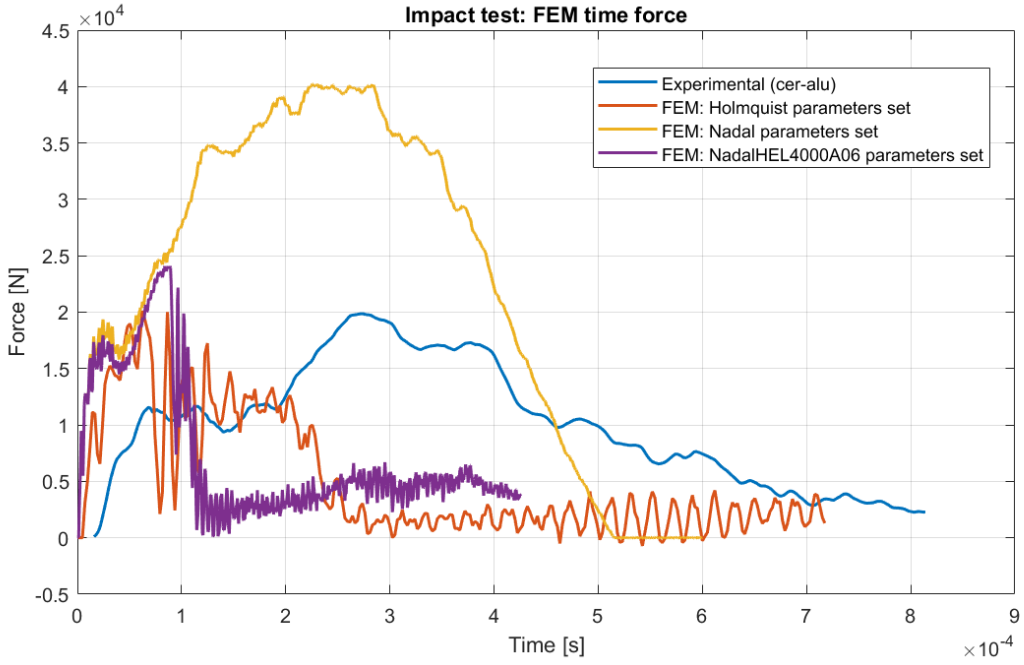

Figure 113

Figure 114: Force time plot for the "Nadal" set variant "NadalHEL4000A06".

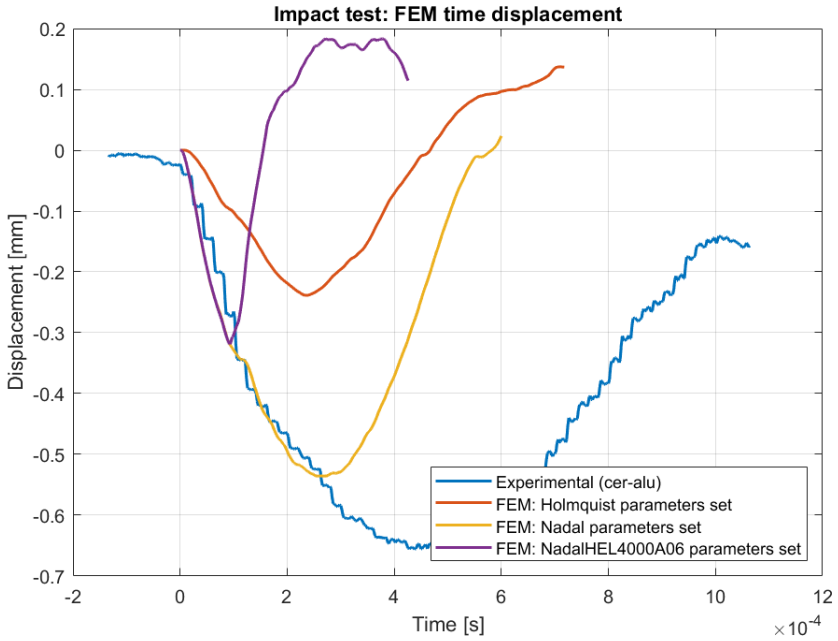

Figure 115

Figure 116: Displacement time plot for the "Nadal" set variant "NadalHEL4000A06".

An attempt was therefore made to correct the set by setting HEL=4000 GPa and A=0.6 to verify this hypothesis, which had proven correct in the static case by reducing the reaction force on the loading pin (see section 3.2.5 on the three-point bending test).
The comparison graphs of the new model "NadalHEL4000A06" are shown in figure 113 and figure 115. As can be seen from the graphs, although these modifications manage to reduce the maximum reaction

force, the model is still unable to effectively simulate the impact phenomenon, losing effectiveness in representing both the backing deflection and the fragmentation process.
Taking inspiration from the observations made in sections 5.5.2 and 5.5.3, we can propose a correction to the damage and strength parameters of the damaged material to obtain a softer reaction force curve for the set, similar to that obtained with the "Nadal" set. The hypothesis is that the HEL value of the "Holmquist" set is correct (as it predicts the correct maximum force), but that the material is somehow too weak when damaged.
We can then try to modify the parameters governing the resistance of the fractured material, in particular:

- Fracture strength constant: from B=0.310 to B=500;
- Fracture strength exponent: from M=0.6 to M=0.75;

Recalling the reference equations:

$$\sigma_i^* = A\left(p^* + \sigma_{t,m}^*\right)^N \left[1 + C\ln\left(dot\varepsilon + \dot{\varepsilon}_0\right)\right] \tag{20}$$

$$\sigma_f^* = B\left(p^*\right)^M \left[1 + C\ln\left(\dot{\varepsilon} + \dot{\varepsilon}_0\right)\right] \tag{21}$$

With these new parameters we obtain the following result in terms of force and deflection of the impactor:

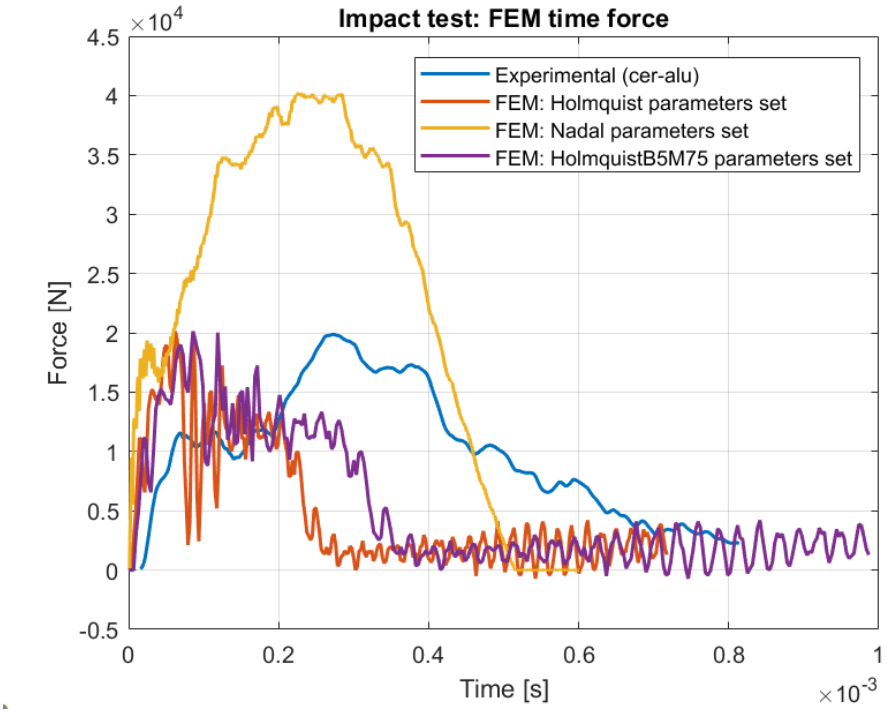

Figure 117

Figure 118: Force time plot for the "Holmquist" set variant "HolmquistB5M75".

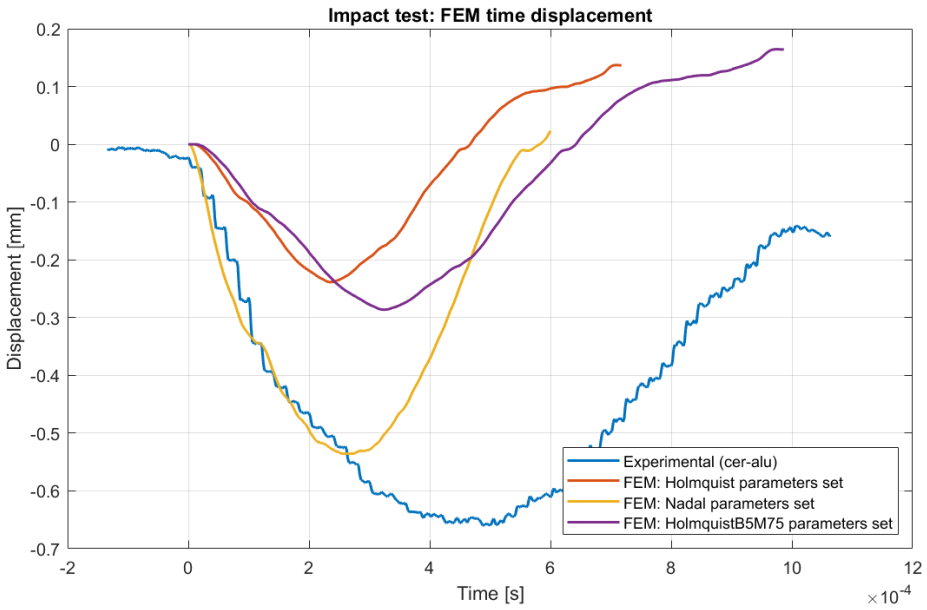

Figure 119

Figure 120: Displacement time plot for the "Holmquist" set variant "HolmquistB5M75".

As can be seen in the graphs, the modifications manage to slightly extend the ceramic response to the impact phenomenon: the material is slightly more resistant, and the collapse of the reactive force is delayed and less abrupt. Moreover, the curve appears more stable and free from the large oscillations visible with the original "Holmquist" set.
The material, once fractured, offers greater resistance to the impactor, which translates into a slightly greater deflection of the backing.
It can thus be observed that the modifications have achieved the desired effect, bringing the model behavior closer to that observed experimentally.

We can conclude that the best set of parameters for the drop test simulation is the "Holmquist" set, which, with a few targeted modifications, could be able to satisfactorily capture the temporal evolution of the reactive force on the impactor.

Nonetheless, it is necessary to refine the numerical parameters in order to improve the prediction of the backing deflection, which is still too low compared to that observed experimentally.
The superior performance of this set compared to "Nadal" one can be attributed to the lower Hugoniot Elastic Limit value: as we observed during the simulations of the three-point bending and Hopkinson bar tests, the "Holmquist" set proved suitable for representing the static behavior of the ceramic, whereas "Nadal" delivered the best results in the case of dynamic loads at high strain rates.

The present drop test falls between the two loading conditions of static and highly dynamic: although it is a dynamic phenomenon, the extremely low impact velocity ensures that the material behavior is more effectively represented by a "static" set such as Holmquist one.
For typical ballistic impact velocities, on the other hand, a better performance is expected from the Nadal set and a significant underestimation of the material resistance when modeled using the Holmquist set.

6 Conclusions and proposed developments

6.1 Conclusions

The present work aims to validate and calibrate a numerical model capable of describing and predicting the behavior of alumina ceramic during a ballistic impact on a dual-hardness ceramic/composite protection.
After presenting in Chapter 1 the characteristics and the materials used in dual-layer ballistic protection systems, the main damage mechanisms observed in ceramics subjected to dynamic loading were described, with particular attention given to the fracturing process in plate-projectile interaction phenomena.
Chapter 2 then introduced the numerical model "Johnson Holmquist II" and briefly explained its functioning. This model is particularly suited to describe the response of materials that undergo fracturing, damage, and fragmentation under extreme loading conditions, and it is based on an elastoplastic description with progressive material damage. In particular, the equations employed are:

- Equation of state for describing the relationship between hydrostatic pressure, density, and internal energy;
- Strength model for computing the strength of the intact material and its progressive deterioration when damage is present, calculated via the damage model;
- Damage model, which describes the progressive deterioration of the material properties by updating its strength with the value of the damage parameter "D", calculated based on the plastic deformation of the ceramic.

Along with the description of the model equations, the three sets of parameters "Holmquist", "Khan", and "Nadal" have been reported in the literature for the numerical modeling of alumina ceramic.
To familiarize with the functioning of the computational model and make an initial comparison between the proposed sets, several compression and release tests were simulated on a single mesh element. This allowed exploring the influence of different parameters on damage modeling and accumulation of plastic deformation, highlighting the differences in the behavior of the three proposed sets.
Particular attention was given to the different value of the "Hugoniot Elastic Limit", a quantity that, under dynamic loads, defines the boundary between the elastic phase and the accumulation of plastic deformation, and hence the onset of damage.
In Chapter 3 the experimental three point bending test is described, which allowed the direct calculation of the material stiffness properties. The parameter sets adjusted for the new properties were then validated through numerical modeling of the bending test: while the first analyzed set "Holmquist" proved entirely capable of predicting the static behavior of the ceramic, the material properties in the "Nadal" set greatly overestimated the maximum reaction force peak on the loading pin.
Corrections were therefore suggested for the use of the "Nadal" set in the case of static loading by lowering the values of the Hugoniot elastic limit and the strength of the intact material, obtaining satisfactory results. The "Khan" set, on the other hand, was discarded as it was completely out of scale compared to the values of the other sets, which were then validated in Chapter 3 for dynamic cases through Hopkinson Bar tests at high strain rates.
In this latter context, the "Nadal" set excels in representing the real behavior of the material, achieving excellent results both in terms of stress and in modeling the process of partial fragmentation of the specimen. These first test campaigns made it possible to distinguish the fields of competence of each set: "Holmquist" for the static case and "Nadal" for the dynamic case at high strain rates.
Through the analysis of the Hopkinson bar tests and the post-processing of the data, numerous issues concerning the experimental test setup have been identified and corrections have been proposed.
It is recommended indeed to conduct an Hopkinson Bar test campaign to obtain the stress–strain curves of alumina at different strain rates: this will allow the computation of the "C" strain rate parameter for the strength equation of the JH2 model, allowing an automatic adjustment of the material strength levels based on the test dynamic conditions.
In Chapter 5 the experimental drop test campaign is described, carried out on alumina plates simply supported on an aluminum backing. The purpose of this first series of tests is to validate the ceramic fragmentation mechanism predicted by the numerical model and to qualitatively introduce the study of the effects of an elastomeric interlayer between the ceramic and the backing. Initial experimental results have shown that the interlayer is able to damp the reactive force curve, lowering its maximum peak and

reducing the rear deflection of the ballistic protection.
These findings suggest the need for further studies to optimize the double-layer protective structure, effectively making it composed of three layers ceramic-elastic adhesive-backing. In particular, future research should focus on a deep understanding of the waves phenomena at the interfaces between the elastomeric interlayer and the ceramic layer, verifying whether and how these mechanisms change at the high speeds typical of ballistic impacts. From this perspective, the conducted drop test campaign should be considered merely a preliminary test aimed solely at data collection and qualitative observation of the phenomenon.
The results of the drop tests have nevertheless been useful for the present study as they allowed for the validation of the fracture mechanisms of the numerical model in the case of low-speed impact, achieving satisfactory yet still imperfect results. In fact, the two sets "Holmquist" and "Nadal" exhibit notable inaccuracies in representing, respectively, the levels of backing deflection and the reactive force on the impactor, while still capturing the fundamental fracture mechanisms observed in the experimental tests and predicted by the literature.
In general, the "Holmquist" set was considered the best for simulating the drop test: this can be explained by the low dynamicity of the test (the impact velocity is only 4.2 m/s).
In fact, the two parameter sets can be regarded as equally valid alternatives for modeling alumina at different impact velocities: for low strain rates or in static cases, the use of the "Holmquist" set is appropriate, whereas the "Nadal" set is recommended for simulating highly dynamic tests at medium-high strain rates. This is mainly due to the different value of the Hugoniot Elastic Limit, a leading parameter in the material dynamic behavior: in this regard, it would be extremely useful to derive a relationship linking the HEL value to the strain rate of the impact test at different velocities.
In order to investigate the effect of various parameters on the numerical outcome two variants on the "Nadal" and "Holmquist" sets were proposed. In particular, the variation on the "Nadal" set was achieved by decreasing the value of the Hugoniot elastic limit and the strength of the intact material. However, the results of this modification turned out to be disappointing, causing the loss of the correct fracture representation and failing to achieve the intended objective. The variant on the "Holmquist" set, on the other hand, involved modifying the parameters related to the strength of the fractured material, successfully improving the model performance in smoothing the load curve and in the deflection of the backing.

6.2 Future developments

Future research should focus on gathering experimental data to characterize the behavior of alumina and complete the parameter definition for the Johnson–Holmquist II model.
In particular, it is recommended to carry out a series of Hopkinson Bar tests to obtain the stress–strain behaviour at different strain rates and determine the parameter C to be used in the resistance equations of the numerical model. These tests should be performed after modifying the experimental setup currently available in Institut Clément Ader and Isae Supaero laboratories, in order to meet the requirements of constant strain rate and dynamic equilibrium within the specimen, as explained in Chapter 4.1.1.
The aspects concerning the interaction between the elastomeric layer and the ceramic should be further investigated by expanding the drop test campaign already carried out: it will be necessary to experimentally characterize the elastomeric layer and conduct a larger number of impact tests at progressively increasing velocities. The study should be initially conducted at the lower velocities typical of drop tests and then extended to high-velocity ballistic impacts achievable via a gas gun, in order to verify how the mechanisms of shock generation and waves reflection change according to the test speed. If possible, the study should also include the search for the best material and interlayer thickness to maximize protection while minimizing cost and bulk.
It will therefore be necessary to test the entire dual harness armour ballistic protection structure with and without the central elastomeric layer, using different numerical models to simulate each constituent material: the Johnson-Holmquist II model for the ceramic and the VUMAT routine developed at ISAE Supaero for the composite backing. The latter numerical model is already available for the simulation of carbon fiber laminates with a thermoplastic matrix, and will therefore need to be calibrated for simulating the fibers that constitute the backing material.

Acknowledgments

I wish to express my sincere gratitude to all those who have contributed, with their support and expertise, to the realization of this project.
I would like to thank Professors Marco Gherlone and Frédéric Lachaud in particular for their support and valuable advice in writing this thesis, as well as all the other professors who helped and welcomed me at ISAE Supaero in Toulouse, where this thesis work was carried out.

Infine, un grande ringraziamento va ai miei genitori, che mi hanno sempre sostenuto e spinto all'eccellenza e senza i quali senza dubbio non sarei arrivato fin qui, e alla mia ragazza Paola, alla quale va tutto il mio affetto: che questi due anni siano i primi di una lunga serie!

Pietro

References

[1] Tristan Camalet. “Caractérisation et modélisation du comportement dynamique des matériaux constituant une structure de protection céramique-composite”. PhD thesis.

[2] Weinong Chen and Bo Song. Split Hopkinson (Kolsky) Bar.

[3] Weinong W. Chen and Bo Song. “Kolsky Compression Bar Experiments on Brittle Materials”. In: Boston, MA: Springer US.

[4] Cosculluela. “Plasticité, endommagements et ruptures des alumines sous sollicitations dynamiques triaxiales: influence de la taille de grains”. In: ().

[5] Forquin. “Endommagement et fissuration de matériaux fragiles sous impact balistique, rôle de la microstructure”. In: ().

[6] D. J. Frew, M. J. Forrestal, and W. Chen. “A split Hopkinson pressure bar technique to determine compressive stress-strain data for rock materials”. In: Experimental Mechanics ().

[7] George A. Gazonas. “Implementation of the Johnson-Holmquist II (JH-2) constitutive model into Dyna3D”. In: Army Research Laboratory ().

[8] Quinn George. Fractography of Ceramics and Glasses.

[9] Guodong Guo, Shah Alam, and Larry D. Peel. “Numerical analysis of ballistic impact performance of two ceramic-based armor structures”. In: Composites Part C: Open Access ().

[10] “Instron website: https://www.instron.com/it-it/products/testing-systems/universal-testing-systems/low-force-universal-testing-systems/6800-series”. In: ().

[11] G. R. Johnson and T. J. Holmquist. “A constitutive model for brittle ceramics subjected to large strains, high strain rates, and high pressures”. In: ().

[12] Gordon R. Johnson and Tim J. Holmquist. “An improved computational constitutive model for brittle materials”. In: Colorado Springs, Colorado (USA): AIP.

[13] M.K. Khan et al. “An investigation of the ballistic performance of independent ceramic target”. In: Thin-Walled Structures ().

[14] Malaise. “Reponse d’une céramique a l’impact d’un barreau à grande vitesse (1500 m/s). Croisement essais dynamiques-modelisation numérique.” In: ().

[15] Meyers. Dynamic Behavior of Materials.

[16] M.R. O’Masta. “Mechanisms of Dynamic Deformation and Failure in Ultra-High Molecular Weight Polyethylene Fiber-Polymer Matrix Composites”. In: ().

[17] Den Reijer. “Impact on ceramic faced armor”. PhD thesis.

[18] R. W. Rice. Mechanical Properties of Ceramics and Composites: Grain and Particle Effects.

[19] D.A. Shockey, J.W. Simons, and D.R. Curran. “The Damage Mechanism Route to Better Armor Materials”. In: ().

[20] E.C. Simons et al. “An experimental and numerical investigation of sphere impact on alumina ceramic”. In: International Journal of Impact Engineering ().

[21] Fuping Yuan, Vikas Prakash, and Terry Tullis. “Origin of pulverized rocks during earthquake fault rupture”. In: Journal of Geophysical Research ().